Water-soluble quantum dots: pH sensitivity, bioconjugation, and enzymatic sensing

David DEBRUYNE

Examination committee:

Prof. André Vantomme	KU Leuven	Chair
Prof. Carmen Bartic	KU Leuven	Supervisor
Prof. Margriet J. Van Bael	KU Leuven	Supervisor
Prof. Jean-Pierre Locquet	KU Leuven	Assessor
Prof. Jin Won Seo	KU Leuven	Assessor
Prof. Christ Glorieux	KU Leuven	
Prof. Zeger Hens	UGent	

Dissertation presented in partial fulfilment
of the requirements for the degree of
Doctor of Science (PhD): Physics

May 2016

Uitgegeven in eigen beheer, David Debruyne, Esstraat 54, 9700 Oudenaarde (Belgium)

Abstract

Quantum dots (QDs), also known as semiconductor nanocrystals, are fluorescent nanoparticles with unique, size-tunable optoelectronic properties. QDs form an active field of research because of the numerous promising applications in biological imaging, (bio)sensing, and optoelectronics. This thesis targets the biosensing field by investigating the optoelectronic properties of water-soluble QDs in the presence of enzymes. The joining of inorganic nanocrystals with organic biomolecules results in novel hybrid materials with exciting properties. QD-enzyme hybrid materials combine the size-tunable optoelectronic properties of QDs with the biocatalytic and substrate recognition properties of enzymes. These hybrid materials are promising candidates in the development of novel biosensors.

The goal of this thesis was to demonstrate enzymatic sensing with QDs and to investigate the interaction between the QDs and the enzymes. More specifically, we studied the interaction between CdSe/ZnS core/shell QDs and the enzyme *glucose oxidase* (GOX). This study was performed on both colloidal QDs and surface-deposited QDs. In the first case, the colloidal QDs were bioconjugated with GOX in solution. In the second case, QDs and GOX were successively deposited as thin films on an electrode surface. An important difference between these two cases is the QD property that is being monitored. In the solution-based approach, the photoluminescence (PL) of the QDs is monitored, while for the QD-enzyme film on a substrate, the photocurrent mediated by the (photoconductive) QDs is measured. Both the PL and the photocurrent are modulated by the enzymatic activity of GOX, thus enabling the sensing of glucose.

The fabrication and investigation of QD-enzyme systems is a multi-step process. Our work on colloidal and surface-deposited QDs can be divided into different parts. For the colloidal QDs: (1) water-solubilization of the QDs, (2) investigation of the influence of environmental factors on the QD PL, (3) bioconjugation of the QDs with GOX, and (4) enzymatic sensing with (the bioconjugated) QDs. For the surface-deposited QDs: (5) thin film deposition of QDs and GOX and the (electrochemical) characterization of these films. The wet-chemical synthesis of QDs was not part of this work, instead we used commercially available QDs. For one part of the thesis (pH sensitivity of QD

PL), we also investigated quantum rods (QRs).

We started from commercial semiconductor nanocrystals that were dispersed in apolar organic solvents. These crystals are initially covered with long-chain hydrophobic ligands, consequently they are not water-compatible. Therefore, we first performed the water-solubilization of the QDs (and QRs), for which there exist several methods. To find the optimal method for our application, we compared three common phase transfer strategies: (I) ligand exchange with dihydrolipoic acid, (II) coating with amphiphilic polymers using poly(styrene-co-maleic anhydride), and (III) micelle-encapsulation using poly(ethylene glycol)-appended phospholipids. Each of these methods could be successfully applied on both QDs and QRs. The methods were evaluated based on how they affect the QD optical properties and the stability of the dispersion. In terms of PL quantum yield, the best results were obtained for phospholipid micelles and polymer coatings. Micelle-encapsulated QDs were however easier to purify than polymer-coated QDs by gel filtration chromatography. Micelle-encapsulated QDs were therefore selected for the further experimental work on colloidal QDs.

To study the morphology of the nanocrystals, the water-soluble QDs and QRs were deposited on (functionalized) silicon surfaces using electrostatic attraction between the surfaces and the QDs. Atomic force microscopy (AFM) images and transmission electron microscopy images both showed a remarkable size difference between CdSe/ZnS QDs obtained from two different suppliers. The size difference is most likely due to a difference in the thickness of the ZnS shell. This difference in ZnS shell thickness may explain some of the observations regarding the pH sensitivity of QDs (see below).

To investigate the interaction between surface-deposited QDs and GOX, lipophilic QDs and GOX were successively deposited on dithiol-modified gold surfaces. We were able to measure electrochemical photocurrents and show that the wavelength-dependency of the photocurrent is similar to the QD absorption spectrum, which indicates that that the photocurrents were mediated by the QDs. AFM topography images and an enzymatic assay test suggested that the electrostatically-driven deposition of GOX on top of the QD film was not successful. We make suggestions on how to improve the surface deposition of GOX.

To study the enzyme-QD interactions in a consistent way, it is critical to control environmental parameters such as the pH, the ionic strength, *etc.* This is because the PL of QDs can be strongly affected by changes of these environmental parameters. We investigated the effect of several (environmental) factors on the QD PL. Firstly, the presence of electric fields can affect the PL of QDs through the so-called quantum-confined Stark effect. We investigated this effect on the ensemble level by depositing QDs on an interdigitated electrode chip. We found that the application of strong electric fields (~100 kV/cm) causes a significant redshift (several nm) as well as a decrease of the PL intensity. Secondly, aggregation of QDs may enable the electronic energy

transfer between closely-spaced QDs, causing a redshift of the PL wavelength. We observed that the aggregation of QDs at high ionic strength was indeed accompanied by a redshift of the PL wavelength. Thirdly, reabsorption of PL emission can also cause a subtle redshift. We found that the PL of water-soluble QDs is redshifted with increasing QD concentration.

The solution pH is one of the most important environmental factors that influence the QD PL. Several research groups have reported that the PL of QDs is pH-dependent. However, varying observations have been made and the mechanism behind the pH-dependent PL remains speculative, underlining the need for further investigation. We investigated the role of the organic ligands in the pH-dependency of the PL. To this end, we compared phospholipid micelle-encapsulated QDs, polymer-coated QDs, and dihydrolipoic acid-capped QDs. We found that the organic capping plays a crucial role in the pH-dependency of the PL. Moreover, we found that the pH-dependent PL changes possess both a reversible and an irreversible component and that the organic capping determines which of these two components dominates. Our observations suggest the involvement of different mechanisms including acid etching, the quantum-confined Stark effect, and pH-dependent surface passivation. Finally, we compared the pH-dependency of CdSe/ZnS QDs to that of CdSe/CdS QRs and found that the QD composition plays an important role. Furthermore, CdSe/ZnS QDs obtained from two different suppliers showed a different pH-dependency, which may be attributable to differences in the thickness or quality of the ZnS shell.

The bioconjugation of colloidal, micelle-encapsulated QDs with the enzyme GOX was attempted by three different approaches: by covalent crosslinking using EDC-NHS, by electrostatic adsorption, and by a combination of these two methods. Gel filtration chromatography was used to separate the bioconjugated QDs from unbound GOX. The success of the bioconjugation was evaluated by examination of the gel filtration elution profiles and by inspection of the collected size fractions by UV-visible absorption spectroscopy, dynamic light scattering and zeta potential measurements. For covalent crosslinking, we found no evidence of successful bioconjugation. In the case of electrostatic absorption, QDs and GOX formed large aggregates that precipitated out of solution. For the combination of electrostatic adsorption and covalent crosslinking, the bioconjugation was likely successful. Zeta potential measurements showed a reversal of the surface charge after bioconjugation, indicating that the positively-charged QDs were covered with negatively-charged GOX. AFM topography images, on the other hand, did not show an increase in particle size. Further measurements are required to obtain definite proof.

Finally, we investigated the influence of the enzymatic activity of GOX on the PL of colloidal QDs. We investigated two cases: unbound and bound GOX. In the first case, QDs and GOX are both freely dispersed in solution and are not bound to each other. The addition of glucose caused quenching of the PL intensity. Control experiments showed that the quenching is attributable to the

generation of hydrogen peroxide. In the second case, we used the bioconjugated QDs (GOX bound to QDs by the combination of covalent crosslinking and electrostatic adsorption). Again, the PL intensity was quenched by the addition of glucose. However, the presence of free GOX in the sample made it impossible to study the influence of the bioconjugated GOX separately. Moreover, the PL intensity changes caused by the enzymatic reaction showed a complex time-dependence. We give several suggestions to improve the experimental approach of future work.

Nederlandse samenvatting

Quantum dots (QDs) zijn anorganische halfgeleider-nanokristallen met unieke, grootte-afhankelijke optische en elektronische eigenschappen. QDs worden actief onderzocht omwille van de talrijke veelbelovende toepassingen binnen de biologische beeldvorming, (bio)sensoren en de opto-elektronica. In dit proefschrift richten we ons op het toepassingsgebied van biosensoren door het onderzoeken van de opto-elektronische eigenschappen van water-oplosbare QDs in de aanwezigheid van enzymen. Door het combineren van anorganische nanokristallen met organische biomoleculen worden nieuwe, hybride materialen met opwindende eigenschappen bekomen. Deze hybride materialen verenigen de grootte-afhankelijke opto-elektronische eigenschappen van QDs met de biokatalytische en herkenningseigenschappen van enzymen.

Het doel van dit doctoraatsonderzoek was het demonstreren van biosensing gebaseerd op enzymen en QDs en vervolgens het onderzoeken van de interactie tussen de enzymen en de QDs. Specifiek onderzochten we de interactie tussen CdSe/ZnS kern/schil QDs en het enzym *glucose oxidase* (GOX). Deze studie werd uitgevoerd op colloïdale QDs en op gedeponeerde QDs. In het eerste geval werden colloïdale QDs gefunctionaliseerd met GOX in oplossing. In het tweede geval werden QDs en GOX achtereenvolgens neergezet op het oppervlak van een elektrode in de vorm van een dunne film. Een belangrijk verschil tussen beide gevallen is de QD eigenschap die wordt gemeten. Voor de colloïdale QDs wordt de fotoluminescentie (FL) gemeten, terwijl voor de neergezette QDs de fotostroom (doorheen de fotogeleidende QDs) wordt gemeten. Zowel de FL als de fotostroom worden beïnvloed door de enzymatische activiteit van GOX, waardoor het mogelijk is glucose te meten.

De realisatie en studie van QD-enzym-systemen omvat verscheidene stappen. Dit werk op zowel colloïdale als gedeponeerde QDs kan als volgt worden onverdeeld. Voor de colloïdale QDs: (1) de fase-transfer van QDs naar waterige oplossingen, (2) onderzoek naar de invloed van omgevingsfactoren op de QD FL, (3) de biofunctionalisatie van QDs met GOX en (4) enzymatische biosensing met de QDs (al dan niet gefunctionaliseerd met GOX). Voor de gedeponeerde QDs: (5) afzetting van QDs en GOX als dunne filmen en de elektrochemische karakterisering van deze filmen. De chemische synthese van

QDs in oplossingen was geen onderdeel van dit werk. We maakten daarentegen gebruik van commercieel-beschikbare QDs. Voor één deel van de thesis (de pH-gevoeligheid van de QD FL) hebben we ook quantum-staafjes onderzocht.

We vertrokken van commerciële nanokristallen die zijn opgelost in apolaire solventen. Deze kristallen zijn bedekt met hydrofobe organische liganden. Bijgevolg zijn deze kristallen initieel niet water-oplosbaar. Er bestaan verschillende technieken voor de fase-transfer van nanokristallen van apolaire naar waterige solventen. We hebben drie van deze technieken met elkaar vergeleken: (1) vervanging van de originele hydrofobe liganden met hydrofiele dithiolen, (2) bekleding van de hydrofobe nanokristallen met amfifiele polymeren en (3) de inkapseling van de hydrofobe nanokristallen binnenin micellen van fosfolipiden. Elk van deze methodes kon succesvol worden toegepast op zowel QDs als quantum-staafjes. De methodes werden geëvalueerd op basis van hun invloed op de FL en de stabiliteit van de dispersie. Wat betreft de FL-efficiëntie werden de beste resultaten behaald met fosfolipide micellen en polymeer-bekleding. De QDs ingesloten in micellen lieten zich echter makkelijker zuiveren met behulp van gelfiltratie dan de QDs bekleed met polymeren. De micelle-methode werd daarom gekozen voor het verdere experimentele werk op colloïdale QDs.

De water-opgeloste QDs werden afgezet op (gefunctionaliseerde) silicium substraten om de vorm en grootte van de QDs te onderzoeken. Bij de afzetting werd gebruik gemaakt van elektrostatische aantrekking tussen het oppervlak en de QDs. Atoomkrachtmicroscopie en elektronenmicroscopie onthulden een merkwaardig verschil in deeltjesgrootte tussen CdSe/ZnS QDs van verschillende leveranciers. Dit verschil in grootte wordt waarschijnlijk veroorzaakt door een verschil in de dikte van de ZnS-schil. Dit verschil in dikte kan mogelijks enkele observaties in verband met de pH-gevoeligheid van de QDs verklaren (zie verder).

Voor het onderzoek naar de interactie tussen gedeponeerde QDs en GOX werden hydrofobe QDs en GOX achtereenvolgens gedeponeerd op goud-oppervlakken voorzien van een dithiol-laag. We waren in staat om elektrochemische fotostromen te meten en we konden aantonen dat de golflengte-afhankelijkheid van de fotostromen vergelijkbaar is met het absorptiespectrum van de QDs. Dit toont aan dat de fotostromen via de QDs verlopen. Atoomkrachtmicroscopie en een enzymatische assay test doen vermoeden dat de elektrostatisch-gedreven depositie van GOX niet was geslaagd. We doen enkele suggesties om de kansen op succes bij de depositie van GOX te verbeteren.

Om de interacties tussen enzymen en QDs op een consequente manier te kunnen onderzoeken, is het van groot belang om omgevingsfactoren zoals de pH, de ionsterkte, enz. te beheersen. Dit is noodzakelijk omdat de FL van QDs sterk beïnvloed kan worden door zulke omgevingsfactoren. Daarom onderzochten we de invloed van verschillende (omgevings-)factoren op de QD FL. Ten eerste onderzochten we het zogenaamde quantum-confined Stark effect. Dit effect beschrijft de invloed van elektrische velden op de FL van QDs. We onderzochten dit effect op het ensemble-niveau door QDs af te zetten op

een chip voorzien van in-elkaar-grijpende kamelektrodes. We vonden dat het aanleggen van sterke elektrische velden (~100 kV/cm) gepaard ging met een roodverschuiving van de FL en met een afname van de FL-intensiteit. Ten tweede observeerden we dat de aggregatie van QDs in oplossingen met hoge ionsterkte gepaard gaat met een roodverschuiving van de FL. Deze roodverschuiving is waarschijnlijk veroorzaakt door elektronische energietransfer tussen de opeengepakte QDs in de aggregaten. Een derde observatie was dat een toename van de concentratie QDs gepaard ging met een subtiele roodverschuiving van de FL. Aan de basis van deze roodverschuiving ligt de reabsorptie van FL.

De pH waarde van de oplossing is één van de meest belangrijke parameters die de FL van QDs beïnvloedt. Verschillende onderzoeksgroepen hebben reeds gerapporteerd over de pH-afhankelijkheid van de FL van QDs. Het mechanisme achter deze pH-afhankelijkheid is echter nog steeds speculatief. Er bestaan ook belangrijke verschillen tussen de observaties door verschillende onderzoeksgroepen onderling. Wij onderzochten de rol van de organische bekleding van de QDs in de pH-afhankelijkheid van de FL. We vergeleken QDs ingekapseld in fosfolipide micellen, QDs bekleed met amfifiele polymeren en QDs bezet met dithiol liganden. We vonden dat de organische bekleding een cruciale rol speelt in de pH-afhankelijkheid van de FL. Bovendien vonden we dat de pH-afhankelijke FL zowel een omkeerbare als een onomkeerbare component bezit. De organische bekleding bepaalt welke van deze twee componenten het zwaarst doorweegt. Onze observaties duiden op de betrokkenheid van drie verschillende mechanismes: (1) het etsen van de QDs in zuur milieu, (2) het quantum-confined Stark effect en (3) de pH-afhankelijke passivatie van het QD-oppervlak. Tenslotte vergeleken we de pH-afhankelijkheid van CdSe/ZnS QDs met deze van CdSe/CdS QRs en vonden dat de materiaalsamenstelling van de nanokristallen een voorname rol speelt in de pH-afhankelijkheid. We stelden ook vast dat CdSe/ZnS QDs van twee leveranciers onderling een sterk verschillende pH-afhankelijkheid vertoonden. Dit verschil kan te wijten zijn aan verschillen in de kwaliteit of dikte van de ZnS-schil.

Voor de biofunctionalisatie van colloïdale QDs met GOX werden drie verschillende methodes geprobeerd: (1) de vorming van covalente verbindingen gebruik makende van EDC-NHS, (2) elektrostatische adsorptie en (3) de combinatie van deze twee methodes. Gelfiltratie werd gebruikt om de gefunctionaliseerde QDs te scheiden van ongebonden GOX. Het succes van de functionalisatie werd geëvalueerd door onderzoek van de gelfiltratie profielen en door inspectie van de gefilterde fracties met UV/vis spectroscopie, dynamische lichtverstrooiing en metingen van de zeta-potentiaal. Voor de eerste methode vonden we geen aanwijzingen voor een succesvolle biofunctionalisatie. Voor de tweede methode observeerden we de vorming van aggregaten gevolgd door neerslag van deze aggregaten. Voor de derde methode, de combinatie van elektrostatische adsorptie en de vorming van covalente verbindingen, vonden we aanwijzingen van een succesvolle biofunctionalisatie. Metingen van de zeta-potentiaal toonden een omkering van de oppervlakte-lading na biofunctional-

isatie. AFM metingen toonden daarentegen geen toename in deeltjesgrootte. Verdere metingen zijn nodig om een sluitend bewijs te kunnen geven omtrent het al-dan-niet slagen van de biofunctionalisatie.

Tenslotte onderzochten we de invloed van de enzymatische activiteit van GOX op de FL van colloïdale QDs. We onderzochten twee gevallen. In het eerste geval waren GOX en QDs niet met elkaar gekoppeld (beide waren vrij verspreid in de oplossing). De toevoeging van glucose veroorzaakte een onderdrukking van de FL intensiteit. Controle experimenten toonden aan dat deze onderdrukking een gevolg was van de productie van waterstofperoxide door het enzym. In het tweede geval maakten we gebruik van de gefunctionaliseerde QDs (GOX gekoppeld aan QDs met de derde methode). Ook in dit geval observeerden we een onderdrukking van de FL na toevoeging van glucose. De aanwezigheid van ongebonden, vrije GOX enzymen maakte het echter onmogelijk om de invloed van de gebonden enzymen te onderzoeken. Bovendien vertoonden de veranderingen van de FL-intensiteit uitgelokt door de enzymatische reactie een ingewikkeld tijdspatroon. We stellen voor hoe de aanpak van toekomstige experimenten kan worden verbeterd.

Contents

List of abbreviations

A	Absorbance
AFM	Atomic force microscopy
APTES	(3-Aminopropyl)triethoxysilane
DHLA	Dihydrolipoic acid
DLS	Dynamic light scattering
EDC	1-Ethyl-3-(3-dimethylaminopropyl)carbodiimide
FWHM	Full width at half maximum
GOX	Glucose oxidase
HDA	Hexadecylamine
MAA	Mercaptoacetic acid
MES	2-(N-morpholino)ethanesulfonic acid
MPA	Mercaptopropionic acid
MWCO	Molecular weight cut-off
NHS	N-hydroxysuccinimide
ODA	Octadecylamine
ODPA	Octadecylphosphonic acid
PBS	Phosphate-buffered saline
PEG	Poly(ethylene glycol)
PL	Photoluminescence
PLI	Photoluminescence intensity
PSMA	Poly(styrene-co-maleic anhydride)
QCSE	Quantum-confined Stark effect
QD	Quantum dot
QR	Quantum rod
QY	Quantum yield
SD	Standard deviation
TEM	Transmission electron microscopy
TOP(O)	Trioctylphosphine (oxide)
UPW	Ultrapure water
a.u.	arbitrary units
pI	Isoelectric point

Introduction

Quantum dots (QDs) are inorganic semiconductor nanocrystals with unique, size-tunable optical and electronic properties. One of the salient properties of QDs is their bright photoluminescence (PL) that falls in the ultraviolet, visible, or near-infrared part of the electromagnetic spectrum depending on the size and composition of the QDs. Since the initial research on QDs in the late 1980s, a lot of progress has been made both in the synthesis of high-quality QDs and in the characterization of their optoelectronic properties. Today we have arrived at the point where the use of QDs in different application fields is being actively explored. These application fields include biological imaging and detection [1, 2], chemical sensors and biosensors [3, 4, 5], photocatalysis [6], photovoltaics and optoelectronic devices (LEDs and lasers) [7, 8].

The focus of this thesis is on the biosensor field. QDs can be used as integrated components in biosensors, where they may serve as transducers. Transduction of the biorecognition events is based on modulation of the optoelectronic signal of the QDs by fluorescence resonance energy transfer (FRET), electron transfer reactions, or electrochemiluminescence [9]. A subset of biosensors uses enzymes as the biorecognition elements. Enzymatic biosensors are attractive because enzymes can catalyze a great number of reactions without being consumed. In addition, enzymes are highly specific towards their substrate. The introduction of QDs in enzymatic biosensing brings together the size-tunable optoelectronic properties of QDs with the biocatalytic and substrate recognition properties of enzymes [4].

In this thesis we studied the combination of CdSe/ZnS QDs and the enzyme *glucose oxidase* (GOX). CdSe/ZnS QDs are among the most studied core/shell QDs [10]. Their synthesis can be well controlled and yields high-quality monodisperse nanocrystals with outstanding optical properties (high PL quantum yield, narrow emission, resistance to photobleaching, *etc.*). The optoelectronic properties of these QDs have been intensely investigated. GOX is one of the most widely used enzymes in the biosensor field and also forms the basis of many blood glucose meters. This enzyme is an oxido-reductase and catalyzes the oxidation of β-D-glucose to D-glucono-δ-lactone and hydrogen peroxide.

The modulation of the QD optoelectronic signal lies at the basis of QD-based sensors. There are several mechanisms by which enzymes can modulate

this optoelectronic signal. A first mechanism is the interaction of the QDs with one (or more) of the enzymatic reaction products. For instance, QDs are highly sensitive to the presence of reducing and oxidizing species (*e.g.* cathechols, quinones, and hydrogen peroxide) [11, 12, 13]. Electron transfer reactions between QDs and these redox-active species affect the QD PL (*e.g.* quenching). GOX produces hydrogen peroxide, which is a known quencher of QD PL. Direct electron transfer from the active redox center of the enzyme to the QD, bypassing the native electron acceptor (*e.g.* oxygen), is also possible. However, achieving electrical contact with the redox center of enzymes is not trivial, because in most enzymes, this center is surrounded by an insulating protein shell that obstructs electron tunneling [14]. The redox center of GOX, the co-factor flavin adenin dinucleotide (FAD), is also deeply buried within the protein core [15]. Nonetheless, electrical wiring of enzymes such as GOX has been successfully demonstrated, through clever engineering using nanoparticles. Xiao *et al.* demonstrated the electrical wiring of GOX by the reconstitution of apo-GOX (GOX missing its co-factor FAD) on FAD-functionalized gold nanoparticles [16]. Holland *et al.* optimized the electrical communication with GOX through the site-specific attachement of gold nanoparticles close to the active site of GOX [15]. This was done through the genetic modification of GOX such that is displays a thiol anchor group near its active site. A third mechanism is fluorescence resonance energy-transfer (FRET). This mechanism channels energy from a donor (the QD) to an acceptor through radiationless dipole-dipole interaction. FRET requires spectral overlap between the emission spectrum and absorption spectrum of the donor and acceptor respectively. Additionally, the donor and acceptor must be in close proximity and their dipoles need to be aligned. Medintz et *al.* showed that the clever attachment of a FRET quencher molecule onto QDs will suppress the QD PL until the addition of an analyte causes detachment of the quencher [17]. The recovery of the PL thus signals the detection of the analyte. In this work, we focus on the first mechanism, *i.e.* interactions between the enzymatic reactions products and the QDs.

Our study on the interaction between GOX and QDs consists of two parts. The first part deals with surface-deposited QDs and the second part deals with colloidal QDs. The application field for deposited and colloidal QDs is usually different: surface-deposited QDs find application in the biosensor field, whereas colloidal QDs are mostly used in biological imaging. From a research point of view, the study of both systems provides complementary information because deposited and colloidal QDs allow for the probing of different QD properties: colloidal QDs are well-suited to study the PL properties whereas surface-deposited QDs can be used to measure the photoconductive properties. For the colloidal and the surface-deposited QDs, it is expected that the enzymatic activity of GOX will modulate the PL signal and the (electrochemical) photocurrent respectively [18, 19].

In general, several intermediate steps are necessary to achieve the interaction between colloidal QDs and GOX. The first step is the water-solubilization

of QDs. The most common synthesis procedure for CdSe/ZnS QDs yields particles that are covered with long-chain hydrophobic ligands. As a consequence, these QDs initially lack water-compatibility. There are different strategies to render QDs water-soluble, including ligand exchange and ligand addition. After the water-solubilization step, the QDs can be functionalized with biological macromolecules (bioconjugation). The bioconjugation of QDs has been demonstrated for a variety of biomolecules, including DNA, antibodies, and enzymes [20, 21]. The bioconjugation of QDs with proteins has been demonstrated by covalent crosslinking [22, 23] and electrostatic binding [24, 25]. One of the goals of this thesis was to compare enzymatic biosensing based on freely-dispersed QDs and GOX to enzymatic biosensing based on bioconjugated QDs with attached GOX.

QDs can be sensitive to many (environmental) factors such as the pH, the ionic strength, electric fields, *etc.* These factors can affect the QD PL. For instance, it is known that a decrease of the solution pH may quench the QD PL [26]. It is important to separate PL changes caused by environmental factors from the PL modulations caused by the enzymatic activity. Knowledge of the influence of environmental factors on the QD PL is critical to achieve a correct understanding of the enzyme-QD interactions for two reasons. Firstly, the enzymatic activity may take place under changing environmental conditions. Identification of and control over these environmental conditions are necessary to properly assess the effect of the enzymatic reaction on the QD PL. Secondly, the enzymatic reaction may itself cause (local) environmental changes. For example, the GOX enzymatic reaction can cause a local drop in pH through the (indirect) production of gluconic acid. Therefore, a substantial part of this thesis is dedicated to the study of environmental factors that influence the QD PL.

Outline of the thesis

Chapter 1 - Quantum dots: an overview. The first chapter gives an overview of the QD research field. We discuss the basic electronic structure of QDs and the particle-in-a-box model for QDs. We give a short history of the development of the QD research field and discuss the potential applications. Finally, we discuss the different QD types by composition, structure, and shape.

Chapter 2 - Experimental techniques. This chapter explains briefly the key experimental techniques that were used in this work, namely UV-visible spectroscopy, fluorescence spectroscopy, time-correlated single photon counting, dynamic light scattering, zeta potential measurements, atomic force microscopy (AFM), and finally electrochemical measurements. We also explain some laboratory techniques: gel filtration chromatography, ultracentrifugation, and reverse dialysis.

Chapter 3 - Water solubilization of quantum dots. Different methods exist to make hydrophobic QDs water-compatible. In this chapter we present three water solubilization methods for QDs that were explored in this doctoral work: thiol ligand exchange, polymer coating, and micelle encapsulation. These three methods yield water-soluble QDs whose properties may differ widely in terms of PL quantum yield, particle size, size monodispersity, *etc.* We evaluate, based on the formerly mentioned properties, which of these methods is most suited for our goal (of enzymatic sensing with colloidal QDs). The experimental data presented in this chapter includes the PL and absorption spectra of the QDs (and QRs) before and after their water solubilization. We also elaborate on the purification steps that were performed before and after the phase transfer.

Chapter 4 - Quantum dots on surfaces. The goal of this thesis was to investigate the enzymatic sensing with colloidal and with surface-deposited QDs. This chapter contains the results for the surface-deposited QDs. The chapter starts with a brief literature overview of the most common deposition techniques for QDs. We then demonstrate the deposition of hydrophilic QDs and QRs on silicon substrates based on electrostatic adsorption. These samples were used to study the QD morphology by means of atomic force microscopy. The enzymatic sensing with surface-deposited QDs is usually based on current sensing, thus requiring the deposition of QDs and GOX on a conductive substrate. To this end, hydrophobic QDs and GOX were successively deposited on thiol-modified gold electrodes. We present AFM measurements of the gold electrode surfaces as well as measurements of the electrochemical (photo)current.

Chapter 5 - Environmental influences on quantum dot photoluminescence. As nanoparticles with very high surface-to-volume ratios, QDs can be very sensitive to the their immediate environment. Changes in the local environment can affect the optoelectronic properties of QDs. Therefore, knowledge of the environmental parameters is of paramount importance in order to understand the optoelectronic properties of QDs in a dynamic environment. This is certainly the case for QDs exposed to enzymatic activity. In this chapter, we discuss the effect on the QD PL of several factors, including particle concentration, electric fields, and the ionic strength.

Chapter 6 - pH sensitivity of quantum dot photoluminescence. This chapter addresses another environmental factor, the pH, which can have a dramatic effect on the QD PL. First, we give an overview of the current literature reports about the pH dependency of QD PL. Then we present our own results that deal with several aspects of the pH dependency: the role of the organic coating, the reversibility of pH quenching, and the time evolution of the pH

dependency. Based on our results, the possible mechanisms that underlie the pH-dependent QD PL are discussed. Finally we compare the pH dependency of CdSe/ZnS QDs and CdSe/CdS QRs.

Chapter 7 - Bioconjugation of quantum dots with glucose oxidase. The bioconjugation of QDs with enzymes can be achieved by different methods. In this chapter we present our results on three bioconjugation methods: covalent crosslinking using EDC-NHS, electrostatic attraction, and the combination of these two. We show how gel filtration chromatography can be used to size-separate GOX and (bioconjugated) QDs. We evaluate the bioconjugation methods through examination of the gel filtration size fractions.

Chapter 8 - Interaction of quantum dots with glucose oxidase. In the last chapter, we demonstrate enzymatic sensing with colloidal QDs. First we show the results for the case in which QDs and GOX are simply mixed in solution. Next we show the results for the bioconjugated QDs (GOX bound to QDs). Comparison between these two cases should in principle reveal how the bioconjugation of GOX to QDs affects the enzymatic sensing. We discuss the experimental problems that prevented us from making such a comparison.

Appendix A - Buffer preparation using $_{\mathrm{pH}}$Tools. In this appendix we show how the preparation of constant-ionic strength buffer series can be planned with $_{\mathrm{pH}}$Tools, a Matlab toolbox.

Appendix B - Fabrication of an interdigitated electrode chip. This appendix gives the process sheet for the fabrication of the interdigitated electrode chip that was used to measure the quantum-confined Stark effect.

Appendix C - Design of the flow cell. This appendix shows the design of the flow cell that was used for the continuous UV-vis absorption measurements during gel filtration chromatography.

Chapter 1

Quantum dots: an overview

Quantum dots (QDs) are semiconductor nanocrystals in which the electrons and holes are confined in all three dimensions. QDs have dimensions typically between 1 and 10 nm. Figure 1.1 shows an transmission electron micrograph of a QD, clearly visualising the crystalline nature of the particle. QDs possess interesting optical and electronic properties that are not seen in the corresponding bulk semiconductors. Mainly two features distinguish QDs from their bulk counterparts. Firstly, QDs have dimensions that are smaller than the Broglie wavelength of electrons, which leads to the manifestation of quantum mechanical effects. Because the electrons and holes are confined to a finite volume, they occupy discrete energy levels. Moreover, the position of the energy levels depends on the size of the particles (quantum-size effect). Consequently, the optoelectronic properties of QDs are size-dependent. A second important difference with the bulk materials is the large surface-to-volume ratio in QDs. The fraction of surface atoms to total atoms is large in QDs, whereas the surface fraction is negligible in bulk crystals. Consequently, surface-related phenomena play an important role in QDs [27].

1.1 Electronic structure

Inorganic solids can be divided into three classes: metals, semiconductors, and insulators. In a solid, the atomic orbitals combine to give an energy spectrum. In a bulk solid, the energy levels are so closely spaced that they dissolve into bands. Roughly speaking, metals have a partially filled band, while semiconductors and insulators have a filled valence band separated from an empty conduction band by an energy gap (figure 1.2A). In semiconductors this energy gap or bandgap (E_g) amounts to $0.5 - 3.5$ eV, whereas in insulators E_g is typically larger than 4 eV.

Electrons in the valence band can be promoted to the conduction band by

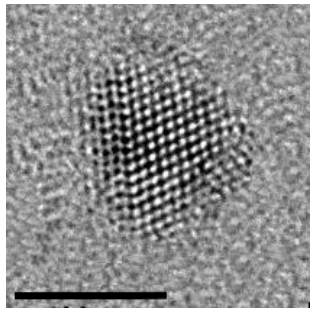

Figure 1.1 – Transmission electron micrograph of a CdSe/ZnS core/shell QD. The scale bar is 5 nm. Remark: the ZnS shell is not clearly distinguishable.

the absorption of a photon with an energy larger than the bandgap, thereby leaving behind a hole in the valence band. Depending on the energy of the photon, the electron can be excited high into the conduction band. Quick relaxation by small nonradiative transitions usually brings the electron to the lowest-energy state of the conduction band, which is a meta-stable state. The final transition of electron then depends on the type of semiconductor. In direct bandgap semiconductors, the lowest energy state of the conduction band and the highest energy state of the valence band share the same crystal momentum. Consequently, excited electrons can relax back into the valence band by emission of a photon. In indirect bandgap semiconductors, the crystal momentum is different for the lowest conduction band state and the highest valence band state. In this case, a radiative transition cannot occur without the assistance of a phonon to carry the momentum difference. Because this process is very unlikely, radiative relaxation is much slower in indirect bandgap semiconductors and the electron decays mostly nonradiatively.

The electron and hole usually form a bound state called an *exciton*, because of their mutual Coulombic attraction. Because of this attraction, the lowest-energy exciton has an energy slightly smaller than the bandgap. The exciton is described by a hydrogen-like Hamiltonian [28]:

$$\hat{H} = -\frac{\hbar}{2m_h^*}\nabla_h^2 - \frac{\hbar}{2m_e^*}\nabla_e^2 - \frac{e^2}{\epsilon_r|r_e - r_h|}, \tag{1.1}$$

where m_e^* and m_h^* are the effective masses of the electron and hole respectively, and ϵ_r is the dielectric constant of the solid. The exciton thus has a spherically symmetric wave function, the extent of which is described by the exciton Bohr radius:

$$a_{\text{exciton}} = a_0\epsilon_r\frac{m_e}{\mu}, \tag{1.2}$$

with a_0 the Bohr radius in a hydrogen atom, m_e is the electron rest mass, and $\mu = m_e^* m_h^* / (m_e^* + m_h^*)$ the reduced mass. The effective masses m_e^* and m_h^* are

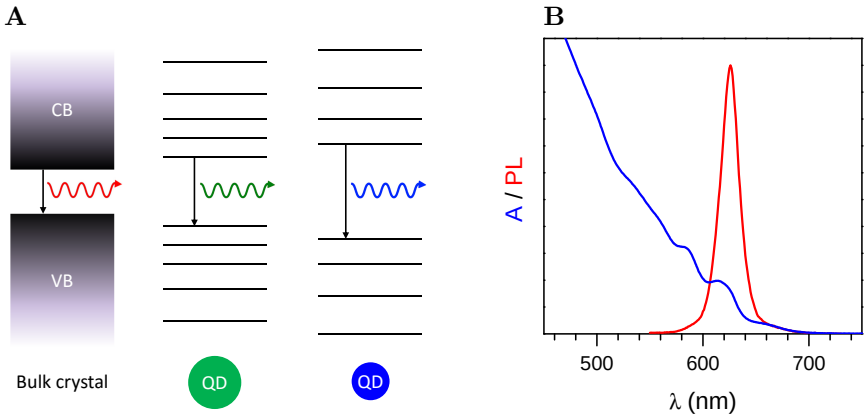

Figure 1.2 – **(A)** Simplified electronic structure for a bulk semiconductor crystal and two QDs with different sizes. The bulk crystal has two energy bands, the filled valence band (VB) and the empty conduction band (CB). The QDs possess discrete energy levels, of which the position depends on the size of the QD. Notice that the bulk crystal has the smallest bandgap and that the exciton confinement increases the bandgap for the QDs. The arrow denotes an electronic radiative transition that emits a photon of which the colour depends on the bandgap. **(B)** Typical UV-visible absorption spectrum and photoluminescence (PL) spectrum of CdSe/ZnS QDs. The lowest excitonic transitions are visible as features in the absorption spectrum.

usually only a fraction of the electron mass. As a consequence, the localization energy for the excited electron and hole is large. The dielectric constant ϵ is typically large in inorganic semiconductors (in the range $5 - 12$), which means that the Coulomb attraction between electron and hole is mostly screened. As a result of these two factors, the exciton wave function typically extends over a large distance. For instance, the exciton Bohr radius for CdSe is ~6 nm [29].

Things get interesting when the size of the nanocrystal becomes comparable to or smaller than the exciton Bohr radius. In this case, the exciton becomes confined, thereby adding confinement energy to the system. The degree of confinement depends on the size of the QD. As a consequence, the quantized energy spectrum of QDs becomes dependent on the particle size for sizes smaller than the exciton Bohr radius. The allowed size-dependent optical transitions are clearly visible as features in the absorption spectra as well as in the PL excitation spectra of QDs [30]. Figure 1.2B shows a typical UV-visible absorption spectrum and PL spectrum of CdSe/ZnS QDs.

Particle-in-a-sphere

The "particle-in-a-box" model is quite successful in describing the basic photophysics of direct bandgap semiconductor nanocrystals [31]. In this model, a particle (electron or hole) is confined inside a spherical potential well of radius a.

$$V(r) = \begin{cases} 0 & r \leqslant a \\ \infty & r > a \end{cases}. \tag{1.3}$$

Solving the Schrödinger equation with these boundary conditions gives the eigenfunctions

$$\Phi_{n,l,m}(r,\theta,\phi) = C\frac{j_l(k_{n,l}r)Y_l^m(\theta,\phi)}{r}, \tag{1.4}$$

where C is a normalization constant, $Y_l^m(\theta,\phi)$ is a spherical harmonic, and $j_l(k_{n,l}r)$ is the l-th order spherical Bessel function. The associated eigenvalues are:

$$E_{n,l} = \frac{\hbar^2\alpha_{n,l}^2}{2m_0a^2}, \tag{1.5}$$

with $\alpha_{n,l}$ the n-th zero of the l-th order Bessel function j_l and m_0 the mass of the particle. Equation 1.5 shows that the energy of the particle depends strongly on the particle size as $1/a^2$. Of course, a QD is not an empty sphere, but consists of a crystal lattice of semiconductor atoms. In the effective mass approximation, the effect of the complicated periodic potential on the particle is taken into account by replacing m_0 by an effective mass m^*. L. E. Brus related the energy of the *lowest* excited electronic state (= the bandgap energy) to the particle size by the following formula [32]:

$$E_g(\text{QD}) = E_g(\text{bulk}) + \left(\frac{\hbar^2\pi^2}{2R^2}\right)\left(\frac{1}{m_e^*} + \frac{1}{m_h^*}\right) - \frac{1.8e^2}{\epsilon R}, \tag{1.6}$$

with R the QD radius, and m_e^* and m_h^* the effective masses of the electron and hole respectively. The second term represents the quantum energy of localization for both the electron and hole (particle-in-a-box) and the third term represents the Coulomb attraction between the electron and hole. The Brus model works well only for larger QDs ($R > 2.5$ nm)[33]. It also does not explain the higher excitonic states in the linear absorption spectrum nor the origin of the PL Stokes shift. However, the model gives a qualitative estimate of the most obvious aspect of quantum confinement: the ability to tune the electronic bandgap by changing the crystal size.

For a more realistic description of the electronic states and transitions in a real QD, a higher level of theory is required, such as the multiband effective mass approximation [34]. This model takes into account that the valence band

in II-VI semiconductors is comprised of several closely lying bands and that these bands are generally not parabolic. Efros *et al.* were the first to incorporate also the electron-hole exchange interaction, the typically non-spherical shape of the nanocrystals, and the intrinsic hexagonal lattice asymmetry [35]. In this way, they were able to explain some of the finer details of QD PL such as the unusually long lifetime of the excited state at low temperature, the large Stokes shift observed for nonresonant excitation, *etc.*

1.2 A short history of the quantum dot field

The systematic investigation of QDs began in the 1980s with the pioneering work of Brus et al. on cadmium-based (CdS and CdSe) nanocrystals [36, 37]. It was inspired also by theoretical work that showed that the linear and nonlinear optical properties could be enhanced in nanocrystals when the size of the particle becomes smaller than the exciton Bohr radius [38]. In the early days, QDs were mostly synthesized in aqueous solution with added stabilizing agents [1]. The early synthesis routes suffered from major problems such as irreproducibility in preparation and colloidal instability [39]. The colloidal stability issue could be circumvented by incorporating the small clusters into solid matrices such as polymers and glasses. Later, methods were developed to cap the cluster surface with organic or inorganic groups (e.g. polyphosphates and thiols) to stabilize the clusters against agglomeration. However, most of these methods still led to QDs with large size variations and low PL quantum yields.

In 1993, Bawendi and co-workers reported a novel synthesis route based on the injection of organometallic precursors into a hot coordinating solvent followed by a temperature drop [40]. Much narrower size distributions (<5% rms in diameter) could be achieved with this technique, because the nucleation stage was temporally separated from the growth stage of the nuclei [7]. However, the PL quantum yield was still relatively low (~10%). To overcome the problem of low PL QY, an increasing number of groups started using so-called core/shell QDs. By overcoating the QD with a shell of a second semiconductor that has a higher bandgap, non-radiative recombination sites on the QD surface are passivated, leading to an enhancement of the PL QY [41, 10]. The progress in the synthesis of high quality QD samples enabled the study of the finer optoelectronic properties of QDs, which had previously been obscured by broad size distributions, poor crystallinity, or surface electronic defects [40]. Figure 1.3 shows the number of publications per year since 1985 dealing with QDs. This number has increased year after year up until 2011. More than 6000 QD-related publications are appearing yearly the past few years.

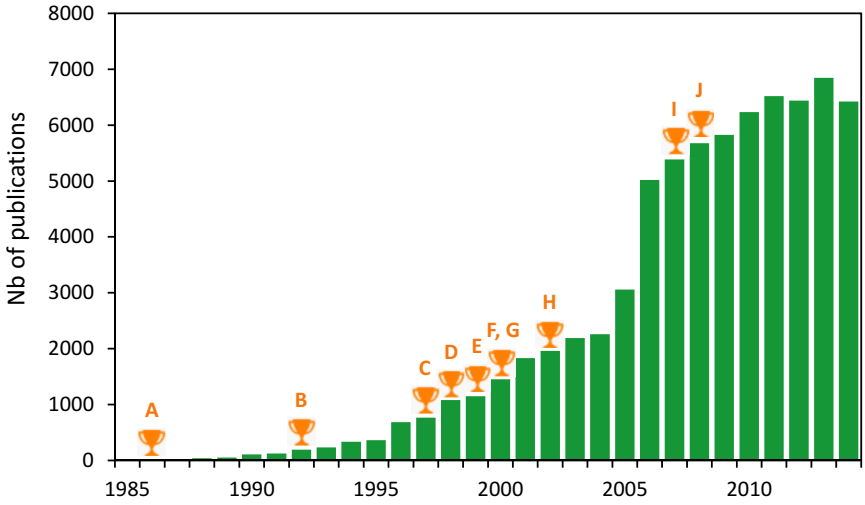

Figure 1.3 – The number of publications per year since 1985 containing in their title one of the following terms: "quantum dot(s)", "semiconductor cluster(s)", "semiconductor microcrystallite(s)", or "semiconductor nanocrystallite(s)" (Web of Knowledge, Thomson Reuters). The chalices mark some of the landmark publications in the field: (A) Pioneering experimental work on CdS QDs by Brus et al. [36], (B) Bawendi et al. report a novel synthesis route that yields high-quality monodisperse QDs [40], (C) Influential paper on core/shell QDs [41], (D) Demonstration of QDs as fluorescent biological labels [42], (E) Report on the PL mechanism in silicon QDs [43], (F) Paper about the optical gain and stimulated emission in nanocrystal quantum dots [8], (G) Bioconjugation of QDs with proteins [24], (H) In vivo imaging with water-soluble QDs encapsulated in phospholipid micelles [44], (I) Report on the renal clearance of QDs [45], and (J) Review about the use of QDs in solar cells [46].

1.3 Applications

The interest in QDs has come from various research fields that have seen potential applications for QDs. Firstly, QDs show exciting possibilities in biology, biomedicine, and (bio)sensing. QDs have shown great potential as fluorescent tags for biological imaging applications [47, 48, 1]. QDs possess several advantages over standard organic dyes, including size-tunable fluorescence and absorption, large absorption cross sections, narrow emission, the potential for multiplexing, and low photobleaching rates. QDs are also used as fluorescent labels in bioassays, where they can be conjugated to highly specific biomolecules such as antibodies (immunoassays) [3]. The large surface-to-volume ratio of nanostructures can be exploited in chemical and biological sensors [49, 50]. The sensing activity typically takes place only on the surface and not in the

interior, making the large surface-to-volume ratio of QDs an asset.

Secondly, the size-tunable electronic structure of QDs could make them useful building blocks for optoelectronic devices. The ongoing miniaturization in electronic device fabrication has brought the device dimensions into the nano-domain. The knowledge obtained from studies on QDs could help in understanding the design rules for next generations of electronic circuits [7]. The size-tunable electronic structure, small exciton binding energy, high luminescence efficiency, and low thermal conductivity make QDs attractive for photovoltaic, lighting, and thermoelectric applications [7]. Colloidal nanocrystals offer additional opportunities in terms of cheap (large area) device fabrication by solution-based techniques such as spin-coating, dip-coating, inkjet printing, *etc.*

1.4 Types by composition and structure

In principle, QDs can be made from any semiconductor material that exists in the bulk. The selection of materials has primarily been driven by the ability to prepare from these materials nanocrystalline particles with the desired optical properties [48]. Differences between the semiconductor materials exist mainly in terms of the accessible range of emission wavelengths, the QD synthesis procedure, chemical stability, and biocompatibility.

QDs made from II–VI compounds (CdS, CdSe, ZnO, etc.) are among the most popular today. Progress in the synthesis of Cd-based QDs in solution has led to the availability of high quality Cd-based QDs with narrow size distributions and high PL quantum yield. By properly tuning the size and composition, the PL of Cd-based QDs can cover the entire visible light spectrum (figure 1.4). Cd-based QDs are commercially available for research purposes. Recently also QDs based on the I-III-VI ternary compound $CuInS_2$ became commercially available. QDs made from Pb-based compounds such as PbS, PbSe, and PbTe are interesting from a fundamental physics point of view. In these semiconductors, *both* the electron and the hole exhibit a large Bohr radius, which facilitates the study of the strong-confinement limit [29]. QDs made from III-V compounds such as GaS, InP, GaN, etc. are popular for use in optoelectronic applications. However the colloidal synthesis of III-V QDs has proven more challenging than the synthesis of II-VI QDs [51].

Most of the previously mentioned QDs contain one ore more heavy metals. The application of heavy-metal based QDs in life science applications is severely limited because of toxicity concerns. There is a potential risk of heavy metals leaking out of the QD particles over time under illumination or by oxidation [48]. It was shown that cytotoxicity of CdSe QDs correlates with the liberation of free Cd^{2+} ions caused by the deterioration of the CdSe lattice, although the QDs can be rendered nontoxic when appropriately coated [52]. However, even QDs made from benign materials that are inert and do not decompose

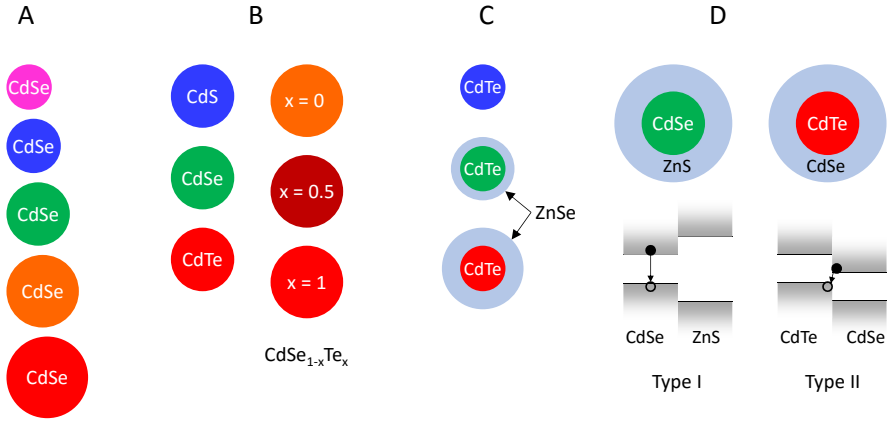

Figure 1.4 – Conceptual illustration of bandgap tuning in QDs: (A) by variation of the size, (B) by changing the composition, and (C) by lattice strain tuning. Panel (D) shows the electronic bands for a type I and type II core/shell QD. The colors are indicative for the PL emission wavelength.

can be toxic. Nanoparticles in general can cause toxic effects by sticking to the cell surface, by being ingested by the cell, or even by impaling the cell in the case nanoparticles with a sharp shape [53]. The use of heavy metals in electrical and electronic products is also regulated in the European Union by the Restriction of Hazardous Substances (RoHS) directive. For instance, the levels of Cd should not exceed 100 ppm (there are some exceptions, for instance for Cd in solar panels) [54].

QDs made from group IV semiconductors (Si, Ge, C, SiC) are heavy metal free and are probably the most promising with regard to biocompatibility. Group-IV elements are usually not popular in optics or optoelectronics because they have an indirect bandgap, which results in very low PL efficiencies. However, nanostructures of group IV-elements can have substantially improved PL efficiencies [55]. SiC and C QDs are very robust and chemically inert, but there exist few methods to their synthesis in solution [55]. Si and Ge QDs on the other hand, can be synthesized by various solution methods.

Next to the composition, QDs can also differ in structure. As opposed to "core-only" QDs (*e.g.* CdSe QDs), many of the QDs prepared these days have an onion-like structure, with a core surrounded by a shell of another semiconductor material (*e.g.* CdSe/CdS QDs). Some QDs possess multiple shells of different semiconductor materials (*e.g.* CdSe/ZnSe/ZnS QDs). One of the functions of the shell is to provide a physical barrier between the optically active core and the surrounding medium, making the QDs less sensitive to environmental changes, surface chemistry, and photo-oxidation [10]. As a con-

sequence, the PL quantum yield of core/shell QDs can be substantially higher than that of core-only QDs.

The shell provides also a means to further tune the electronic structure of the core/shell QD (figure 1.4C). In core/shell QDs such as CdSe/ZnS, there is a large lattice mismatch (~12 %) between the core and shell materials because they have a different bond length [56]. The lattice mismatch introduces a strain field that can be used to tune the electronic bandgap. For instance, the fluorescence spectrum of CdTe/ZnSe QDs with 1.8 nm cores can be dramatically red-shifted (~350 nm) by increasing the epitaxial shell thickness from 0 to 6 monolayers [57]. For CdTe/ZnSe QDs with a core of 6.2 nm, the obtainable PL redshift is much smaller because of strain relaxation due to the formation of lattice defects.

Two types of QDs can be discriminated based on the bandgap alignment of the core and the shell (figure 1.4D). In type I QDs (*e.g.* CdSe/ZnS QDs), the bandgap of the shell is larger than that of the core. The shell has a higher valence band and a lower conduction band compared to the core. As a result, both charge carriers are confined to the QD core. In type II QDs (*e.g.* CdTe/CdSe QDs, CdSe/CdS), the bandgaps of the shell and the core are staggered in such a way that both the valence and conduction band are higher or lower than in the core. As a result, one of the charge carriers is confined to the core whereas the other charge carrier is confined to the shell. The separation of the charge carriers has important consequences. The carrier recombination taking place at the core/shell interface proceeds at a reduced energy, leading to a redshift of the PL spectrum [58, 56]. Secondly, the reduction in electron-hole wave function overlap leads to a smaller oscillator strength and thus longer excited state lifetimes.

The previously described core/shell QDs are heterostructures, with a clear segregation between the core and shell materials. It is also possible to prepare homogeneously alloyed QDs with a smooth transition between core and shell, such as $CdSe_yTe_{1-y}$, and $Cd_xZn_{1-x}S$ [59, 60]. This allows for tuning the electronic structure by changing the composition without changing the particle size (figure 1.4B).

1.5 Quantum rods

As explained in the previous section, there are several ways to tune the electronic structure of the QD. There is yet another way of doing so and that is through the shape of the nanocrystal. The shape controls the dimensionality of the quantum confinement. In quantum wells, electrons are confined in only one dimension, whereas in quantum wires, they are confined in two dimensions, and in QDs they are confined in all three dimensions. Particle-in-a-box approximations show that 3D confinement is stronger than 2D confinement, which in turn is stronger than 1D confinement [61]. As a consequence, the

size-dependent change of the bandgap is predicted to be the largest in dots, followed by rods and wires, and finally wells. This was partially confirmed experimentally for InP QDs and wires [62]. Quantum disks [63] and quantum rods are the colloidal analogues of quantum wells and quantum wires respectively. Certain phenomena such as the quantum-confined Stark effect (see chapter 5) may be enhanced in quantum rods as compared to QDs, because of the larger polarizability of these elongated crystals [64].

Chapter 2

Experimental techniques

In this chapter we introduce the experimental techniques that have been used most extensively in this work. To probe the opto-electronic properties of QDs we used UV-visible spectroscopy, fluorescence spectroscopy, and time-correlated single photon counting. To obtain information on the hydrodynamic size and surface charge of colloidal QDs, we performed dynamic light scattering and zeta potential measurements respectively. Atomic force microscopy (AFM) was used to investigate the distribution and morphology of surface-deposited QDs. Electrochemical measurements were performed to investigate the photoconductive properties of surface-deposited QDs. We also introduce some laboratory techniques: gel filtration chromatography and ultracentrifugation were used for the purification of QDs, and reverse dialysis was used to increase the QD concentration.

2.1 Ultraviolet-visible spectroscopy

Ultraviolet-visible (UV-vis) spectroscopy is routinely used in analytical chemistry for the quantitative determination of different analytes, by measuring their absorption of light in the ultraviolet and visible regions of the spectrum. The absorption of light by matter is related to electronic transitions from the ground state to the excited states in that matter. The absorption spectrum therefore provides information on the electronic structure of the analyte. The measurement instrument, the UV-visible spectrophotometer, consists of a high-intensity light source (*e.g.* a xenon lamp) that produces light over the entire UV-visible region of the spectrum. A monochromator selects a narrow band of wavelengths from the source light. The monochromatic beam then illuminates the sample and the transmitted light is detected. The sample typically is a solution that contains one or more light absorbing species. Most often the sample container is a cell or cuvette with a typical optical path length of 10

mm. Disposable plastic cuvettes are suitable for routine work in the visible range. Quartz cuvettes are used for the more accurate work (especially at low absorbances < 0.1) or when measuring in the UV region of the spectrum.

The output typically given is the wavelength-dependent absorbance A. Absorbance is a number that measures the attenuation of light in a material and is given by

$$A = \log_{10}\left(\frac{I_0}{I}\right). \tag{2.1}$$

Here I_0 is the intensity of the incident light and I is the intensity of the transmitted light. Attenuation is usually due to the physical process of absorption, but reflection, scattering, and other physical processes may contribute. The Beer–Lambert law relates the attenuation of light to the properties of the material through which the light is travelling. For a liquid containing N different species, the absorbance A is given by

$$A = \sum_{i=1}^{N} c_i \epsilon_i l \ , \tag{2.2}$$

with c_i and ϵ_i the concentration and the molar attenuation coefficient of specie i, and l the optical path length. When the liquid contains only one type of specie, measuring the absorbance allows one to calculate the molar concentration of the specie if one knows the path length and the molar attenuation coefficient.

In practice, a cuvette with a reference solution is measured before each sample (series). This reference solution is usually the solvent without the absorbing specie(s). Subsequent measurements subtract the reference measurement such that only the absorbing species contributes to the absorption spectrum.

2.2 Photoluminescence spectroscopy

Photoluminescence (PL) spectroscopy is a spectroscopic technique that analyses the PL generated by a sample after its optical excitation. The measurement instrument is called a fluorometer (or fluorimeter). The instrument typically consists of a light source, a detector, a sample stage, and two monochromators, one to select the excitation wavelength and one to select the emission wavelength that is being measured. The second monochromator is most often placed at a 90° angle with respect to the incident excitation beam. This serves to minimize the risk of transmitted or reflected excitation light reaching the detector.

PL spectroscopy has some inherent advantages over UV-visible spectroscopy [65]. Firstly, the sensitivity is greatly enhanced, because the emitted

light is detected against a background of zero. In UV-visible spectroscopy on the other hand, small changes in light intensity are measured against a large intensity background. Secondly, each PL measurement requires the input of two specific wavelengths (one for excitation and one for emission). Therefore PL measurements have a higher specificity towards the measured compound than absorption measurements. The largest drawback of PL spectroscopy is that it is limited to fluorescent molecules only (non-fluorescent species may however be coupled to fluorescent dyes).

It is important to correct the raw spectrum $I_u(\lambda)$ for any instrument-dependent and sample-specific contributions. Practically this is done by subtracting from the raw spectrum a blank spectrum $I_b(\lambda)$ obtained from a cuvette containing only the solvent. Next one should correct for the wavelength-dependent spectral responsivity $s(\lambda)$ of the instrument to obtain the corrected spectrum $I_c(\lambda)$, which is instrument independent.

$$I_c(\lambda) = \frac{I_u(\lambda) - I_b(\lambda)}{s(\lambda)}. \tag{2.3}$$

The peak wavelength (λ_{peak}) is the wavelength at which the PL spectrum reaches its maximum intensity. Because most PL spectra are measured with a 1-nm step, the sensitivity of λ_{peak} to subtle changes in the spectral position of the PL is limited. For this reason we often use the intensity-weighted average wavelength (λ_{avg}) instead, which is calculated by

$$\lambda_{avg} = \frac{\sum_\lambda I_c(\lambda)\lambda}{\sum_\lambda I_c(\lambda)}. \tag{2.4}$$

This figure is also sensitive to changes in the shape of the spectrum, in contrast to the peak wavelength.

2.3 Photoluminescence quantum yield measurements

The efficiency or quantum yield (Φ) of the PL is defined as the ratio of absorbed photons to photons emitted through PL.

$$\Phi = \frac{\text{emitted photons}}{\text{absorbed photons}}. \tag{2.5}$$

The quantum yield can be determined directly by optical methods, either relatively to a PL standard of known quantum yield, or absolutely with an integrating sphere setup. Other methods measure the quantum yield indirectly, for instance by measuring the dissipated heat after excitation with an intense laser light source [66]. The optical method is complicated by the fact that measuring the total number of emitted photons accurately is not straightforward.

A conventional fluorimeter detects only a fraction of the emitted fluorescent light. The size of this fraction is nearly impossible to determine, because it depends on many factors, both instrument-related (numerical aperture, detection angle, *etc.*) and sample-related (scattering, solvent refractive index, *etc.*). To overcome this problem, the use of a PL standard of known quantum yield (comparative method), or alternatively an integrating sphere (absolute method) is necessary.

2.3.1 The comparative method

The comparative method requires only a common fluorimeter and UV-vis spectrophotometer. In this method, the quantum yield of a test sample (X) is estimated by comparing its PL with that of a standard (ST) of known quantum yield. Essentially, when the test sample and standard have an identical absorbance at the same excitation wavelength, they can be assumed to be absorbing the same number of photons and the ratio of their integrated PL intensities should yield the ratio of the quantum yield values. Obtaining two samples with the same absorbance at a specific wavelength is not practical, and this restriction can be lifted by taking the ratio of the absorbances.

In a fluorimeter, the intensity of the excitation light as well as the response of the monochromators and detector usually vary with wavelength. Although most modern fluorimeters apply automatic correction for these intensity fluctuations and for the spectral response of the detector, it is still advantageous to choose the standard such that its optical properties (absorption and PL spectrum) overlap with those of the test sample. Note that for some wavelength regions (e.g. the near-infrared), no reliable standards are available [66].

A fast result can be obtained with a single-point measurement of the absorbance and integrated PL of the sample and the standard:

$$\Phi_X = \Phi_{ST} \frac{PL_X}{PL_{ST}} \frac{A_{ST}}{A_X}, \tag{2.6}$$

with Φ_{ST} the quantum yield of the PL standard, PL_X and PL_{ST} the spectrally-integrated PL of respectively the sample and the standard, and A_X and A_{ST} the absorbance at the excitation wavelength of respectively the standard and the sample. To determine the quantum yield more accurately, one can take multiple measurements of the PL spectrum at different absorbance values. To this end, several dilutions of the sample and of the standard are prepared. The dilutions should be well-chosen and have absorbance values in the range $0-0.1$. The fluorophore concentration should be low enough to minimize the re-absorption of PL [67]. If the solvent of the sample and standard is different, an additional factor should be included to correct for the difference in refractive index. The quantum yield is then calculated by

$$\Phi_X = \Phi_{ST} \left(\frac{\mathrm{Grad}_X}{\mathrm{Grad}_{ST}} \right) \left(\frac{\eta_X^2}{\eta_{ST}^2} \right), \tag{2.7}$$

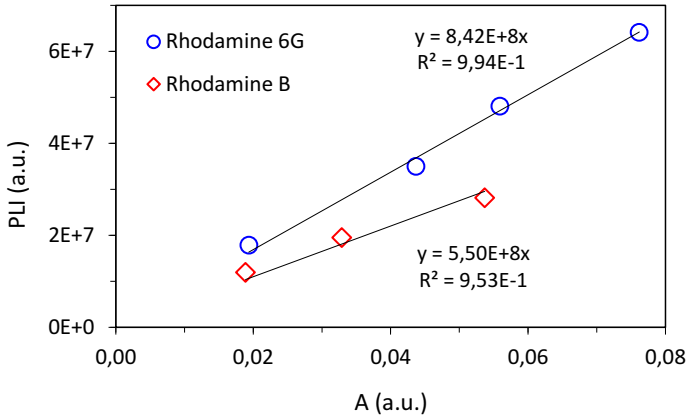

Figure 2.1 – Calculation of the PL quantum yield of rhodamine B in ethanol with the comparative method, using equation 2.6. The PL intensity (PLI) is plotted versus the absorbance for different dilutions of rhodamine 6G and rhodamine B. The linear fit through the data gives the gradients required to calculate the unknown quantum yield.

where Grad_X and Grad_{ST} are the slopes of the PL intensity versus the absorbance for respectively the sample and the standard, and η_X and η_{ST} are the refractive indices of respectively the sample and the standard. Figure 2.1 shows an example of the comparative method, where we measured the quantum yield of rhodamine B, using rhodamine 6G as a standard. Rhodamine 6G has a quantum yield of 0.95 in ethanol [68]. By applying equation 2.7, we obtain a quantum yield of 0.62 for rhodamine B, which is close to the literature value of 0.65 [68]. Relative quantum yield measurement are tricky to measure and they are usually reported with quite large errors (~10%) [69]. There are some excellent guides for the beginner, describing the procedure and the most common pitfalls [69, 70, 66].

2.3.2 The absolute method

The absolute method uses a calibrated fluorimeter equipped with an integrating sphere. An integrating sphere is a hollow sphere that has its inner surface coated with a diffusely reflecting material. In an ideal integrating sphere, the light from a light source is redistributed isotropically over the surface of the sphere, regardless of the angular dependence of the emission [71]. Hence if N_Ω photons are detected over a solid angle Ω, then the total number of photons is given by

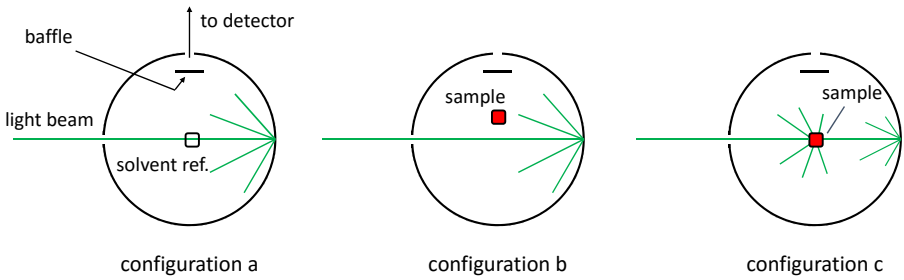

Figure 2.2 – The method of De Mello *et al.* for the experimental determination of the absolute quantum yield involves three measurement configurations [71]: a) solvent reference in beam; b) sample out of the beam; c) sample in the beam.

$$N = N_\Omega \left(\frac{4\pi}{\Omega} \right). \tag{2.8}$$

It is thus possible to determine the total number of photons emitted by the sample. The number of absorbed photons can also be deduced, by measuring the decrease in the excitation light intensity caused by the absorbing sample. Practically, one measures the PL spectrum of the sample ($I_X(\lambda_{em})$) as well as the excitation light spectrum with the sample still inside the sphere ($I_X(\lambda_{exc})$). Next, the sample is replaced by a blank (solvent without fluorophore) and these two measurements are repeated, yielding the PL background ($I_B(\lambda_{em})$) and another excitation light spectrum ($I_B(\lambda_{exc})$). The quantum yield can then be calculated absolutely by dividing the emitted photon flux (F) by the absorbed photon flux (F_{abs}) [66]:

$$F = \int_{\lambda_{em}} \frac{I_X(\lambda_{em}) - I_B(\lambda_{em})}{s(\lambda_{em})} \lambda_{em} d\lambda_{em}, \tag{2.9}$$

$$F_{\text{abs}} = \int_{\lambda_{exc}} \frac{I_B(\lambda_{exc}) - I_X(\lambda_{exc})}{s(\lambda_{exc})} \lambda_{exc} d\lambda_{exc}, \tag{2.10}$$

with $s(\lambda)$ the spectral responsivity of the instrument.

De Mello *et al.* reported an alternative protocol for the experimental determination of the absolute quantum yield [71]. Their protocol includes an additional configuration in which the sample is placed inside the sphere but outside the excitation light path. This configuration measures the indirect (secondary) excitation of the sample by light reflected from the cavity walls. Figure 2.2 shows the three measurement configurations used in the protocol of de Mello *et al.* Each configuration involves two measurements, one in the excitation wavelength region and one in the PL wavelength region, giving a total

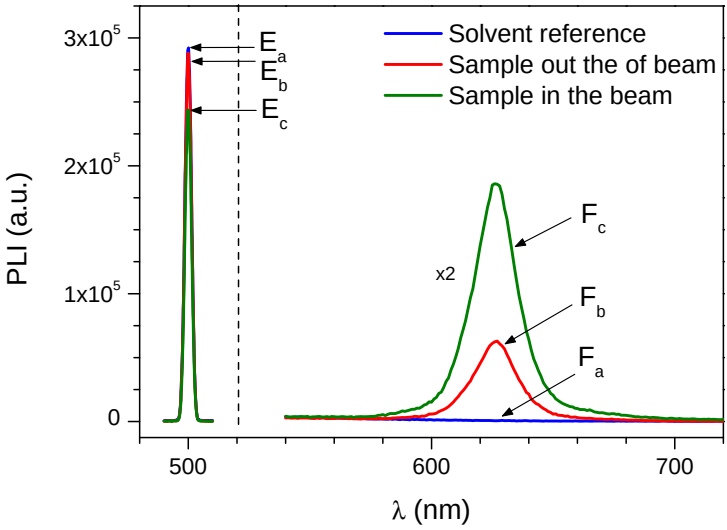

Figure 2.3 – Illustration showing the six spectra that are measured to determine the absolute quantum yield. For each of the three measurement configurations (a, b, and c), the excitation light profile (E) as well as the PL spectrum (F) of the sample is measured.

of six spectra (see figure 2.3). We refer to the area under the corrected PL and excitation spectra as F_a, F_b , F_c, E_a, E_b, and E_c. From these quantities, the absolute quantum yield can be calculated as [71]

$$\Phi = \frac{F_c - F_b(1 - A)}{E_a A}, \tag{2.11}$$

with A (the direct absorption)

$$A = \frac{E_b - E_c}{E_b}. \tag{2.12}$$

Despite the practical and theoretical differences between the two methods described above (involving either two or three measurement configurations), these methods are generally in excellent agreement [72]. Values of the absolute quantum yield reported in this thesis were obtained with the method of de Mello *et al.* The excitation light spectra were always recorded with a neutral density filter placed behind the exit of the integrating sphere. The recorded spectrum was corrected afterwards for the wavelength-dependent transmission of the filter.

2.4 Time-correlated single photon counting

2.4.1 Working principle

Time-correlated single photon counting (TCSPC) is a well-established and common technique for fluorescence lifetimes measurements. It is a time-domain technique (as opposed to a frequency-domain technique). In TCSPC, the sample is excited by a pulsed light source, and the PL decay profile is reconstructed by registering the arrival times of many single photon events.

Measuring the time-dependent intensity profile requires the excitation of the sample by a short flash of light. In principle, one could attempt to measure the decay profile from a single excitation-emission cycle, but this is hindered by some practical problems. Firstly, ordinary electronic recorders often do not possess the required temporal resolution to resolve the shape of the decay profile of fast emitters (*e.g.* a fluorescent compound with a lifetime of 500 ps would require signal sampling with a 10-ps time step)[73]. Secondly, the PL signal may be too weak to create an analog voltage that represents the incoming photon flux. This would be especially so in the case of single molecule spectroscopy. TCSPC overcomes these two problems by extending the data collection over multiple excitation-emission cycles. The PL decay profile is reconstructed from the precise registration of arrival times of single photons collected over multiple cycles.

The experimental setup used in TCSPC is shown in figure 2.4. TCSPC requires a pulsed light source, for instance a pumped picosecond dye laser or Ti:sapphire laser. Since the turn of the century, also solid-state light sources such as pulsed laser diodes and pulsed light emitting diodes have found their introduction in the technique [74]. The excitation light pulse is split into two components, one to excite the sample and one to serve as a reference for the timing mechanism. After their detection, the arrival times of the excitation and emission pulses are accurately determined with a common fraction denominator (CFD).

At the heart of the timing mechanism lies a time-to-amplitude converter (TAC), which generates a voltage that increases linearly with time on the nanosecond scale. In the normal TCSPC configuration, the TAC voltage ramp is started by the arrival of the excitation pulse. The TAC is occupied either until a STOP signal is generated by the *first* detection of a photon emitted by the sample, or until the TAC completes its sweep. However, running data collection in the normal configuration results in substantial deadtime, *i.e.* time during which the TAC is in operation and unable to respond to another signal [75]. The deadtime is minimized in the reverse configuration, in which the first photon from the sample serves as a START signal, while the excitation pulse serves as the STOP signal.

After amplification, the TAC voltage is digitized by an analog-to-digital converter (ADC). The resulting binary value is sent to the multi-channel analyser

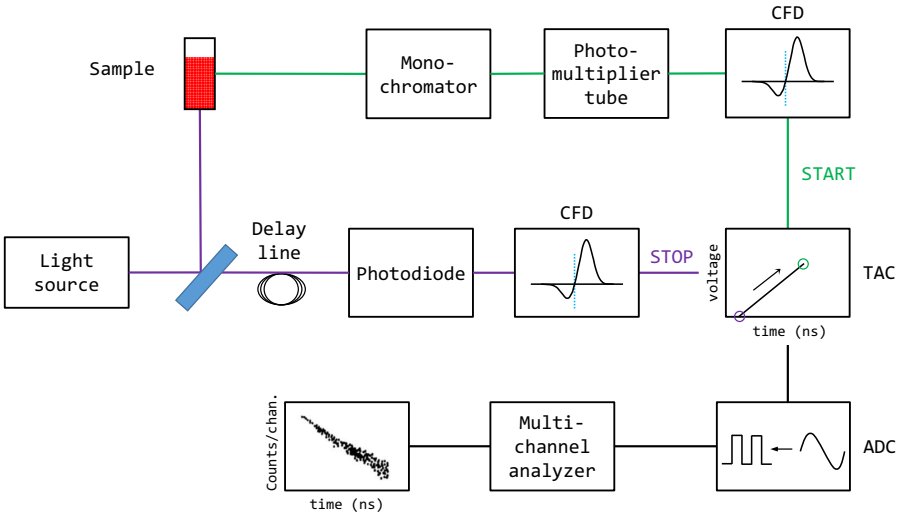

Figure 2.4 – Block diagram of a TCSPC system (reverse configuration).

(MCA) and provides the address of the channel (memory location) of which the content has to be increased by one. The channels are like the bins of a histogram, each one corresponding to a certain time interval. By the repetitive detection of single photons, a histogram of the emission decay is constructed.

Because only the first photon is observed in TCSPC, it is critical that the photon detection rate remains low (typically 1 photon per 100 excitation pulses) [74]. If the photon count rate is too high, the histogram will be biased towards shorter times and it will not represent the actual PL decay.

Figure 2.5 shows a typical example of TCSPC data. Three functions are shown: the measured decay $N(t_i)$, the instrument response function (IRF) $L(t_i)$, and the calculated decay $N_c(t_i)$. These three functions exist only at discrete times t_i, because the photon arrival times are binned over a finite number of channels by the MCA. The IRF represents the overall timing precision of the TCSPC system. For an ideal system the IRF is infinitely narrow. In reality, the IRF is broadened by the duration of the excitation light pulse, the timing accuracy of photon registration by the detectors, *etc.* The IRF can be determined by tuning the emission monochromator to the excitation wavelength and measuring scattered excitation light (*e.g.* from a colloidal solution).

It is important to understand that the measured intensity decay $N(t_i)$ is a convolution of the real intensity decay $I(t)$ and the instrument response function $L(t_i)$. The measured intensity decay therefore takes on the shape of the IRF. Mathematically, the convolution of two functions f and g, supported on $[0, +\infty[$, is given by

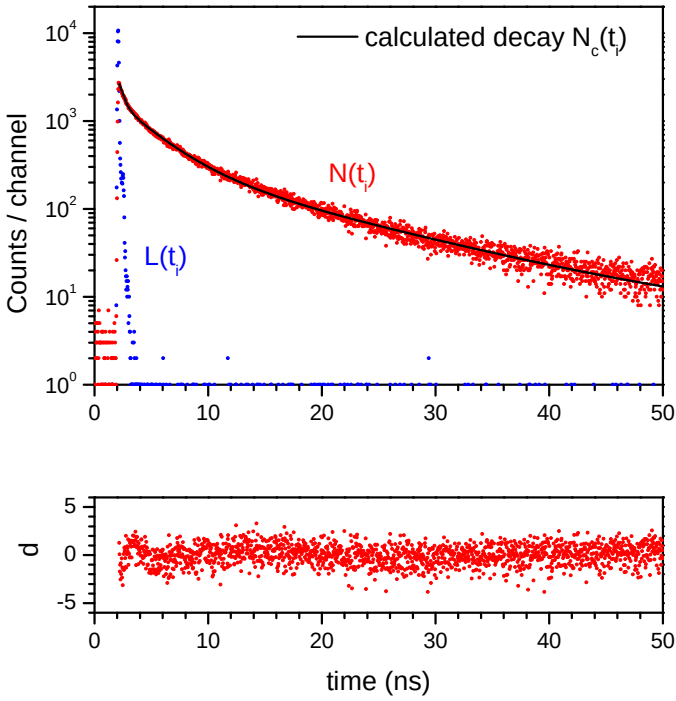

Figure 2.5 – TCSPC data for QDs dispersed in water. The top panel shows the instrument response function (blue points), the PL decay curve of the QD sample (red points), and a three-component exponential fit to the PL decay curve (black line). The lower panel shows the fit residuals.

$$(f \otimes g)(t) = \int_0^t f(t')g(t-t')dt'. \tag{2.13}$$

Applying this to our case, we have

$$N(t) = (L \otimes I)(t) = \int_0^t L(t')I(t-t')dt'. \tag{2.14}$$

Because $N(t_i)$ and $L(t_i)$ exist only at discrete times, this is more appropriately written as

$$N(t_i) = \sum_{k=0}^{i} L(t_k)I(t_i - t_k)\Delta t, \tag{2.15}$$

with Δt the channel width.

The task is now to determine the intensity decay $I(t)$ that best matches the experimental data. One method to do this is by non-linear least squares (NLLS) analysis. In fact, NLLS assumes a model decay $I(t)$ that is believed to describe the data. Let's say that we expect our data to obey first order kinetics. Hence the decay is given by

$$I(t) = A\mathrm{e}^{-t/\tau}. \tag{2.16}$$

The goal is to test whether this model is consistent with the data and if so, to obtain the set of parameter values that provides the best match between the measured decay $N(t_i)$ and the calculated decay $N_c(t_i)$. The problem is solved by iterative reconvolution. Given a set of start values for the floating parameters (A and τ in this case), $I(t)$ is convoluted with the IRF $L(t)$, and the calculated decay $N_c(t_i)$ is compared with the measured decay $N(t_i)$. The parameters are adjusted iteratively in order to minimize the goodness-of-fit parameter χ^2, which is given by

$$\chi^2 = \sum_{i=1}^{n} \frac{[N(t_i) - N_c(t_i)]^2}{N(t_i)}. \tag{2.17}$$

Usually, the reduced value χ^2_R is reported, because χ^2depends on the number of data points.

$$\chi^2_R = \frac{\chi^2}{n-p}, \tag{2.18}$$

where n is the number of data points and p the number of floating parameters. The goodness-of-fit should also be judged visually by inspecting the residuals $R(t_i)$=$N(t_i)$-$N_c(t_i)$ (figure 2.5, lower panel). The residuals should be randomly distributed around zero and any form of pattern should be absent.

2.4.2 Experimental details

The PL decay curves were recorded with the TCSPC setup of the *Single Molecules Detection* group of Prof. Johan Hofkens. A detailed description of the setup used can be found in reference [76]. Briefly, the PL decay histogram was collected in 4096 channels over 120 ns, thus obtaining a resolution of 0.029 ns/channel. The excitation wavelength was 488 nm. The FWHM of the instrument response function (IRF) was ± 130 ps. The recorded decay curves were analyzed with the FAST (Fluorescence Analysis Software Technology) software package from Edinburgh Instruments Ltd. The decay curves were fitted with a three-component exponential function

$$I(t) = \sum_{i=1}^{3} A_i \mathrm{e}^{-t/\tau_i}. \tag{2.19}$$

The goodness-of-fit was judged by the chi-squared value ($\chi^2 < 1.2$) and by inspection of the residuals plot. The average lifetime was calculated by

$$\tau_{avg} = \frac{\sum_{i=1}^{3} A_i \tau_i}{\sum_{i=1}^{3} A_i}. \tag{2.20}$$

2.5 Dynamic light scattering

2.5.1 Working principle

Dynamic light scattering (DLS), also known as photon correlation spectroscopy, is a popular technique to determine the size of dispersed particles in the sub-micron region and down to 1 nm. The technique is based on the fact that, given a certain temperature and viscosity, the size of a particle determines the speed of its Brownian motion. The latter can be represented by the translational diffusion coefficient D. The Stokes-Einstein equation relates the diffusion coefficient D to the particle radius R:

$$D = \frac{k_B T}{6\pi\eta R}, \tag{2.21}$$

with T the absolute temperature, k_B the Boltzmann constant, and η the viscosity of the medium.

In DLS, the sample is illuminated by a monochromatic light source, usually a laser. The incident laser light is scattered by the particles in all directions. At every point in space, the light intensity is determined by the constructive and destructive interference of light scattered by many particles at different locations. A small portion of the scattered light is detected under a certain angle. Because the particles are in constant (Brownian) motion, the interference pattern changes constantly, and the detected light intensity fluctuates in

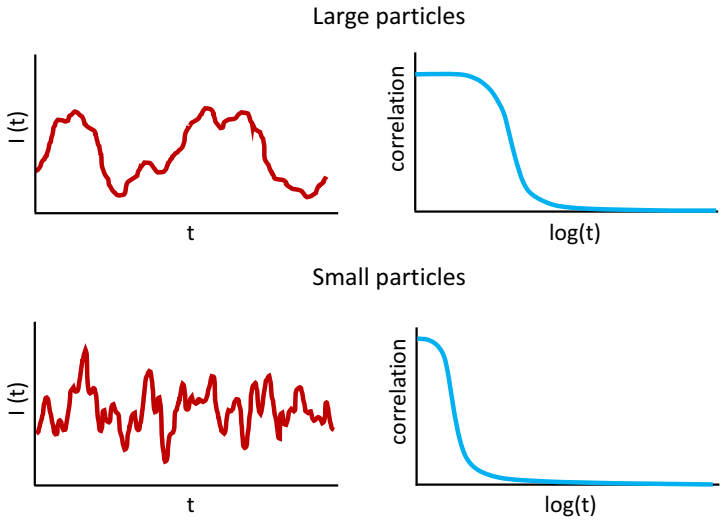

Figure 2.6 – Typical intensity fluctuations and correlation functions for small and large particles.

time. This is illustrated in figure 2.6 for small and large particles. Because large particles diffuse more slowly than small particles, the intensity fluctuations associated with the large particles vary more slowly in time than those of the small particles.

The scattered light intensity is measured over a certain time period (typically seconds) with a certain time step (for instance 1 ns). The rate of change in light intensity is described by the (second order) intensity correlation function, which is obtained by autocorrelation of the measured intensity trace $I(t)$:

$$G_2(\tau) = \frac{1}{N}\sum_{i=0}^{N} I(t_i)I(t_i+\tau). \tag{2.22}$$

Figure 2.6 shows the typical shape of the correlation function for small and large particles. The correlation is large when little time has passed. Particles have moved, but they are still more or less in the same position, such that the intensity is similar. When a larger time period has elapsed, the particle positions will be completely different from their initial positions and the intensity is not related to the initial intensity.

It is more convenient to write $G_2(\tau)$ in its normalized form [77]:

$$g_2(\tau) = 1 + \beta\left(\frac{G_2(\tau)}{G_2(\infty)} - 1\right). \tag{2.23}$$

The parameter β is instrument-related and depends on the optical aperture sizes (especially on the size of the detector pinhole). $G_2(\infty)$ equals the square of the mean intensity, and corresponds to the baseline of the correlation function.

The (first order) electric field correlation function $g_1(\tau)$ describes the dynamics of the superposition of the scattered electric fields. It can be shown that for a monodisperse population of Brownian particles, $g_1(\tau)$ is a single exponential decay:

$$g_1(\tau) = e^{-\Gamma\tau}. \tag{2.24}$$

The decay rate $\Gamma = Dq^2$, with the wave vector q given by

$$q = \frac{4\pi n}{\lambda_0}\sin(\theta/2), \tag{2.25}$$

with n the refractive index of the medium, λ_0 the laser wavelength, and θ the scattering angle. The Siegert equation relates the second-order correlation function with the first-order correlation function $g_1(\tau)$:

$$g_2(\tau) = 1 + |g_1(\tau)|^2. \tag{2.26}$$

Combining equations (2.23), (2.24), and (2.26), we obtain

$$G_2(\tau) = G_2(\infty)\left(1 + \frac{1}{\beta}e^{-2Dq^2\tau}\right). \tag{2.27}$$

The diffusion coefficient D can be determined by fitting the measured correlation function with equation 2.27. The Stokes-Einstein relation can then be used to convert the diffusion coefficient to a particle size. This is called the method of cumulants. It is valid only for samples that have a monomodal size distribution, *i.e.* samples that contain only one type of particle. It gives two numbers: the mean size (Z-average size) and an estimate of the width of the particle size distribution (polydispersity index).

For samples that contain particles with different sizes, the autocorrelation function will not be a single exponential function, but rather a sum of exponentials:

$$G_2(\tau) = G_2(\infty)\left(1 + \frac{1}{\beta}|g_1(\tau)|^2\right), \tag{2.28}$$

with $g_1(\tau)$ given by

$$g_1(\tau) = \sum_i G_i e^{-\Gamma_i\tau}. \tag{2.29}$$

The G_i and Γ_i can be determined by means of a non-negative least squares algorithm. The primary output of the distribution analysis is a distribution of particle sizes called the intensity size distribution.

It is important to note that the reported particle radius is the Stokes radius, *i.e.* the radius of a hard sphere that would diffuse at the same speed as the particle under investigation. The Stokes radius is also referred to as the hydrodynamic radius (R_H) and it is influenced by solvent effects. For instance, the ionic concentration of the medium can affect the particle diffusion speed by changing the thickness of the electric double layer. A low ionic strength medium will produce an extended double layer of ions around the particle, reducing the diffusion speed and resulting in a larger, apparent hydrodynamic diameter [78].

2.5.2 Experimental details

Our measurements were performed with a Malvern Zetasizer nano, equipped with a red laser (633 nm). The Zetasizer software package was used to analyse the correlation functions. The reported DLS sizes are based on the intensity size distribution (distribution analysis).

2.6 Zeta potential measurements

2.6.1 Definition of Zeta potential

Charged particles in aqueous media will attract oppositely charged ions from the solution. These counter-ions form what is known as an electrical double layer around the particles. The electrical double layer consists of two parts: an inner region (the Stern layer) where ions are firmly bound to the particles, and an outer region (the diffuse layer) in which the ions are only loosely associated with the particle. Within the diffuse layer, there is a fictitious boundary called the slipping plane. Ions inside this boundary stay with the particle as it moves in the solution, whereas ions outside this boundary remain in the bulk dispersant. The zeta potential is defined as the electric potential at the slipping plane (see figure 2.7). The zeta potential is an important tool for the determination of the charge state of the nanoparticle surface. The zeta potential will also help to understand the stability of the colloidal dispersion. Zeta potential values typically range from -100 mV to +100 mV. Nanoparticle dispersions with zeta potential values below -30 mV or above +30 mV are usually considered stable, because the nanoparticles experience mutual electrostatic repulsion.

2.6.2 Experimental determination of the zeta potential

Charged particles move in response to an applied electric field and their motion depends on the zeta potential of the particles. Electrophoresis is the movement of colloidal particles relative to the fluid under the action of an externally applied electric field. For uniform and not very strong electric fields, there

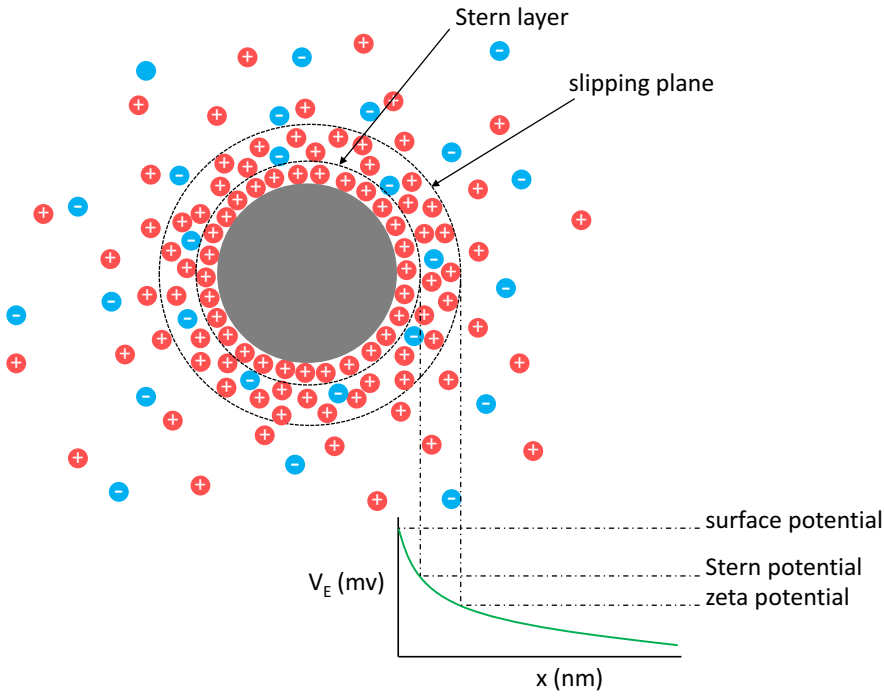

Figure 2.7 – Illustration of the electric double layer around a particle with negatively charged surface. The Zeta potential is defined as the electric potential V_E at the so-called slipping plane.

exists a linear relationship between the electrophoretic mobility U_e and the steady-state electrophoretic velocity $\mathbf{v_e}$:

$$\mathbf{v_e} = U_e \mathbf{E}. \tag{2.30}$$

There exist different electrokinetic models that relate the electrophoretic mobility to the zeta potential [79]. The applicability of these models depends on the ratio of the particle radius a to the Debye length κ^{-1} as well as on the zeta potential value itself. If the ζ potential is presumed to be low (< 50 mV) and for $\kappa a < 20$, Henry's formula can be used to calculate the zeta potential [79]:

$$U_e = \frac{2\epsilon_r \zeta f(\kappa a)}{3\eta}, \tag{2.31}$$

with ϵ_r the relative permittivity, ζ the zeta potential, η the viscosity of the medium, $f(\kappa a)$ the Henry function [80].

There exist several techniques to measure the electrophoretic mobility experimentally. In microelectrophoresis, one directly observes the particle motion with an optical microscope. More automated techniques are the electrophoretic light scattering techniques. The most commonly used method is laser Doppler velocimetry (LDV), which is based on the analysis of the intensity autocorrelation function of the scattered light. The situation differs from DLS because the particles experience not only Brownian motion, but also an electrophoretic velocity attributable to the applied electric field. The electrophoretic velocity causes a Doppler shift in the scattered laser light, which is measured to determine the particle mobility. The Malvern Zetasizer nano uses phase analysis light scattering (PALS), which is a variation of LDV. PALS measures the phase shift caused by the moving particles instead of the frequency shift. PALS is better suited than LDV to measure particles that are moving very slowly (*e.g.* close to the isoelectric point). [81].

2.6.3 Experimental details

Zeta potential measurements were performed with a Malvern Zetasizer nano using DTS1070 folded capillary zeta cells. The voltage applied to the cell electrodes was kept below 100 V. The reported values for the zeta potential are averages of at least three measurements.

2.7 Atomic force microscopy

Atomic force microscopy (AFM) is a scanning probe technique that uses a sharp tip mounted on a cantilever to map the surface topography of a sample. AFM measurements were performed in air using an Agilent 5500 AFM (Agilent Technologies) system operating in the tapping mode. MSNL-10 AFM probes

(Bruker) were employed for image acquisition, thereby using the F triangular cantilever (0.6 N/m spring constant, $90 - 160$ kHz characteristic frequency) on these probes.

AFM images were processed with Gwyddion, an open-source software for scanning probe microscopy data processing [82]. Topography images were levelled by applying a polynomial background function. The *peak* height distributions presented in this thesis are not the conventional height distributions given by Gwyddion. Images were imported into ImageJ and the Find Maxima tool was used to find the peaks that correspond to QD particles on the surface. The peak height distribution is based on the maxima found by ImageJ. A comparison between the conventional and the peak height distribution for a typical AFM topography image is shown in figure 2.8. The conventional height distribution has a first peak at 1.5 nm representing the background and then a long tail which ends in a second peak at approximately 9.5 nm. It is difficult to get an estimate for the average particle height based on this distribution. One approach is to take the difference between the second peak and the background peak, which gives a particle height of 8 nm. The peak height distribution gives directly the average particle height of 9.0 nm ($n = 988$, $\sigma = 1.5$ nm). The average particle height from the conventional size distribution is smaller because it is based on the complete surface of the spherical particles and not only the maximum. The height obtained from the peak height distribution is a better estimate for the particle diameter.

2.8 Electrochemical measurements

The electrochemical measurements were performed with an Interface 1000 potentiostat (Gamry Instruments, Inc.) and a homemade electrochemical cell in a three-electrode arrangement. An Ag/AgCl, 3 M KCl electrode (MI-401F, Microelectrodes Inc.) was used as a reference electrode and a rectangular platinum plate as a counter electrode. Silicon wafer pieces (10×20 mm^2) with sputtered thin gold film (10 nm Ti + 100 nm Au) were used as working electrode. For the photoelectrochemical measurements, the working electrode was illuminated using the monochromator and Xenon light source of a QuantaMaster™ 60 fluorimeter (Photon Technology International). Photocurrent action spectra (photocurrent plotted against light wavelength) were obtained by measuring the photocurrent (50 ms sampling period) while changing the wavelength of the excitation light from 400 to 800 nm. The start and end times of the wavelength scans were used to convert the time scale to a wavelength scale. The power spectrum of the Xenon lamp was measured between 400 and 800 nm with a 5 nm step using a PM100D digital power meter and S130VC (CHECK) photodiode sensor from Thorlabs Inc.

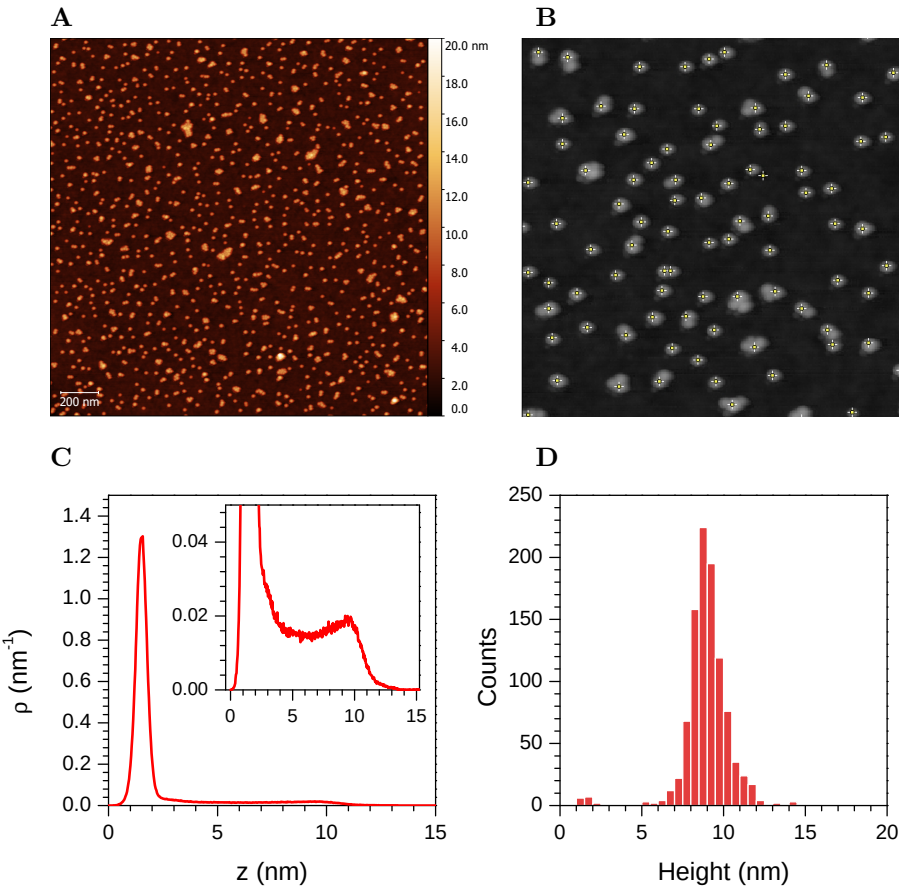

Figure 2.8 – Comparison between the conventional height distribution and the peak height distribution. **(A)** Original AFM topography image of QDs deposited on a Si substrate. **(B)** The same image imported in ImageJ and zoomed in to better discriminate the individual particles. The crosshairs mark maxima found with the "Find Maxima" tool. **(C)** Conventional height distribution given by the AFM processing software. The inset shows a zoom to better see the second peak at 9.5 nm. **(D)** Peak height distribution based on the maxima found by ImageJ.

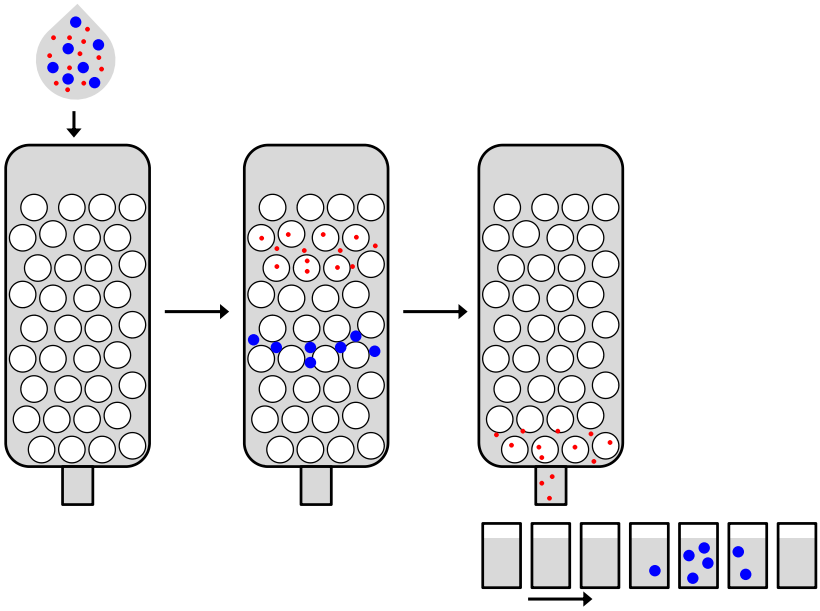

Figure 2.9 – Principle of gel filtration chromatography. A sample containing two different particle sizes is injected at the top of the column containing the gel. The large particles of the sample cannot enter the pores of the gel beads as opposed to the small particles. Consequently, the large particles elute before the small particles.

2.9 Gel filtration chromatography

2.9.1 Working principle

Gel filtration is a chromatographic technique that separates molecules based on their size. Figure 2.9 illustrates the working principle. The setup consists of a vertical column that is filled with a gel. The gel consists of porous beads made from materials such as dextran, acrylamide, and cross-linked agarose [83]. The size of the pores is well-defined and determines the applicable size separation range. A sample containing molecules of different sizes is injected at the top of the column and as it descends through the column (by gravitation or under low pressure), the molecules interact with the gel beads. Small molecules can enter inside the porous beads, whereas large molecules are excluded. The degree of interaction determines the speed of descend through the column. Consequently, the larger molecules elute faster from the column than the smaller molecules. In simple manual columns, the eluent is collected in constant volumes, known as fractions. In more advanced columns, the eluent is constantly monitored by optical methods such as UV-visible spectroscopy, refractometry, *etc.*

2.9.2 Experimental details

We used a home-built setup consisting of an injection port, a 1.0 × 50 cm glass column (cross-sectional area of 0.79 cm^2), a flow adaptor, and a custom-made quartz flow cell. The flow cell design can be found in appendix C. The column was packed with Sephacryl S-400 HR gel medium (GE Healthcare), which has a target size range of 20 – 8000 kDa. The column was equilibrated with borate buffer (0.02 M boric acid, 0.1 M NaCl, pH 8.5). Experiments were performed under a low pressure of approximately 0.2 bar. The eluent was monitored continuously by UV-visible absorption spectroscopy through the optical window of the flow cell.

2.10 Concentrating particle dispersions

A side effect of techniques such as gel filtration or dialysis is sample dilution. Below we discuss two techniques to increase the particle concentration again.

2.10.1 Reverse dialysis

In this technique, the dilute sample is placed in a semi-permeable dialysis bag, which is subsequently covered with dry flakes of poly(ethylene glycol) (PEG). The molecular weight cut-off (MWCO) of the membrane must be chosen such that neither particles nor the PEG polymer can pass through. Therefore, a high molecular weight PEG (*e.g.* 20 kDa) should be chosen. Continuously check the tubing until the desired concentration is reached.

2.10.2 Ultrafiltration using a centrifugal device

Ultrafiltration uses the centrifugal force to filter a solution over a semi-permeable membrane. A centrifugal device typically consists of a tube with a top reservoir that is separated from a bottom reservoir by a semi-permeable membrane. Initially, the top reservoir holds the sample solution. During centrifugation, water and low molecular weight solutes pass through the membrane into the bottom reservoir, while high molecular weight species are retained in the top reservoir. For our experiments we used Nanosep® centrifugal devices with a 10 kDa MWCO Omega™ Membrane.

Chapter 3

Water solubilization of quantum dots

The water solubilization or *phase transfer* of QDs has received considerable attention by researchers from the field. This is because the synthesis of cadmium-based QDs normally takes place in the apolar organic solvent phase, while many promising applications require water-compatible QDs. We explored three phase transfer techniques to find out which technique is most suited for our purpose (combining enzymes with colloidal QDs). The evaluated phase transfer techniques are ligand exchange with dihydrolipoic acid, encapsulation with poly(styrene-co-maleic anhydride), and micelle encapsulation with poly(ethylene glycol)-phospholipids. For each technique, we give the experimental procedure and discuss how the QD properties (*e.g.* PL quantum yield, hydrodynamic size, ...) are affected by the phase transfer.

The chapter is subdivided as follows. In section 3.1, a general introduction is given to the existing methods for the phase transfer of QDs. Section 3.2 gives the properties of the commercial semiconductor nanocrystals that were used in this work, as well as their PL properties in the apolar solvent phase. Section 3.3 discusses the removal of excess native ligands by repeated precipitation. Sections 3.4, 3.5, and 3.6 describe the phase transfer by ligand exchange, phospholipid micelle encapsulation, and polymer wrapping respectively. Finally, in section 3.7, we give an overview of the phase transfer methods and compare them.

3.1 Introduction

The most popular method to prepare Cd-based QDs - the rapid injection of metal and chalcogenide precursors into hot solvent followed by a temperature drop - yields particles that have no intrinsic water solubility. Their surfaces are

covered with organic ligands with long hydrophobic chains such as alkylamines and tri-n-octylphosphine oxide. Phase transfer from an apolar organic solvent to an aqueous solution can be achieved by functionalization of the QD surface with hydrophilic ligands, for which there are several strategies. Most of these strategies can be classified as either ligand exchange or ligand addition.

3.1.1 Ligand exchange

Ligand exchange means the replacement of the native (hydrophobic) ligands with new bifunctional ligands. The new ligands bear on one side an anchoring group that has a high affinity to bind to the inorganic QD surface and on the opposite side a hydrophilic head group to achieve water compatibility. In fact, the anchoring group should have an higher affinity for the QD surface than the native ligand. Thiols are extensively used in ligand exchange. Deprotonated thiols, thiolates, form strong complexes with many metal ions. The affinity of thiolates for the surfaces of noble and coinage metals is well known [84]. Thiols with a functional head group such as an amine or carboxyl group are readily available. Examples of ligand exchange with a thiol-containing ligand include cysteine [85], cysteamine [45], mercaptoacetic acid [86], dihydrolipoic acid (DHLA) [24], PEG-terminated DHLA [87], DHLA-based zwitterionic ligands [88], and even alkylthiol-terminated DNA [89]. Ligand exchange with DHLA is schematically represented in figure 3.1.

Thiol ligand exchange has some attractive features. Firstly, there is a large choice of ligands that is available. Secondly, the procedure is easy to execute. Thirdly, the monolayer of ligands does not add much to the particle size. There are however two major drawbacks to thiol ligand exchange. Firstly, the thiolate-metal bond is fairly weak, because it is a dative (dipolar) bond [90]. As a consequence, thiols suffer from a high dynamic dissociation rate [88]. The shelf life of monothiol-capped QDs is therefore limited (~days). This issue is largely resolved by using bidentate thiols. The cooperative binding of the two thiolate groups extends the shelf life from several weeks to years [88, 91]. The second and perhaps largest disadvantage is that thiol ligand exchange often causes a reduction of the PL quantum yield [92, 93]. This will be further discussed in section 3.4.

3.1.2 Ligand addition

A second strategy is wrapping the hydrophobic QDs with amphiphilic co-polymers. The encapsulation is driven by hydrophobic interactions between the QD native ligands and the hydrophobic parts of the co-polymers. The hydrophilic part of the co-polymers faces the solution side and renders the particles water soluble. Alternatively, the hydrophobic QDs can be buried inside the hydrophobic core of phospholipids micelles. QDs have been encapsulated by using poly(ethylene glycol)-phospholipid micelles [94, 44], poly(styrene-co-maleic

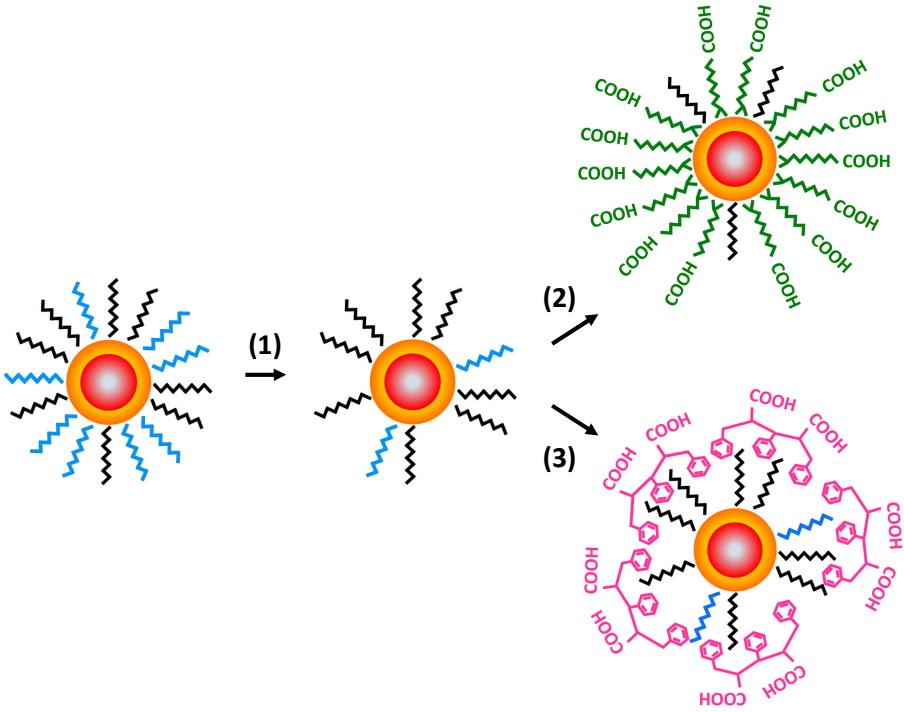

Figure 3.1 – Schematic representation of the organic ligands on the QD surface before and after purification and water solubilization. (1) The traditional purification of QDs by sequential precipitation and redissolution leads to the loss of weakly bound organic ligands from the surface (see section 3.3). The sketch discriminates between weakly bound ligands (in blue) and more strongly bound ligands (in black). (2) Ligand exchange with DHLA replaces the native hydrophobic ligands. Some firmly bound hydrophobic ligands may remain on the surface. (3) PSMA polymer encapsulation retains the native hydrophobic ligands. Hydrophilic groups on the polymer ensure water compatibility.

anhydride) (PSMA) [95], and amphiphilic triblock copolymers [96], among others. The water solubilization of QDs using the amphiphilic polymer PSMA is schematically represented in figure 3.1.

Ligand addition by phospholipid micelle encapsulation solves some of the major problems inherent to ligand exchange. Because of the preservation of the native ligands, the PL quantum yield, that depends strongly on the surface passivation by these native ligands, remains high [94]. Micelle-encapsulated QD also have a long shelf life, the dispersions can be stable months [44]. On the downside, PEG-appended phospholipids are quite expensive. Moreover, the encapsulation with PEG-phospholipids can substantially increase the hydrodynamic size depending on the length of the PEG chains.

Encapsulation with amphiphilic polymers may have the most attractive features. They offer long shelf life and high PL quantum yield, but contrary to PEG-appended phospholipids, these specific amphiphilic polymers can be designed from cheap and widely available polymeric precursors. Also, all of the desired functionalities can be integrated into the polymer chain during the design phase, so there is no need for further functionalization after the phase transfer [97].

3.1.3 Other strategies

Other strategies include the growing of a silica shell around the QDs [98]. The first step to make the silica shell actually consists of a ligand exchange with mercaptopropyltris(methyloxy)silane. The methoxysilane groups (Si-OCH_3) hydrolyze into silanol groups (Si-OH), after which the silane shell can be polymerized through the formation of siloxane bonds. There exist other phase transfer techniques, but a complete overview of all available techniques is beyond the scope of this text. We refer the interested reader to reference [91].

3.2 Commercial semiconductor nanocrystals

Three types of commercial semiconductor nanocrystals were used for the experiments presented in this thesis. These nanocrystals are covered with lipophilic organic ligands, consequently they can be dispersed only in apolar organic solvents. The experimental work was started with Lumidot™ 640 QDs supplied by Sigma-Aldrich. Because Lumidots™ were discontinued in 2014, we continued our work with the similar QSP-630 QDs supplied by Ocean Nanotech. The third type are the CANdot® series A+ QRs supplied by Strem Chemicals Inc.

The specifications of the commercial semiconductor nanocrystals are summarized in table 3.1. Lumidot™ 640 and QSP-630 are very similar particles. They are both CdSe/ZnS core/shell QDs. The Lumidots™ have trioctylphosphine (TOP), triocytlphosphine oxide (TOPO) and hexadecylamine (HDA)

	Lumidot™ 640	QSP-630	CANdot® series A+
Type	dots	dots	rods
Comp.	CdSe/ZnS	CdSe/ZnS	CdSe/CdS
Size	~ 6.3 nm	?	$3-5$ nm x $15-20$ nm
Ligands	HDA, TOP(O)	ODA	ODPA, TOP(O)
λ_{em}	640 nm	630 nm	590 nm
FWHM	$<$ 40 nm	$<$ 25 nm	$<$ 35 nm
QY	$>$ 30%	$>$ 50%	$>$ 60%

Table 3.1 – Properties of the commercial semiconductor nanocrystals according to their specifications.

ligands. QSP-630 QDs possess octadecylamine (ODA) ligands and possibly also some TOP(O) ligands (only limited information concerning the ligands was communicated by the supplier). The emission wavelengths of Lumidots™ and QSP-630 QDs differ by only 10 nm. The FWHM and quantum yield are both better in the case of QSP-630 QDs, suggesting that these QDs are of higher quality than the Lumidots™ in terms of monodispersity and surface passivation. The CANdot® series A+ are CdSe/CdS quantum rods (QRs). They emit in the yellow/orange part of the light spectrum. The ligands are TOP(O) and octadecylphosphonic acid (ODPA). The quantum yield is more than 60%.

The absorption and PL spectra are shown in figure 3.2. For Lumidot™ 640 QDs, the PL peak wavelength is at ~639 nm. The FWHM is $40-41$ nm, and the absolute PL QY is $\sim 37\%$. These values fall within the specifications. For QSP-630 QDs, the PL peak wavelength is reached at 626 nm, the FWHM is ~ 21 nm, and the absolute PL QY is $\sim 47\%$. The PL QY is slight lower than the specification. Finally, for CANdot® QRs, the peak wavelength is found at ~ 578 nm, the FWHM values is ± 25 nm, and the absolute QY is 51%. The peak wavelength differs more than 10 nm from the specified value and also the QY is lower than expected. In summary we conclude that the measured optical properties are close to the specified values, with some deviations for CANdot® QRs.

The absorption of the CdSe/CdS QRS is markedly different from that of the CdSe/ZnS QDs (figure 3.2). The first absorption peak at 570 nm is due to excitation of the CdSe core. At shorter wavelengths, above the absorption edge of CdS, the CdS extinction dwarfs that of the CdSe core and the absorption spectrum is dominated by the shell [99, 100]. The spectral position of the PL emission band shows that the radiative recombination of the photoexcited carriers takes place in the CdSe core [100].

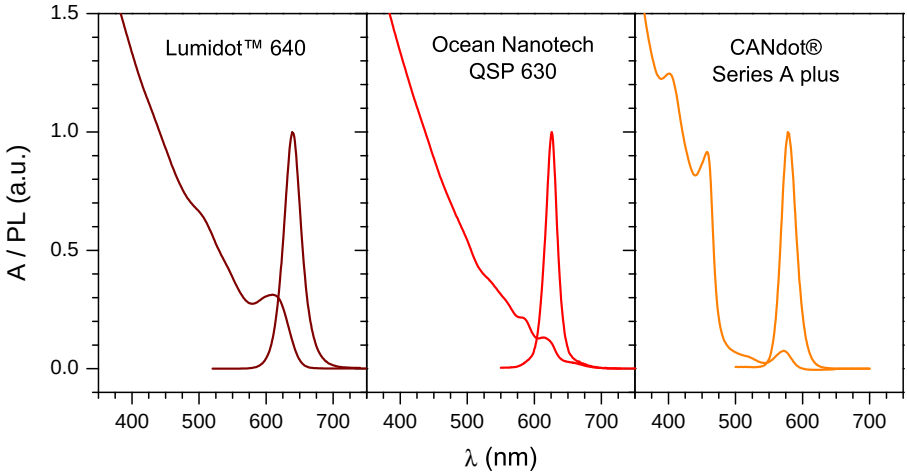

Figure 3.2 – UV-visible absorption spectra and PL spectra (normalized) of the different semiconductor nanocrystals dispersed in organic solvent.

3.3 Removal of excess native ligands

Before the actual phase transfer step, the QD dispersion is usually purified to remove the surplus of ligands in the solvent. A popular purification method is the precipitation of QDs by the addition of a non-solvent followed by centrifugation. Next, the supernatant is removed and the QDs are redispersed with solvent [101]. This purification step can be repeated several times as deemed necessary (we typically used two purification steps). A step-by-step description is given in protocol 3.1.

This purification method comes with two disadvantages. Firstly, a (small) percentage of QDs is typically lost with each purification step. Secondly, the purification step removes reversibly bound QD ligands, thereby affecting the PL quantum yield negatively [101]. For Lumidot™ QDs, the PL brightness diminished visually with each consecutive purification step. The Lumidot™ QDs have hexadecylamine and tri-n-octylphosphine (oxide) surface ligands. Because these surface ligands bind reversibly to the nanocrystal surface, extensive purification will lead to net loss of ligands from the surface. Remarkably, we did not observe a similar decrease in brightness upon purification for the QSP-630 QDs, although these QDs have a similar ligand, namely octadecylamine. The CANdot® QRs also showed a robust brightness. They showed no visual decrease in brightness upon purification. These QRs mainly have octadecylphosphonic acids as organic ligands, with a small amount of other components like trioctylphoshine (oxide).

Morris-Cohen *et al.* showed that for CdSe QDs synthesized in TOPO co-

Step-by-step description:

- Gradually add a polar solvent to the QD dispersion and stop at the first sign of turbidity, which typically occurs at an equal volume of polar solvent and QD dispersion.
- Centrifugate the solution at 1000 g. The QDs should form a pellet and the supernatant should look transparent.
- Discard the supernatant and redissolve the QDs in the native solvent.

Commentary 1: Polar solvents that work well include ethanol, methanol, and a 50/50 mixture of acetone/methanol.
Commentary 2: The centrifugation speed should be optimized for each QD size or type. When the supernatant is coloured after centrifugation, try increasing the centrifugation time. If this does not work, try increasing the centrifugation speed (however, we found that setting the centrifugation speed too high causes irreversible aggregation of QDs).

Protocol 3.1 – Removal of excess ligands

ordinating solvent, successive precipitations using a solvent/non-solvent mixture, result in the loss of the datively (L-type) bound ligands such as HDA, TOPO and TOPSe. On the other hand, X-type ligands such as alkylphosphonates (*e.g.* n-octylphosphonate) and carboxylates form a stable population on the QD surface [102]. Phosphorus NMR studies indicated that phosphorous-containing impurities in technical grade TOPO such as n-octylphosphonic acid are present on the surface of CdSe QDs and that they can be more tightly bound than TOP(O) and HDA. Shakeri *et al.* investigated the choice of non-solvent and the number of processing steps in the traditional purification process [103]. They found, similarly to Mores-Cohen *et al.*, that the datively bound TOPO is almost completely removed from the QD surface after three or four washing steps. The amount of stearic acid, an X-type ligand, on the other hand, while also showing a decrease, plateaus after some washing steps, indicating its stronger coordination to the surface.

An alternative to the traditional method based on sequential precipitation and redissolution is gel permeation chromatography. Gel permeation chromatography is a type of size-exclusion chromatography that uses an organic mobile phase. It is widely used for the characterization of macromolecules such a polymers. The technique can be used to purify monodisperse samples of core and core/shell QDs from synthesis byproducts and excess ligands [104]. This method has multiple advantages over the traditional method, including better reproducibility and efficiency (lower ligand/QD ratio). The method also avoids the exposure of the QDs to a foreign solvent that can perturb the QD surface.

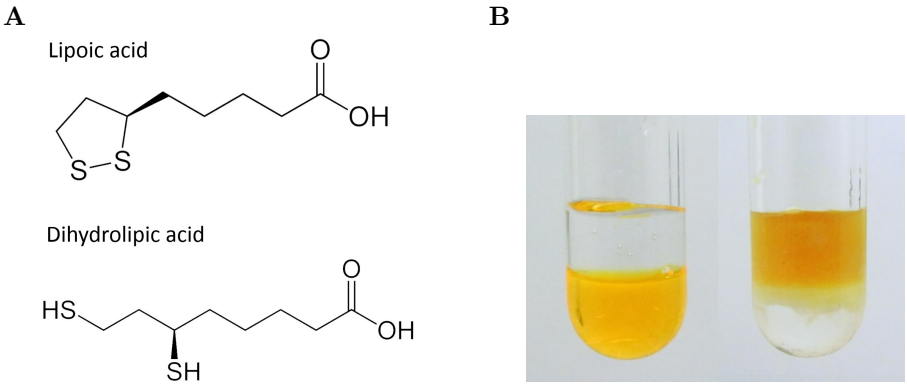

Figure 3.3 – (A) Chemical structure of lipoic acid and dihydrolipoic acid. (B) Water solubilization of yellow CANdot® QRs by DHLA ligand exchange. The QRs were initially dispersed in the chloroform (left tube). After addition of the aqueous solution containing DHLA and vigorous mixing, the QRs transferred to the water phase (right tube). Note that chloroform is more dense than water and thus forms the bottom phase.

3.4 Ligand exchange with DHLA

Dihydrolipoic acid (DHLA) is the reduced form of lipoic acid, an organic compound derived from octanoic acid that has two sulphur atoms connected by a disulphide bridge (figure 3.4A). DHLA is a dithiol and coordinates more strongly to the semiconductor surface than monothiols. This results in a longer shelf life for DHLA-capped QDs compared to monothiol-capped QDs. Remark that thiols are bound to the QD surface as thiolates [105]. Ligand exchange with DHLA is schematically shown in figure 3.1. The experimental details are given in protocol 3.2. Briefly, we used sodium borohydride as a reducing agent to obtain DHLA from lipoic acid. The ligand exchange itself takes place by simply mixing the hydrophobic QDs (or QRs) dispersed in chloroform with an aqueous phase containing the reduced DHLA. A successful ligand exchange is evident from the complete transfer of QDs from the chloroform to the aqueous phase. Figure 3.3B shows a photograph of yellow QRs before and after the ligand exchange. Notice that the QD dispersion appears less bright after phase transfer.

As seen from figure 3.4, the phase transfer has a negligible impact on the absorption spectrum and on the spectral position of the PL spectrum. The PL intensity is however drastically reduced after the ligand exchange (note that the PL spectra in figure 3.4 are normalized). CANdot® QRs for instance, have a PL QY of 51% in hexane, but after ligand exchange with DHLA, the QY is reduced to only 0.5%. The decrease in PL QY is also visible with the naked eye (figure 3.3B). Ligand exchange with thiols is known to be detrimental to the PL

Chemicals required: CdSe/ZnS QDs (1 mg), lipoic acid (1.5 mg), chloroform (0.8 ml), sodium borohydride (10 mg), and borate buffer (5.5 ml, 0.25 M borate, pH 9.0).

Step-by-step description:

- Dissolve 1.5 mg of lipoic acid in 0.5 ml borate buffer.
- Dissolve 9.5 mg (0.25 mmol) sodium borohydride in 1 ml borate buffer. Dilute 5 times to obtain a 50 mM solution.
- Slowly add 0.5 ml of the borohydride solution to 0.5 ml lipoic acid solution and shake for ± 2 hours. Observe that the initially yellow solution becomes colourless.
- Dilute 0.2 ml of QD chloroform solution to 1 ml.
- Add the DHLA solution and vortex for $5 - 15$ min until all the QDs have transferred to the aqueous phase.
- Extract the water (top) phase and perform dialysis to remove unreacted ligands and other chemicals.

Commentary: Sodium borohydride reacts with water in the absence of a base. Its lifetime depends on temperature and on the pH. Therefore we recommend performing steps $1 - 3$ in an ice bath.

Protocol 3.2 – Ligand exchange with DHLA.

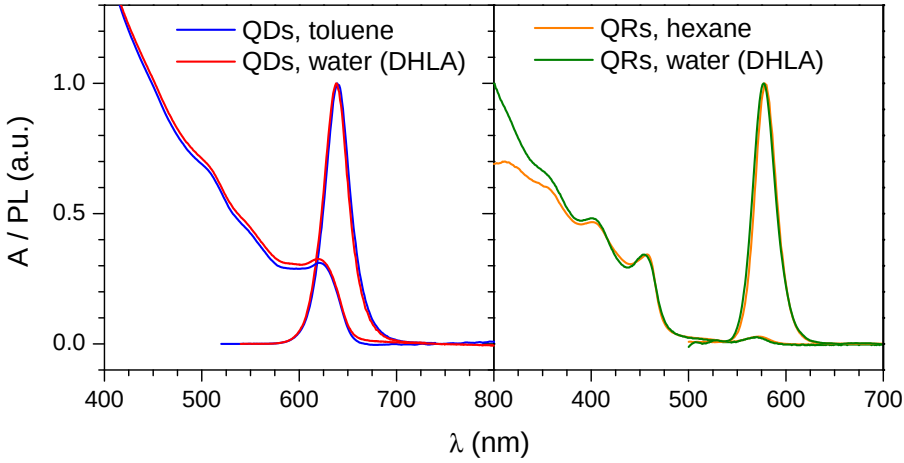

Figure 3.4 – UV-visible absorption spectrum and PL spectrum before and after ligand exchange with DHLA for Lumidot™ QDs (left) and CANdot® QRs (right). Spectra are scaled to allow for better comparison.

QY, but the exact mechanism is complicated and remains under investigation [92, 106, 107, 93]. Jeong *et al.* found that the effect of thiols on QD PL can be both favourable and adverse, depending on the concentration of the thiolate anion ($-S^-$), which is influenced by the initial thiol concentration, the pH, and the exposure time to the thiols [92]. They proposed that thiolates deactivate existing electron traps at low concentrations (enhancing the PL), but introduce new hole traps at high concentrations (quenching the PL). Breus *et al.* compared the quenching efficiency of different thiols. They found that thiols that possessed a carboxyl group (e.g. mercaptoacetic acid) presented an additional quenching pathway [93]. Indeed, Zhang *et al.* showed that carboxyl groups can interact with the surfaces of CdTe QDs in the acidic pH range [108]. These studies show that it is important to consider all the functional groups that are present in the solution for their interaction with the semiconductor surface.

3.5 Phospholipid micelle encapsulation

Phospholipids are amphiphilic lipids that form a major component of all cellular membranes. The hydrophobic part consists of two fatty acyl chains, the hydrophilic part contains a phosphate group and glycerol. In aqueous solutions, phospholipids spontaneously form micelles or lipid bilayers. The favored structure for most phospholipids is the lipid bilayer because the two fatty acyl chains are too bulky to fit into the interior of a micelle [109]. Phospholipids

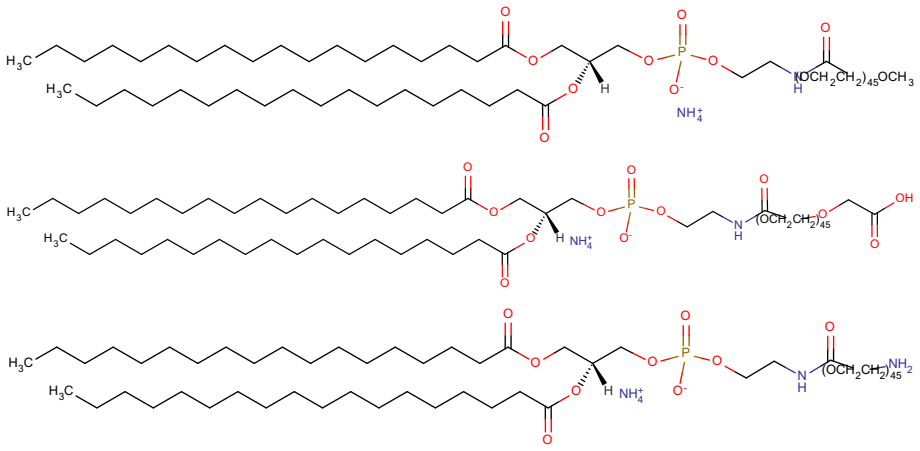

Figure 3.5 – Chemical structure of three PEG-appended phospholipids: DSPE-mPEG 2000 (top), DSPE-PEG 2000 Carboxylic Acid (middle), and DSPE-PEG 2000 Amine (bottom).

can be conjugated to poly(ethylene glycol) (PEG), which makes the polar head group larger such that the micelle structure is favoured over a bilayer structure [110]. Micelles and liposomes (lipid vesicles that consist of a small aqueous compartment surrounded by a lipid bilayer) have been explored as carriers for water-insoluble drugs [110, 44]. PEG-appended phospholipids are commercially available in different flavours in terms of functional groups, chain length, saturation of the fatty acyl chains, *etc.* Figure 3.5 shows the three PEG-phospholipids used in this work.

The encapsulation with PEG-appended phospholipid micelles was found to be an excellent way to render hydrophobic QDs water-soluble [44, 94]. The experimental procedure is described in detail in protocol 3.3. Briefly, phospholipid-micelle encapsulation of QDs is achieved by mixing QDs and phospholipids in chloroform, followed by evaporation of the chloroform and addition of water. Figure 3.6 (left) shows that the PL and absorption spectra of QDs are nearly identical before and after micelle-encapsulation. The PL quantum yield however is reduced after phase transfer by micelle-encapsulation. For these QDs (QSP-630), the PL quantum yield dropped from 47.2% in chloroform to 17.8% in water. As shown in the next section, it is important to use enough PEG-phospholipids to obtain a monodisperse dispersion of QDs in water.

3.5.1 Optimization of the amount of phospholipids

One of the most important parameters in the micelle-encapsulation protocol is the amount of phospholipids. If the amount of phospholipids is too small,

Chemicals required: CdSe/ZnS QDs (1 mg), PEG-phospholipids (2.5 mg), acetone (~5.5 ml), methanol (0.5 ml), toluene (1 ml), chloroform (0.5 ml), ultrapure water (0.5 ml).

Step-by-step protocol:

- Dissolve 2.5 mg of phospholipids in 0.5 ml of chloroform.
- Purify the QD solution by performing the repeated precipitation procedure. After the last purification step, redissolve the QDs with the phospholipid solution.
- Shake for 3 hours. Afterwards, evaporate the chloroform under N_2 flow and add 0.5 ml of H_2O.
- Perform gel filtration chromatography (using *e.g.* Sephacryl S-400 HR) to separate QDs from aggregates and empty micelles.

Commentary: When the obtained water-soluble QDs have low PL QY and/or the absorption spectrum does not look nice, try increasing the amount of phospholipids.

Protocol 3.3 – Ligand addition: PEG phospholipids.

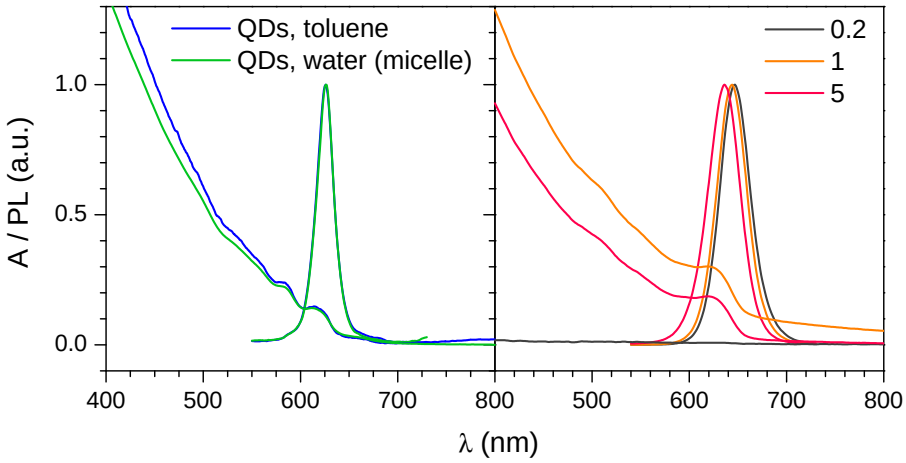

Figure 3.6 – Micelle-encapsulation of QDs. **Left:** UV-visible absorption spectrum and PL spectrum before and after micelle encapsulation of QSP-630 QDs. Spectra are scaled to allow for better comparison. **Right:** UV-visible absorption spectrum and PL spectrum of micelle-encapsulated QDs (Lumidot™) as function of the phospholipid-QD ratio. The mass ratio of phospholipids to QDs is varied between 0.2, 1, and 5.

then micelles may be formed that contain multiple QDs. Consequently, the dispersion becomes more polydisperse. If the amount of phospholipids used is higher than the amount necessary to encapsulate all QDs individually, the excess phospholipids will form empty micelles. Although the empty micelles can be separated from the QDs by ultracentrifugation or gel filtration, this situation is to be avoided as well, because the phospholipid molecules are quite expensive.

Figure 3.6 (right) shows the influence of a variation in the amount of phospholipids. When the mass ratio of phospholipids to QDs is 5, the absorption spectrum appears normal. The PL spectrum has a peak wavelength at 636 nm. At the lowest ratio (0.2), the absorbance goes to zero over the whole visible wavelength range, which is attributable to the sedimentation of the QDs. The PL spectrum[1] has a peak wavelength at 648 nm, a 12-nm redshift compared to the PL spectrum associated with ratio 5. At a ratio of 1, the absorption spectrum reappears, but the baseline is increased. There is non-zero absorbance at wavelengths longer than 620 nm (the first QD absorption peak). The PL spectrum peaks at 644 nm. The increase in baseline of the absorption spectrum at this ratio is most likely due to scattering caused by the presence of large particles. We propose that these large particles are micelles that contain multiple QDs and that form when the amount of phospholipids is low compared to the amount of QDs. At a mass ratio of 0.2, the number of QDs per micelle becomes so high that the micelles sediment, which leads to the disappearance of the absorption spectrum. At a mass ratio of 5, most micelles contain one QD or only a small number of QDs. The inclusion of multiple QDs per micelle could also explain the observed PL redshift. Inside the micelle, the QDs would be closely packed. The small distance between the QDs could enable electronic energy transfer through dipole-dipole coupling [111]. The energy transfer goes from the smaller to the larger QDs in the population, and consequently causes a red shift of the PL emission.

3.5.2 Purification by gel filtration chromatography

As we have seen in the previous section, the dispersion of micelle-encapsulated QDs can contain differently-sized micelles due to varying amounts of QDs inside the micelles. Gel filtration can be used to narrow the size distribution of the dispersion and to separate micelle-encapsulated QDs from empty micelles [94]. A typical gel filtration elution profile of micelle-encapsulated QDs is shown in figure 3.7. The eluent is monitored at five different wavelengths to obtain a signature of the eluting species. For instance, QDs are easy to recognise because they absorb more strongly at shorter wavelengths than at longer wavelengths. The elution profile in figure 3.7 has a trailing shoulder, the origin of which is not clear. Empty micelles are expected to elute after the QDs [94]. However,

[1] The PL spectrum was measured with a Tecan plate reader by a fluorescence top reading. In such a top reading, also sedimented QDs are excited and detected.

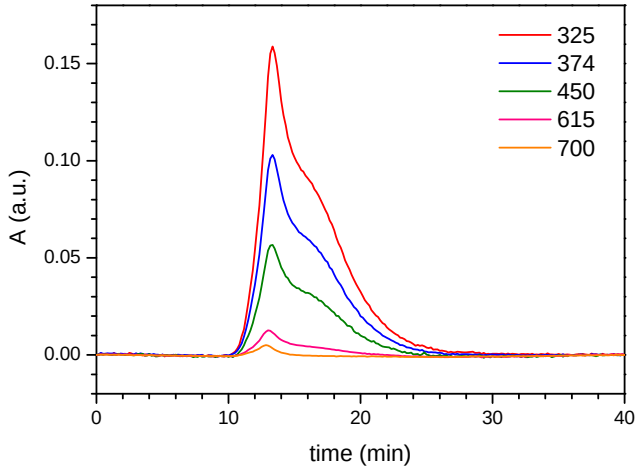

Figure 3.7 – Gel filtration elution profile of micelle-encapsulated QDs. The elution of QDs was monitored at five wavelengths (325, 374, 450, 610, and 700 nm).

their elution may not be observed by UV-visible absorption measurements, because they absorb only weakly in the visible light range. Empty micelles can be detected clearly by measurements of the refractive index [94].

The eluent of interest (between 10 and 30 min) is collected as different size fractions. The PL intensity and absorbance of these fractions is shown in figure 3.8A. Interestingly, the PL intensity profile does not present the shoulder that is present in the absorbance profile. Figure 3.8B shows the PL spectra of some selected fractions. A minute blueshift can be observed as the fraction number increases from 2 to 8. The fractions 2 to 5 also possess an increased tail in the red part of the spectrum. Consequently, the average PL wavelength of the early fractions is redshifted compared to the later fractions (figure 3.8C). Between fractions 2 and 8 there is a ~3 nm spectral shift. Figure 3.8D shows the hydrodynamic radii measured by DLS. The particle size decreases with fraction number, as expected. The hydrodynamic size starts at values above 150 nm (for fraction 2) and approaches 20 nm for the last fractions. We can conclude that the water solubilization process yields a wide distribution of micelle sizes. Micelles of different sizes may indicate a variation in the number of QDs inside the micelles. As discussed in the previous section, we postulate that the spectral (red)shift originates from the close-packing of multiple QDs inside micelles.

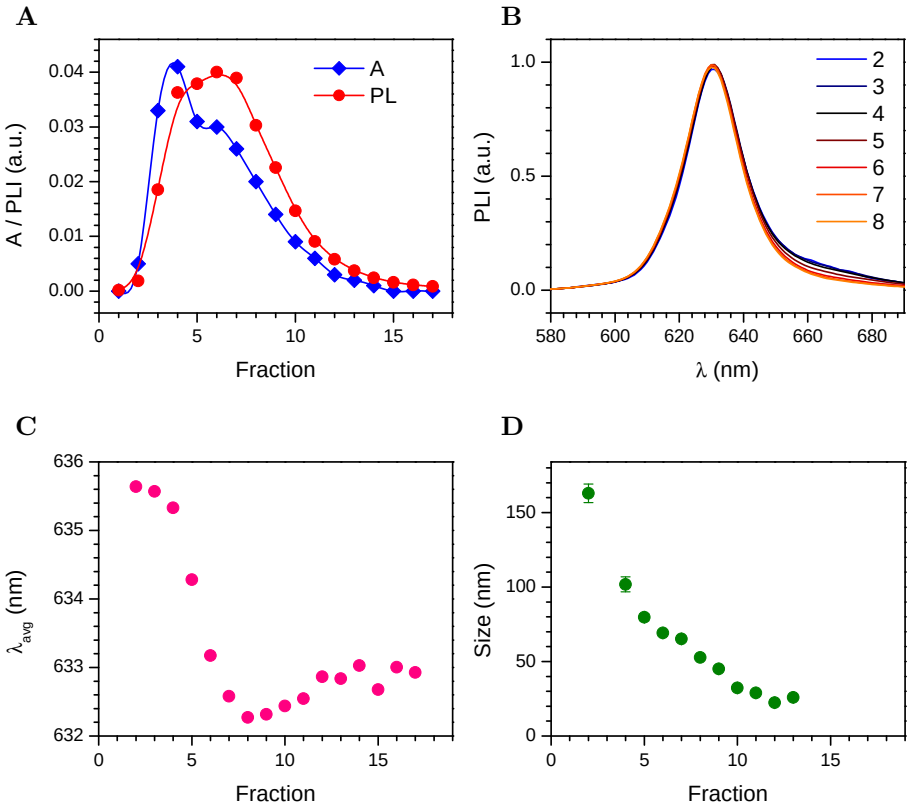

Figure 3.8 – Characterization of the collected gel filtration fractions by optical methods. (A) Absorbance (A) at 450 nm and PL intensity of the collected fractions. (B) PL spectra for fractions 2 to 8. (C) Average wavelength (λ_{avg}) calculated from the PL spectra. (D) DLS size measurements. For fractions 14 to 17, the size could not be measured because the particle concentration was too low.

Poly(maleic anhydride-alt-1-octadecene)
M_r ~ 30,000 - 50,000

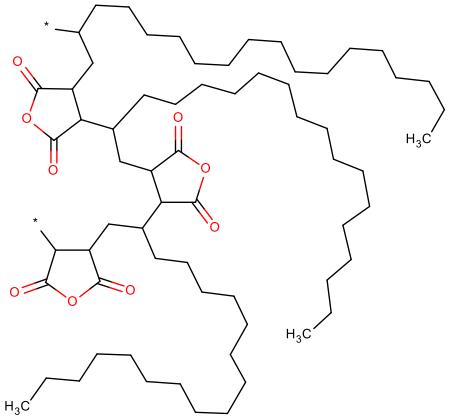

Poly(styrene-co-maleic anhydride)
M_r ~ 1700

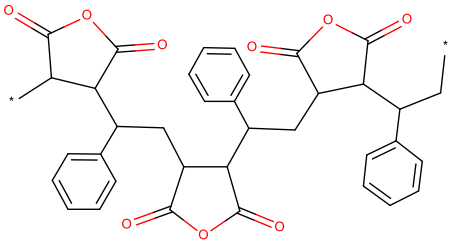

Figure 3.9 – Chemical structure and molecular mass (M_r) of poly(styrene-co-maleic anhydride) (PSMA) and poly(maleic anhydride-alt-1-octadecene) (PMAO).

3.6 Polymer encapsulation

Hydrophobic QDs can be wrapped with amphiphilic polymers to make them water-soluble. We used two different polymers, namely poly(styrene-co-maleic anhydride) (PSMA) and poly(maleic anhydride-alt-1-octadecene) (PMAO), which are shown in figure 3.9. The chemical structure of these two polymers is different only in the hydrophobic part, which is an alkyl chain in the case of PMAO and an aromatic ring in the case of PSMA. Also the polymer chain length is different. For PSMA, low molecular weight polymers are commercially available (down to M_r ~ 1600 g/mol). For PMAO, only high molecular weights are available (M_r ~ 30,000 - 50,000). Short polymers are preferred over long polymers, because the chance that a short polymer interacts with more than one QDs is lower [112]. To prevent the interaction of long polymers with multiple QDs, a larger excess of polymers compared to QDs should be used.

Phase transfer with PSMA is shown schematically in figure 3.1. The experimental details can be found in protocol 3.4. Briefly, the wrapping of QDs with PSMA or PMAO is achieved by mixing the polymers and the QDs in chloroform for several hours and then adding an amine to open the maleic anhydride rings. The biphasic mixture is shaken until all QDs have transferred to the aqueous phase. We have successfully used both ethanolamine and poly(ethylene glycol) methyl ether amine (PEG-amine). Figure 3.10A shows a photograph of the QDs before and after the water transfer. The QD dispersion is clearly less bright after phase transfer, indicating a decrease of the PL quantum yield.

Chemicals: CdSe/ZnS QDs (0.5 mg), PSMA or PMAO (10 mg), ethanolamine (36 µl), chloroform (0.9 ml), ultrapure water (1 ml).

Step-by-step protocol:

- Dilute 100 µl of QDs in chloroform (5 mg/ml) by adding 0.4 ml of chloroform.
- Weigh 10 mg PSMA (6 µmol) or 10 mg PMAO (0.25 µmol) and dissolve the polymer in 0.5 ml chloroform.
- Slowly add the QD solution to the polymer solution.
- Shake for minimum 3 hours.
- Dilute 36 µl ethanolamine (0.6 mmol) in 1 ml UPW.
- For PSMA: add the ethanolamine solution to the QD solution. Shake until all QDs transferred to the aqueous phase.
- For PMAO: evaporate the chloroform. Add the ethanolamine solution to the QD pellet and ultrasonicate.
- (Optional) Extract the aqueous phase containing the QDs and perform dialysis with an appropriate molecular weight cut off to remove excess ethanolamine and polymer.

Troubleshooting: When the phase transfer is incomplete or a mixed phase is created, try increasing the amount of polymer.

Protocol 3.4 – Ligand addition: amphiphilic polymers.

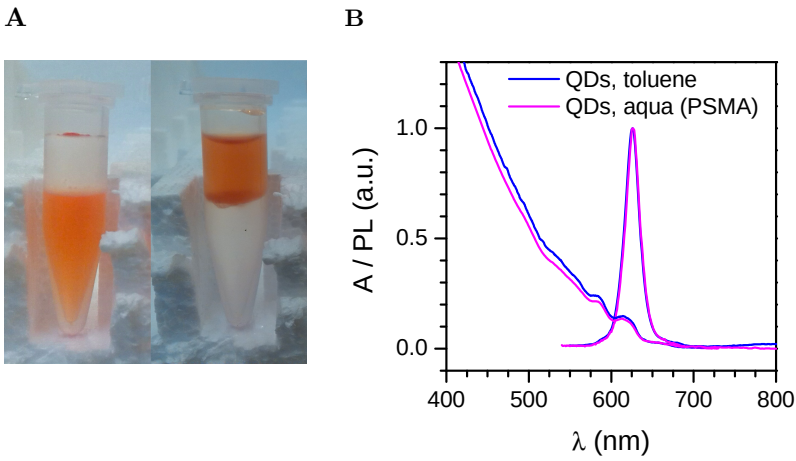

Figure 3.10 – (A) Phase transfer of red Ocean Nanotech QDs by PSMA encapsulation. The QDs are initially dispersed in chloroform (left tube). After addition of an aqueous solution containing ethanolamine and vigorous mixing, the QDs transfer to the water phase (right tube). (B) UV-visible absorption spectrum and PL spectrum before and after phase transfer by PSMA encapsulation for QSP-630 QDs. Spectra are scaled to allow for better comparison.

The UV/visible absorption spectrum and the PL spectrum were not affected by the water transfer (figure 3.10B). The PL quantum yield (~47 % in chloroform) on the other hand was affected negatively by the water transfer and found to be dependent on the ratio of PSMA to QDs. When this ratio was too low (*e.g.* 3.6 mg PSMA for 1 mg of QDs), the transfer was incomplete and the chloroform and water phases could not be separated completely. Water-soluble QDs could be extracted, but their PL QY was low (~6 %). Increasing the ratio (20 mg PSMA for 1 mg of QDs) gave better results in terms of phase separation and PL QY (~20 %).

The above results show that the polymer-to-QD ratio should be sufficiently high for a successful phase transfer and to retain a high PL quantum yield. When using 20 mg ($\sim$ 12 µmol) PSMA for 1 mg ($\sim$ 2 nmol) QDs, the polymer-to-QD ratio is about 6000. In fact, a more relevant figure is the number of polymer monomer units per nm^2 of QD surface [112]. Let us estimate this number in the case of 20 mg PSMA for 1 mg of QDs. The polymer PSMA is composed of styrene and maleic acid units, the former making up 68% (by mass). This corresponds to about 11 styrene units per PSMA strand. The total number of styrene monomer units is therefore $7.9 \cdot 10^{19}$ units ($11 \times 12 \cdot 10^{-6} \times 6 \cdot 10^{23}$). The surface area of a QD is approximately 150 nm^2. The total surface area of QDs in the dispersion is $\sim 1.8 \cdot 10^{17}$ nm^2 ($2 \cdot 10^{-9} \times 6 \cdot 10^{23} \times 150$).

	Ligand exchange		Ligand addition	
	Thiol	Dithiol	PEG-phospholipids	Polymer
Execution	easy	easy	medium	medium
Shelf life	poor	good	good	good
Size increase	small	small	large	medium
PL quantum yield	−−	−−	+	+
Chemical stability	−−	−	+	+

Table 3.2 – Comparison of the phase transfer methods for QDs.

Dividing the number of styrene monomer units by the total surface area gives ~ 440 monomers per nm^2 of QD surface.

3.7 Which method to choose?

The choice of the phase transfer method will mostly be determined by practical considerations. There are large differences between the methods in terms of shelf life, hydrodynamic particle size, photochemical stability, pH stability, and PL quantum yield. The application will determine which of these factors is more important. Table 3.2 briefly compares the methods that we employed.

The PL quantum yield is a very important parameter in many applications (bio-imaging, sensing, *etc.*). Table 3.3 recapitulates the PL quantum yield values obtained for the different water-soluble QDs. In general, the water solubilization of QDs affects their PL quantum yield negatively, irrespective of the QD type and phase transfer method. Between the QD types, the Lumidot™ QDs perform the poorest, both before and after phase transfer. The Lumidot™ QDs were observed to readily lose their native ligands during the removal of excess ligands, which can explain their low QY after phase transfer. Between the phase transfer methods, micelle encapsulation and PSMA polymer encapsulation perform the best.

The method of polymer coating with PSMA would be preferable over phospholipid micelle encapsulation for two reasons. Firstly, PSMA is much cheaper than the PEG-appended phospholipids. Secondly, the increase in particle size is smaller in the case of the polymer coating. However, we encountered a practical problem with PSMA-coated QDs. PSMA-coated QDs (treated with ethanolamine during the phase transfer) were not compatible with the gel matrix used for gel filtration chromatography. Gel filtration is used after the biofunctionalization of the QDs with *glucose oxidase* to separate the functionalized QDs from unbound enzymes (see chapter 7). PSMA-coated QDs were found to interact strongly with the gel matrix and they were retained in the column. We found that using PEG- amine instead of ethanolamine during the phase transfer improved (but not solved) this issue. Phospholipid micelle-encapsulated QDs showed a better passage through the column, although we

QD type		Solvent	Transfer method	QY
Lumidot™ 640 CdSe/ZnS QDs	lot 1	toluene		24
	lot 2	toluene		34.1
		aqua	Micelle (COOH)	1.1
		aqua	PSMA	1.3
	lot 3	toluene		37.6
		aqua	PSMA	1.1
QSP-630 CdSe/ZnS QDs		chloroform		47.2
		aqua	PSMA	6.3
		aqua	PSMA[1]	25.5, 19.1, 20.9
		aqua	Micelle (NH_2)	17.8
		aqua	Micelle (serine)	18.6
CANdots® 590 CdSe/CdS QRs		hexane		50.9
		aqua	DHLA	0.5
		aqua	Micelle (COOH)	45.4

Table 3.3 – Absolute PL quantum yield of QDs and QRs before and after different water transfer methods. The results for the Lumidot™ 640 QDs have been divided over their respective lots (the lots had a slightly different PL spectrum and starting quantum yield). [1]PSMA protocol executed with a higher ratio of PSMA to QDs.

encountered some problems with micelle-encapsulated QDs that have amine functional groups. For the above reasons, we chose to proceed with phospholipid micelle-encapsulated QDs for the biofunctionalization of QDs.

3.8 Conclusion

Prior to the water-solubilization protocol, QD dispersions are usually purified to remove the excess of free ligands in solution. We applied the most popular purification method, which is based on the repeated precipitation and redissolution of QDs while exchanging the supernatant. The downside of this simple purification method is that it can affect the PL quantum yield negatively by causing the loss weakly-bound QD surface ligands. However, only the Lumidot™ QDs seemed to be affected. The PL quantum yield of the QSP QDs and the CANdot® QRs remained robust.

Three water-solubilization methods were successfully applied to transfer QDs from the apolar solvent to the aqueous phase. The first method was ligand exchange with dihydrolipoic acid (DHLA). We observed a huge reduction in the PL quantum yield after applying this method. This PL quenching is inherent to thiol ligand exchange. The second method was encapsulation of QDs inside phospholipid-PEG micelles. The PL quantum yield remained high with this method. The price tag of the phospholipid-PEG molecules encourages the

optimization of the amount of phospholipids used in the protocol. For the lowest phospholipid amount tested, we observed additiontal scattering in the UV-visible absorption spectrum. This was attributed to the presence of large micelles, which most likely contain multiple QDs. Such micelles are undesirable because they precipitate more easily and they increase the size polydispersity. We also observed a PL redshift at the lowest amount of phospholipids. We proposed that this redshift is due to electronic energy transfer between close-packed QDs that reside in the same micelle. Gel filtration chromatography was successfully applied as a post-phase transfer purification step to narrow the size distribution of the particle dispersion. The size fractions containing the largest micelles displayed a (subtle) PL redshift, which supports the idea of electronic coupling inside larger micelles that contain multiple QDs. The third method consisted of coating the QDs with the amphiphilic polymers PSMA and PMAO. This method also retained high PL quantum yield values, but only when a sufficiently high amount of polymer was used. Post-phase transfer purification was required to remove the excess polymer. We found that gel filtration chromatography was not suited to purify PSMA-coated QDs, because the QDs interacted heavily with the gel matrix.

The PL quantum yield was best retained by the PSMA polymer coating method and by phospholipid micelle-encapsulation method. For the biofunctionalization of QDs (chapter 7), we chose to work with micelle-encapsulated QDs, because the polymer-coated QDs could not be purified by gel filtration chromatography (a necessary purification step after the biofunctionalization).

Chapter 4

Quantum dots on surfaces

As stated in the introduction, our goal was to study the interaction between GOX and QDs on two levels: surface-deposited QDs and colloidal QDs. This chapter contains the work done on surface-deposited QDs. Surface-deposited QDs are attractive components for (bio)sensing platforms as well as for solid-state devices (QD lasers, LEDs, and solar cells). In biosensors, QDs may act as the transducer element, converting the biorecognition event (*i.e.* the adsorption of analyte on the sensor surface) into an optoelectronic signal. The QDs can also provide the adsorption sites for the analyte through (bio)functionalization of the QD surface. The surface deposition of QDs is a necessary step because most (cadmium-based) QDs are synthesized in solution. Substrates modified with thin films of QDs adopt the exciting properties of those QDs. For instance, the deposition of QDs on electrodes will provide photoconductive properties to these electrodes. Our goal was the deposition of QDs and GOX on electrode surfaces to study the interaction between QDs and GOX by measuring the electrochemical photocurrent.

The chapter is structured as follows. In section 4.1, we present TEM images of the QDs. In section 4.2, we give a brief literature overview of the most important deposition techniques for QDs, which include self-organisation of hydrophobic QDs by solvent evaporation, binding of QDs onto thiol-modified substrates, and electrostatic adsorption of QDs. In section 4.3, we illustrate the deposition of QDs and QRs on silicon substrates based on electrostatic adsorption. The nanocrystals are characterized by AFM. In section 4.4, we show the thin film deposition of QDs and GOX on thiol-modified gold electrodes. The resulting thin films are evaluated by AFM measurements and by measurements of the electrochemical photocurrent. Section 4.5 gives the conclusions of this chapter

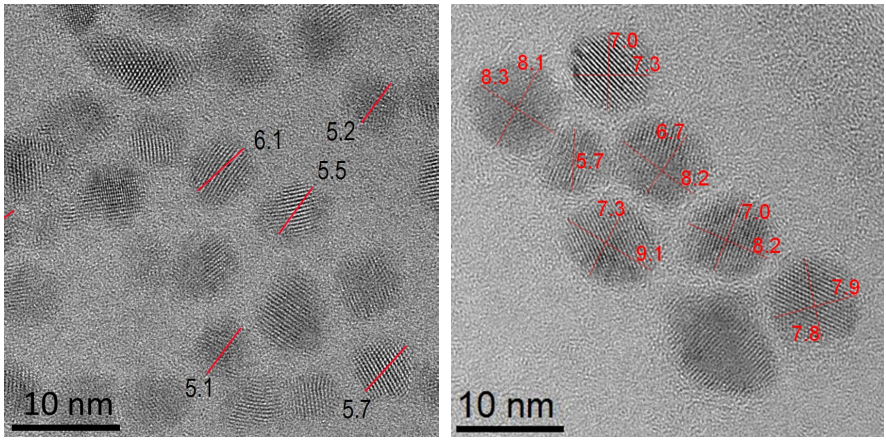

Figure 4.1 – TEM images of phospholipid micelle-encapsulated Lumidots™ QDs (left) and PSMA-coated QSP-630 QDs (right). Particle diameters are marked in red. Experimental details: a few droplets of the QD solutions were deposited on a lacey carbon copper grid. Images were recorded with a Tecnai F30 operated at 300kV.

.

4.1 Characterization by TEM

Figure 4.1 shows TEM images of Lumidot™ 640 QDs and QSP-630 QDs. The crystalline nature of the QDs is clearly visible. However, the core/shell structure of the CdSe/ZnS QDs is not obvious. This may be attributable to the fact that the ZnS shell is too thin (some monolayers) or to the fact that the ZnS shell is grown epitaxially on the CdSe core, and therefore nearly indistinguishable from the core. The average particle size for Lumidot™ QDs is 5.5 ± 0.1 nm ($n = 16$, SD = 0.5 nm). Ocean Nanotech QDs are larger and measure 7.7 ± 0.2 nm ($n = 24$, SD = 0.9 nm). This is surprising because these QDs emit at roughly the same wavelength. Because the particle size determines the emission wavelength, a similar size is expected. Possibly, the difference in particle size is caused by a difference in the thickness of the ZnS shell.

4.2 Surface deposition strategies

Several approaches for the formation of thin films of QDs have been reported in literature. Note that these strategies are usually applicable to nanoparticles in general, and not just to QDs. A first strategy is the self-organisation of hydrophobic QDs into ordered films. Murray *et al.* demonstrated the self-

organisation of trialkylphosphine-capped QDs into ordered thin films through destabilisation of the QD dispersion using established two-solvent recrystallisation methods [113]. The QDs were dispersed in a mixture of 90% octane and 10% octanol. Whereas the QDs form stable dispersions in alkanes, they reversibly aggregate in more polar alcohols. Careful regulation of the temperature and pressure results in the preferential evaporation of the lower boiling octane over octanol, leading to the formation of colloidal crystals. An interesting observation was the redshift of the PL spectrum of the close-packed QDs with respect to that of the solution-dispersed QDs, indicating interdot coupling.

A second method to prepare QD films exploits the binding affinity of Cd-based compounds for thiols. The surface is functionalized with thiols and the QDs are immobilized when their native ligands are exchanged with the solution-exposed free thiol groups. Hu *et al.* functionalized Au surfaces with 1,6-hexanedithiols and glass and ITO surfaces with 3-(mercaptopropyl)trimethoxysilane [114]. They then immersed these substrates alternately in a QD solution and in a 1,6-hexanedithiol solution to prepare a multilayer film of QDs. Stoll *et al.* immobilized QDs onto 1,4-dithiane and 1,4-benzenedithiol modified gold electrodes [115]. Note that the thiol layer provides not only fixation for the QDs, but also blocks unwanted redox reactions at the surface when the substrate is used as an electrode. To improve the interaction of the fixated QDs with biomolecules, the surface of the QDs can be further modified. Stoll *et al.* modified the fixated QDs with mercaptopropionic acid, mercaptosuccinic acid, and 4-mercaptopyridine to optimize the interaction with *cytochrome c*. They found that only 4-mercaptopyridine enabled stable electrochemical interaction. Some authors also report on the immobilization of 1,4-benzenedithiol-capped QDs on gold surfaces [18, 116]. In our experience however, this method does not result in the formation of a good QD film: AFM measurements (not shown) show the presence of large aggregates and a poor distribution of QDs over the surface.

A third way to prepare QD films uses electrostatic interactions between the QD particles and the surface. Tang *et al.* investigated the adsorption of citrate-stabilized QDs on silicon wafers modified with 3-Aminopropyl)triethoxylsilane (APTES), polyethylenimine, and poly(diallydimethylammonium) chloride [117]. The adsorption of QDs at alkaline pH is driven by the electrostatic attraction between the negatively charged QDs and the positively charged aminosilanes or polycations. Jaffar *et al.* used glass substrates patterned with hyaluronic acid, an anionic polysaccharide, for the sequential deposition of cationic and anionic QDs [118]. Zucolotto *et al.* assembled mercaptoacetic acid-capped QDs on glass substrates with two distinct polyelectrolytes, poly(allylamine hydrochloride) and poly(amidoamine), generation 4 dendrimer, via the layer-by-layer technique [119]. They observed that the PL intensity for the PAMAM-QD film was much larger than the PL intensity for the PAH-QD film. Surface-enhanced fluorescence measurements showed that the larger PL intensity is not attributable to differences in film thickness. These results

indicate that the host polymer can have a large influence on the QD PL properties.

4.3 Electrostatic adsorption of QDs on silicon

Figure 4.2 (top) shows micelle-encapsulated Lumidot™ 640 QDs deposited on silicon functionalized with (3-Aminopropyl)triethoxysilane (APTES). APTES is a short silane that can be used to introduce amine groups on the silicon surface. The amine groups are positively charged at neutral pH, while the micelle-encapsulated QDs are negatively charged by virtue of the phosphate and carboxylic acid groups on the phospholipids. Therefore, the particles can bind electrostatically to the surface. The peak height distribution gives an average particle height of 5.3 nm ($n = 2489$, SD = 1.3 nm), which is in good agreement with the size measured by TEM (5.7 nm). Note that the peak height distributions in figure 4.2 are not conventional height distributions as given by typical AFM processing software, but distributions of the peak heights only (see section 2.7). Figure 4.2 (middle) shows micelle-encapsulated QSP-630 QDs. This time, the micelles are composed of amine-functionalized phospholipids, which are positively charged at neutral pH. The QDs are deposited directly on silicon dioxide, which is negatively charged at neutral pH as a result of the deprotonation of silanol groups [120]. The topography image shows that the majority of the deposited particles are individual, single particles. These are micelles that contain only one QD. Aggregates are also visible. These are likely micelles that contain multiple QDs. The average particle height is 9.0 nm ($n = 988$, SD = 1.5 nm), which is slightly larger than the particle diameter measured by TEM (7.6 nm). Figure 4.2 (bottom) shows DHLA-capped CANdot® QRs deposited on a silicon substrate. The elongated shape of the QRs is clearly visible. The peak height distribution reveals two distributions: one centered at 5.5 nm and another one at 10 nm. The distribution at 10 nm is most likely due to the stacking of QRs. The height of 5.5 nm corresponds to the diameter of the rods and is in good agreement with the specified diameter ($3 - 5$ nm).

To have a better view on the particle shape, zoomed images are shown in figure 4.3. The top image shows micelle-encapsulated QDs having a spherical shape. The line profile demonstrates that the lateral dimension (diameter in the XY plane) of the particle is much larger than its height. This is a measurement artefact that can be attributed to the limited sharpness of the AFM tip ("tip convolution effect"). The topography features are convoluted with the tip shape, thereby limiting the lateral resolution. The bottom image shows the bar-like shape of the QRs. The line profile shows that the particular rod in the center of the image has a length of ~42 nm and a diameter of ~13 nm. Because of the tip convolution effect, these numbers are again overestimations of the actual dimensions (the diameter obtained from the height distribution is only 5.5 nm!).

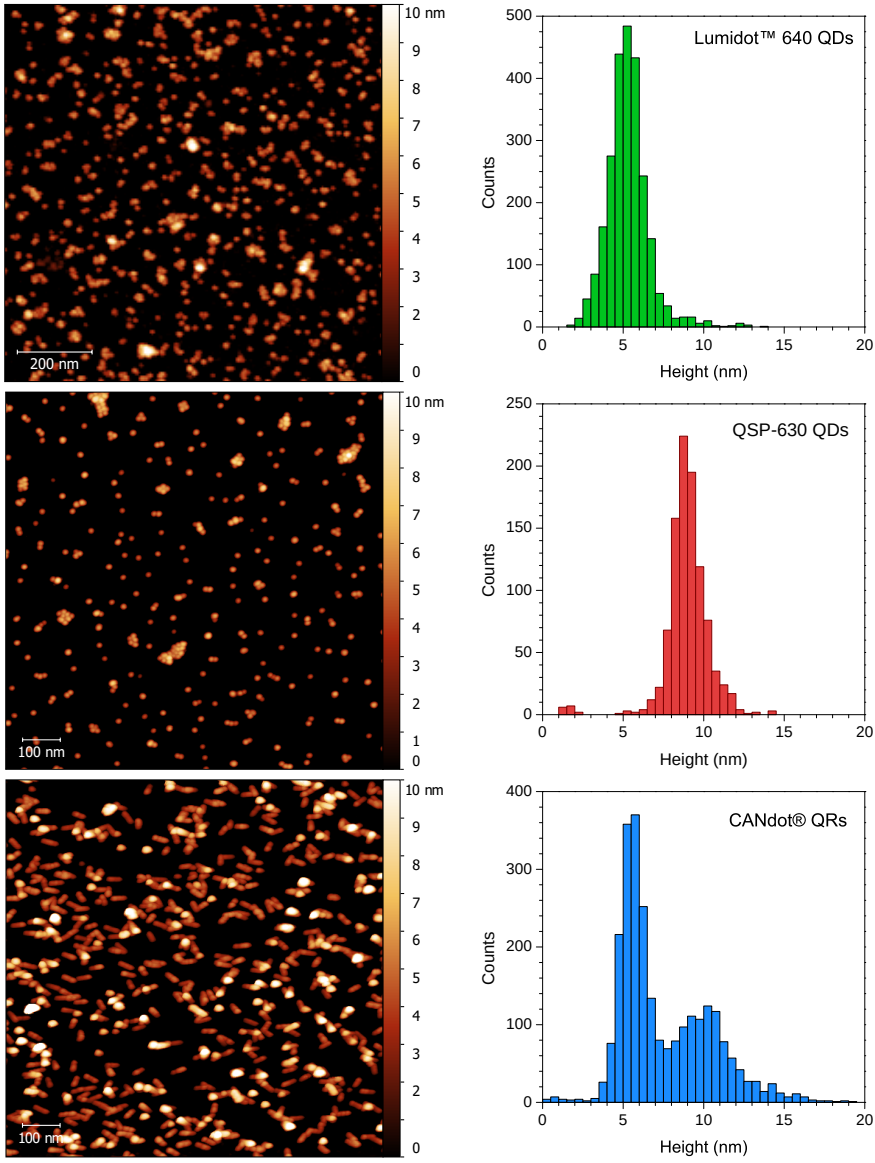

Figure 4.2 – AFM topography images (1×1 µm^2) and particle height distributions (based on larger area scans, > 4 µm^2). **Top:** Lumidot™ 640 QDs encapsulated in phospholipid micelles composed of 10% DSPE-PEG(2000) COOH and 90% DSPE-mPEG(2000). QDs were deposited on a silicon substrate functionalized with APTES. **Middle:** QSP-630 QDs encapsulated in phospholipid micelles composed of 100% DSPE-PEG(2000) NH2. QDs were deposited on a pirahna-cleaned silicon substrate. **Bottom:** DHLA-capped CANdot® QRs deposited on silicon.

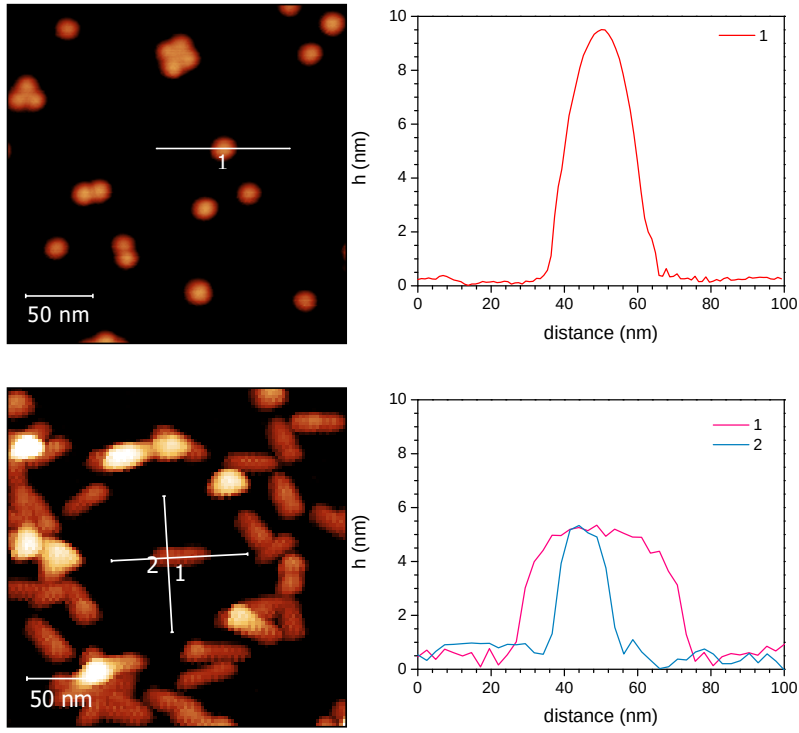

Figure 4.3 – Zoomed AFM topography images of micelle-encapsulated QSP-630 QDs (top) and DHLA-capped CANdot® QRs (bottom). These are zooms of the topography images of figure 4.2. The height profiles on the right correspond to the marker lines in the topography images.

4.4 Immobilization of QDs on gold electrodes

The deposition of QDs on conductive surfaces allows one to observe the photoconductive properties of QDs. These properties can be nicely observed in electrochemical experiments and they can be used in photoelectrochemical sensors. Photoelectrochemical QD-based sensors typically consist of QDs immobilized on an electrode by a linking molecule [121]. Upon illumination, a photocurrent is generated which depends on the type and concentration of the analyte that is present in the immediate environment of the electrode. The immobilized QDs can also be coupled to enzymatic reactions. Katz *et al.* showed the control of the direction of the photocurrent by adding *cytochrome c* in different oxidation states [122]. The photocurrents could be further enhanced by using an biocatalytic cascade based on *cytochrome c* and *lactate dehydrogenase*. Tanne *et al.* built an electrochemical biosensor based on CdSe/ZnS QDs and *glucose oxidase* (GOX) [18]. Benzenedithiol-capped QDs were immobilized on a gold electrode followed by either covalent cross-linking or layer-by-layer deposition of GOX by means of polyallylamine hydrochloride. The oxidation of glucose by GOX is accompanied by the reduction of oxygen. However, oxygen is also the electron acceptor in the photocurrent cascade, accepting electrons from the illuminated QDs. The depletion of oxygen in the vicinity of the QD-modified electrode by the GOX activity suppresses the photocurrent. This configuration enables the biosensing of glucose in the mM range.

In the following sections, we show photoelectrochemical measurements performed on QSP-630 QDs immobilized on gold. Similar to the idea presented by Tanne *et al.*, we attempted to couple the electrochemical photocurrent to the activity of GOX. However, we followed a different approach for the immobilization of QDs and GOX on the gold electrode. Tanne *et al.* performed ligand exchange of QDs with benzenedithiol (BDT) and then deposited the BDT-capped QDs on gold. We have found, by performing AFM measurements on such samples, that this approach does not result in the formation of a monolayer of QDs on the surface. Instead, large aggregates were present, which may already have formed in the solution phase. For this reason, instead of the QDs, we functionalized the surface with BDT. This is also the approach followed by several other groups [115, 114, 116, 123, 16].

4.4.1 Sample preparation

The experimental procedure to prepare the QD-GOX-modified electrode is described in detail protocol 4.1. Briefly, silicon substrates with a thin gold film were functionalized with BDT. BDT was chosen as a linker molecule because it has been shown that short thiols such as BDT and ethanedithiol can enhance the photocurrent through thin films of CdSe QDs compared to other linkers [124]. The thiol-covered surfaces were submerged in a QD (QSP-630) toluene solution overnight. The immobilization of QDs on the BDT layer is based on

Materials: silicon substrates (20 x 10 mm^2) with a thin Au film (10 nm Ti adhesion layer + 100 nm Au), dilute solution of QDs in toluene, 10 mM benzenedithiol in ethanol, 10 mM cysteamine in ethanol, dilute solution of GOX in PBS buffer (10 mM, pH 7.0).

Step-by-step description:

- Clean the substrates by ultrasonication in acetone for 10 minutes. Then rinse successively with acetone, isopropanol, and UPW. Dry under a stream of N_2.
- Submerge the sample in the benzenedithiol solution for 3 hours in the dark. Thoroughly rinse the samples with ethanol and dry under a stream of N_2.
- Submerge the sample in the QD solution and leave overnight. The next day, rinse with ethanol and dry under a stream of N_2.
- Submerge the sample in the cysteamine solution and leave overnight. The next day, rinse with ethanol and dried under a stream of N_2.
- Submerge the sample in the GOX solution for 45 minutes. Afterwards, thoroughly rinse with UPW.

Protocol 4.1 – Preparation of a QD-GOX thin film on gold.

ligand exchange of the native capping ligands with the solution-exposed thiol groups of the BDT layer. Next, these surfaces were treated with cysteamine (CA) to make them hydrophilic. The substrate surfaces before and after cysteamine treatment are schematically shown in figure 4.4A. The change in contact angle is shown qualitatively in figure 4.4B, proving the successful exchange of the native hydrophobic ligands by cysteamine. As a final step, the substrates were submerged in GOX solution to form a layer of GOX on top of the QD film based on electrostatic attraction: cysteamine is positively charged at neutral pH (its amine group has a pKa of 8.27 [125]), while GOX is negatively charged at neutral pH (the pI of GOX is 4.2).

4.4.2 AFM characterization

Figure 4.5 shows AFM topography images at different steps of the surface functionalization. Panel A shows that the topography of bare gold is quite rough, with height variations of more than 5 nm. The high roughness might be explained by the gold deposition process. The gold film was obtained by sputtering first an adhesion layer of Ti (10 nm) on a silicon wafer followed by the sputtering of a thin gold film (100 nm). Panel B shows that the deposition of QDs on the BDT monolayer was successful. A submonolayer of QDs is present on the surface, while large aggregates are absent. Panel C shows that

(A)

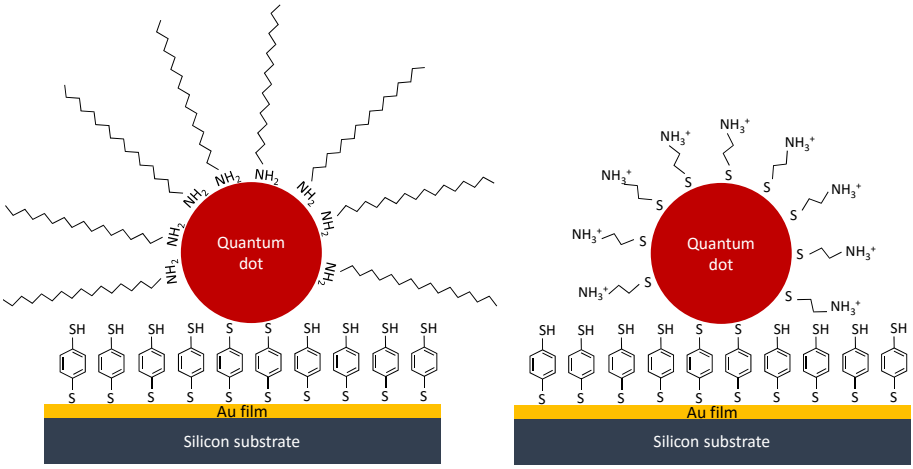

Au+BDT+QDs Au+BDT+QDs+CA

(B)

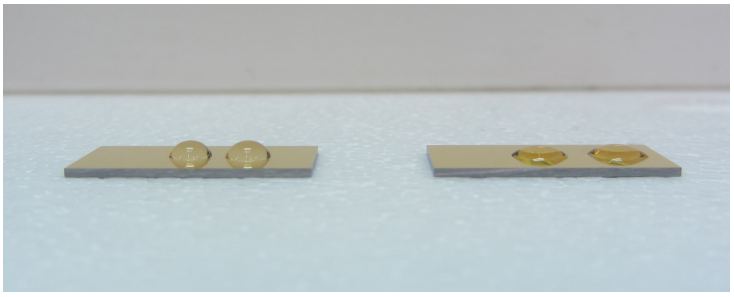

Figure 4.4 – **(A)** Schematic representation of the substrate before and after functionalization with cysteamine (CA). **(B)** Drops of 10 µl UPW on `Au+BDT+QDs` (left) and `Au+BDT+QDs+CA` (right). The contact angle is smaller for the surface that was treated with cysteamine, indicating increased hydrophilicity.

the treatment with cysteamine does not affect the surface distribution of the QDs. Panel D finally, shows the sample after it was submerged in a solution of GOX. The image is quite similar to the topography images shown in panels B and C. This suggests that the functionalization of the surface with GOX may not have been successful.

The peak height distributions corresponding to the above topography images are shown in figure 4.6. The distributions are quite similar for the three samples, although it can be noted that the distribution for `Au+BDT+QDs+CA+GOX` is slightly broader. The average particle heights are 9.4 ± 0.5 nm for the sample `Au+BDT+QDs`, 8.3 ± 0.5 nm for the sample `Au+BDT+QDs+CA`, and 8.9 ± 0.5 nm for the sample `Au+BDT+QDs+CA+GOX`. These results indicate that the average particle height is slightly reduced after the treatment with cysteamine. This can be attributed to the replacement of the long hydrophobic ligands (*e.g.* hexadecylamine) by the shorter cysteamine. The sample `Au+BDT+QDs+CA+GOX` has a slightly larger average particle height than the sample `Au+BDT+QDs+CA`, namely 0.6 nm. One would expect a larger difference between these two samples, because the dimensions of the GOX dimer are approximately $6.0 \times 5.2 \times 7.7$ nm^3 [126]. However, the AFM analysis presented in section 7.4 finds an average height for GOX deposited on silicon of only ~2 nm, which is substantially smaller than the dimensions found by X-ray crystallography for crystallized GOX. Still, proving the presence or absence of GOX requires further investigation by other techniques.

4.4.3 Enzymatic assay

To be conclusive about the presence or absence of GOX on the surface, we executed an enzymatic assay based on the Trinder method used to determine the glucose concentration [127]. The Trinder method comprises a *glucose oxidase/peroxidase* enzyme system in conjunction with a phenol and 4-aminoantipyrine. The reactions involved are:

$$\beta\text{-D-glucose} + O_2 \xrightarrow{\text{GOX}} \text{D-glucono-1,5-lactone} + H_2O_2 \tag{4.1}$$

$$H_2O_2 + \text{4-aminoantipyrine} + \text{phenol} \xrightarrow{peroxidase} \text{quinoneimine dye} + H_2O \tag{4.2}$$

The quinoeimine dye concentration will be proportional to the added glucose concentration and can be determined through Beer's law by measuring the dye absorbance at 510 nm. We adapted the Trinder method to determine the activity of GOX instead of the glucose concentration. In our adaptation we prepared two solutions. The first solution contained glucose and p-hydroxybenzoic acid in PBS buffer and the second solution contained *horseradish peroxidase* (HRP) and 4-aminoantipyrene. The sample substrate to be examined was

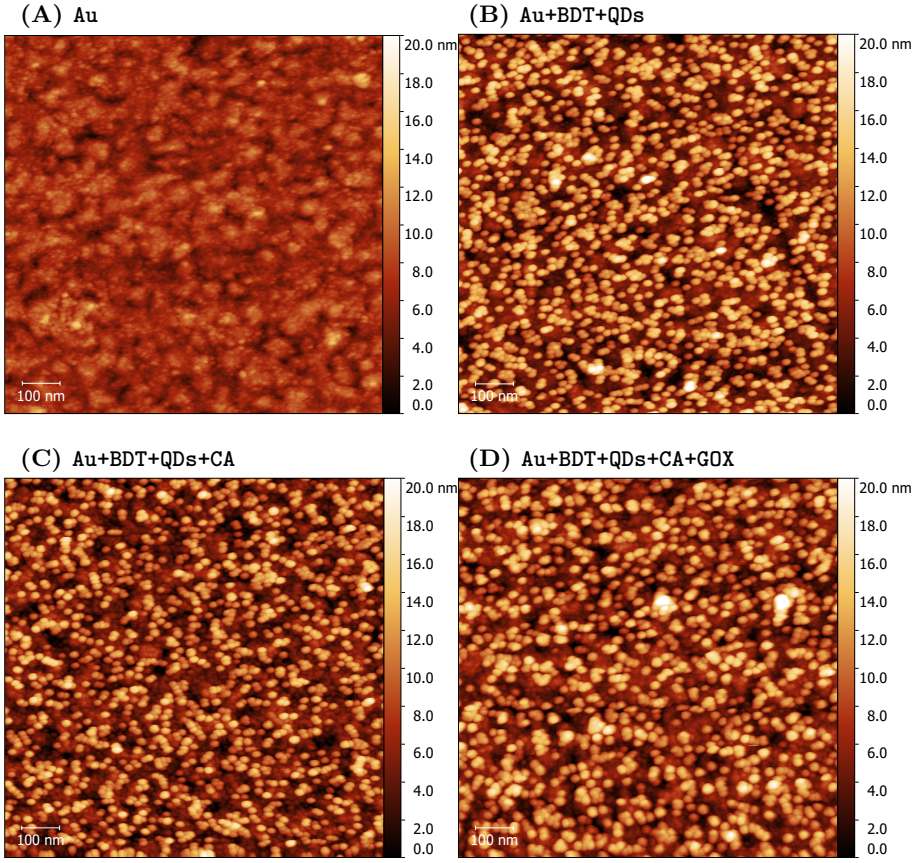

Figure 4.5 – AFM topography images (1×1 µm^2) of the substrate at different steps of the surface functionalization: (A) `Au`, (B) `Au+BDT+QDs`, (C) `Au+BDT+QDs+CA`, and (D) `Au+BDT+QDs+CA+GOX`.

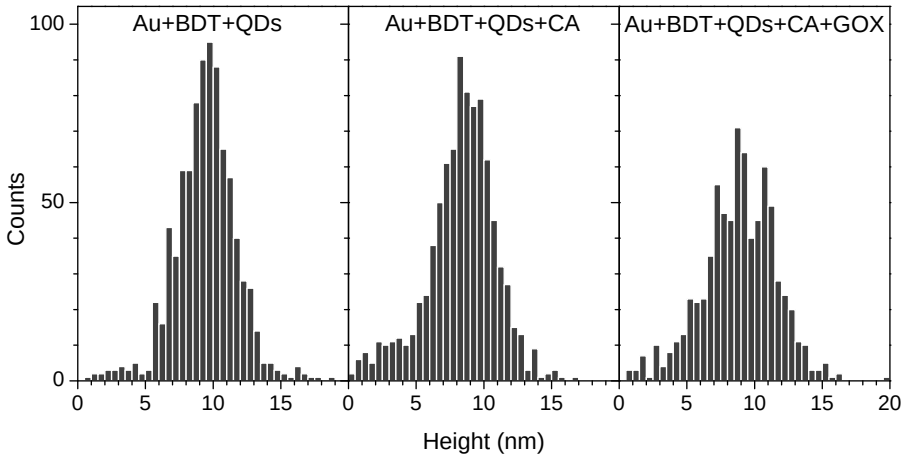

Figure 4.6 – Distributions of particle heights for the topography images of figure 4.5.

placed in a cuvette filled with solution number two, without blocking the optical light path. Then the baseline absorbance was recorded for 10 minutes, after which solution number one was added. This addition caused no detectable changes in the absorbance above the baseline. In a control measurement, no sample was placed in the cuvette and instead of adding solution two, a third solution containing HRP, 4-aminoantipyrene, and GOX was added. This addition gave a sharp increase in the absorbance at 510 nm. These measurements show that there is no appreciable amount of active GOX immobilized on the sample surface.

Together with the AFM measurements we can conclude that the immobilization of GOX was not successful. Most likely, the electrostatic attraction between GOX and the QD film was insufficient to overcome the short-range repulsion (due to overlap of the electric double layers) that prevents electrostatic adsorption. As a consequence, the GOX was washed away during the rinsing step. We note that the buffer we used was of quite low ionic strength (10 mM). Increasing the ionic strength of the buffer may aid the electrostatic adsorption of GOX to the surface by thinning the electric double layers. Also, to increase the electrostatic attraction, the ligand exchange with cysteamine could be replaced by the deposition of a layer of highly-charged polycations.

4.4.4 Electrochemical measurements

Figure 4.7A shows cyclic voltammograms for the samples `Au`, `Au+BDT`, and `Au+BDT+QDs+CA`. Compared to bare gold, the presence of a BDT layer blocks the electrochemical current as expected. The current at negative sample bias

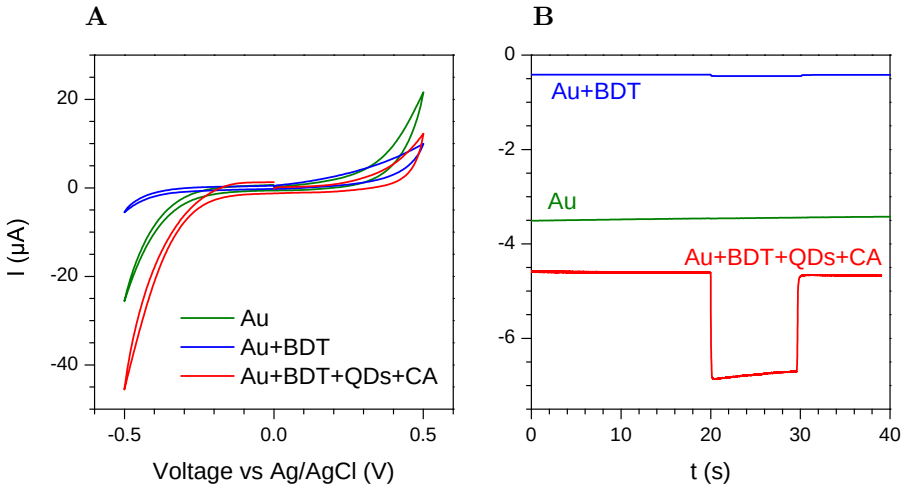

Figure 4.7 – Electrochemical measurements on the samples `Au`, `Au+BDT`, and `Au+BDT+QDs+CA` in 0.10 M HEPES buffer (pH 7.0). **(A)** Cyclic voltammograms recorded at a scan rate of 50 mV/s. **(B)** Photocurrent measurements. Samples were illuminated between $t = 20$ s and $t = 30$ s. The excitation wavelength was 420 nm and excitation power 21 mW. The sample was negatively biased at -350 mV vs Ag/AgCl.

is larger in the case of `Au+BDT+QDs+CA` as compared to `Au`, whereas the situation is reversed at positive sample bias. This indicates that at negative sample bias, electrons can effectively tunnel from the gold film into the QD film. The larger current might be explained by the larger surface area of the nanostructured surface of `Au+BDT+QDs+CA`. Figure 4.7B shows the electrochemical current with and without illumination. The bare gold surface shows no response, while the BDT-covered gold shows a small increase in current upon illumination at $t = 20$ s. The largest increase in current is however seen for `Au+BDT+QDs+CA`, where the current goes from -4.6 µA before illumination to -6.8 µA during illumination.

In order to verify that the photocurrent is indeed mediated by the QDs, the wavelength dependence of the photocurrent was examined. The action spectra of `Au+BDT` and `Au+BDT+QDs+CA` are shown in figure 4.8. For `Au+BDT`, the (small) photocurrent has a maximum around 645 nm. The photocurrent also increases with decreasing wavelength below 550 nm. For `Au+BDT+QDs+CA`, the photocurrent increases towards shorter wavelengths. The as-measured photocurrent (I raw) shows two local maxima, one at 465 nm and one at 615 nm. The first maximum can be attributed to a maximum in the photon flux at this wavelength. Correcting for the photon flux removes this feature in the corrected photocurrent (there is slight overcompensation). The second feature at 615 nm is most likely a signature of the first absorption maximum of the QDs, which

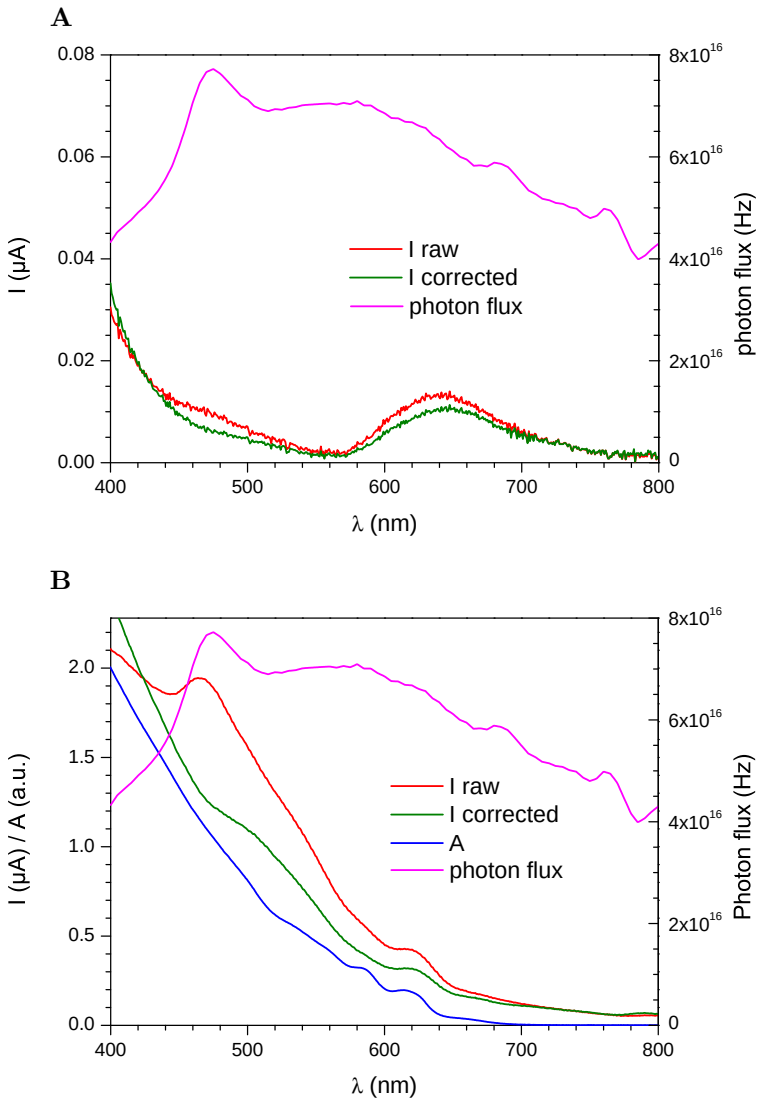

Figure 4.8 – Photocurrent action spectra for **(A)** `Au+BDT` and **(B)** `Au+BDT+QDs+CA`. For both samples, the measured photocurrent (I raw) was corrected for wavelength-dependent variations of the photon flux. For the sample `Au+BDT+QDs+CA` , also the absorption spectrum (A) is shown.

is also situated around 615 nm. This can be regarded as qualitative proof that the QDs are indeed responsible for the generation of the photocurrents. The second absorption maximum at 582 nm is not reproduced in the photocurrent action spectrum. Still, these measurements provide strong evidence that the photocurrent is indeed mediated by the QDs.

4.5 Conclusion

To study the QD morphology, water-soluble QDs and QRs were deposited on silicon substrates using electrostatic adsorption. Negatively charged micelle-encapsulated QDs were deposited on silicon surfaces modified with APTES. Positively charged micelle-encapsulated QDs were deposited directly on piranha-cleaned silicon surfaces. Particle characterization by AFM and TEM showed that a substantial size difference exists between Lumidot™ 640 and QSP-630 CdSe/ZnS QDs. The size difference may be due to differences in the thickness of the ZnS shell.

To investigate the interaction between GOX and surface-deposited QDs, hydrophobic QDs were immobilized on thiol-modified gold electrodes. Thin gold films were sputtered on silicon and then these substrates were successively immersed in solutions of benzenedithiol, QDs, cysteamine, and GOX. AFM characterization showed that all but the last of these steps was successful. An enzymatic assay provided further evidence that the immobilization of GOX was not successful. Electrochemical measurements in a three-electrode configuration were performed using the QD-modified gold electrodes as working electrode. The illumination of the working electrode led to the generation of photocurrents in the µA range. Wavelength-dependent measurements showed that the photocurrent action spectrum resembles the QD absorption spectrum, indicating that the photocurrents are mediated by the QDs.

Chapter 5

Environmental influences on quantum dot photoluminescence

In this and the next chapter we show that the PL of QDs can be affected by environmental factors such as the pH, the ionic strength, electric fields, and particle concentration. We discuss the mechanisms by which these factors affect the PL intensity and/or spectral position. Understanding the influence of these environmental factors is important when studying QDs in a dynamic environment. In the case of QDs and enzymes, the enzymatic activity can cause changes in environmental parameters such as the pH or the ionic strength. Additionally, the enzymatic activity may take place under changing environmental conditions. For instance, the temperature of the solution may drift during the experiment.[1] Knowledge of the environmental parameters that affect the QD PL is therefore a prerequisite to understanding the enzymatic sensing with QDs. After their identification, these environmental parameters can be controlled within a certain range (*e.g.* the pH and ionic strength can be controlled by using buffered solutions), thereby nullifying their effect.

It is important to realize that changes in the PL due to external factors can occur on two levels. Some factors change the PL *extrinsically* on a population level. An example is reabsorption of PL that causes an apparent redshift in the detected PL. Other factors change the PL of the QDs *intrinsically*. An example is the shifting of QD energy levels by electric fields, also causing a redshifted PL.

[1] In general, the PL of CdSe/ZnS QDs is decreased and red-shifted as the temperature increases [128, 129]. The effect of temperature is not further discussed in this text.

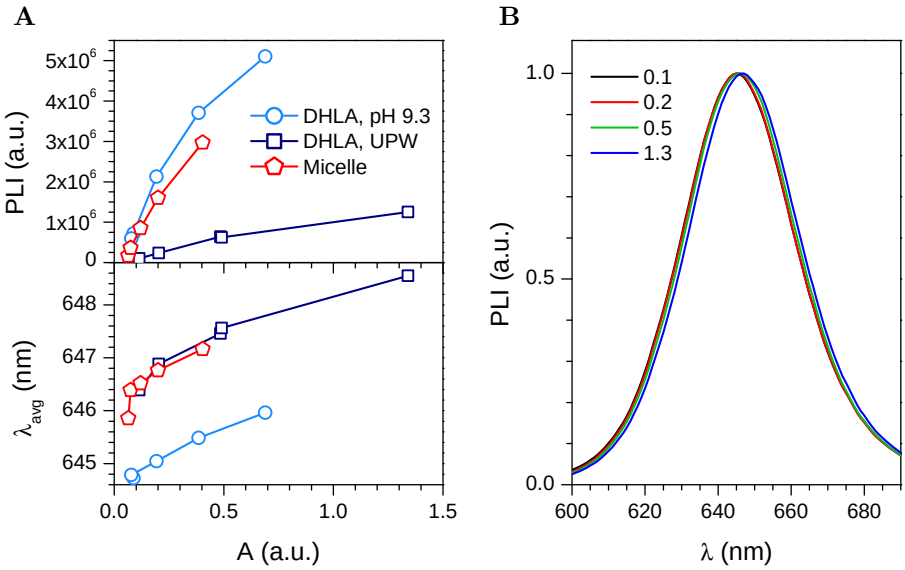

Figure 5.1 – The effect of the QD concentration on the PL. **(A)** PL intensity (PLI) and average emission wavelength (λ_{avg}) versus absorbance (at 500 nm) for three QD preparations (micelle-encapsulated QDs, DHLA-capped QDs in UPW, and DHLA-capped QDs in borate pH 9.3. **(B)** Normalized PL spectra of DHLA-capped QDs in UPW recorded at different absorbances (0.1, 0.2, 0.5, and 1.3).

5.1 Particle concentration

The effect of the QD concentration on the PL is shown in figure 5.1A. The optical properties are plotted versus the absorbance, which is a measure of the concentration. Quite naturally, the PL intensity increases as the absorbance increases. Note that the dependence of the photoluminescence on the absorbance is sublinear. Also, as the QD concentration increases, the average wavelength is redshifted for each of the three samples. Figure 5.1B shows that this shift is real (and not attributable to for instance a baseline artefact). These observations can be explained by the reabsorption of QD emission, a phenomenon that occurs at high fluorophore concentrations when there is spectral overlap between the emission and absorption. Reabsorption leads to a reduced quantum yield and apparent redshift of the PL [66].

Another mechanism that could redshift the PL is electronic energy transfer arising from dipole-dipole interdot interactions [111]. In this case, the electronic energy from an excited QD (the donor) is transferred to another QD (the acceptor). This long-range transfer of electronic excitations requires that the

acceptor has a transition resonant with the donor as well as a lower energy state in which to trap the excitation [111]. As a result, there is a net transfer of energy from the smaller to the larger QDs and the PL of the QD population is redshifted. Electronic energy transfer is efficient only when QDs are within a few nm of each other [111].

The average distance between particles in solution can be found by a simple calculation starting from the molar concentration [130]. In a solution with molar concentration c, there are $c \cdot 6 \cdot 10^{23}$ particles/l or $0.6 \cdot c$ particles/nm^3. The volume occupied by each particle is then $1.67/c$ nm^3. Taking the cube root of this volume gives an indication of the average particle spacing d (in nm):

$$d = \frac{1.18}{c^{1/3}}. \tag{5.1}$$

The molar concentration of QDs can be found from the Beer-Lambert law (using $\epsilon = 5.90 \cdot 10^5$ M^{-1}cm^{-1} [131] and $l = 1$ cm). For $A = 0.3$, we find a concentration of 0.5 µM, which gives an average distance of ~ 148 nm. This spacing is too large for electronic energy transfer to play a role. As discussed in section 3.5, there most likely are micelles that contain several QDs. The separation between QDs in the same micelle would be sufficiently small to enable electronic energy transfer. The content of the micelles (the number of QDs inside) is expected to remain fixed after the phase transfer process. Therefore, electronic energy transfer cannot explain the concentration-dependent PL redshift. Therefore we conclude that the redshift with increasing concentration is due to reabsorption of PL emission.

5.2 Electric fields

It is well-established that semiconductor absorption and emission edges are modulated by an external electric field. This modulation is greatly enhanced in semiconductor nanostructures compared to bulk semiconductors because of the confinement of the exciton [132], giving rise to the quantum-confined Stark effect (QCSE). The presence of a sufficiently large electric field leads to the polarization of the excited state in QDs. The electric field pulls the electron and the hole in opposite directions, resulting in an overall net reduction in the energy of the exciton [132]. Moreover, the reduction in the wave function overlap decreases the PL quantum yield [64, 133].

The electric field strength necessary to induce the QCSE is on the order of 100 kV/cm [134]. It is important to realize that local charges near or on the surface of the QD create electric fields locally that are of similar strength. Imagine a QD with a radius of 3 nm with a single elementary point charge at its surface. Then the electric field at the center of the QD is given by

$$E = \frac{k_e e}{\epsilon_r R^2} \approx 160 \text{ kV/cm}, \tag{5.2}$$

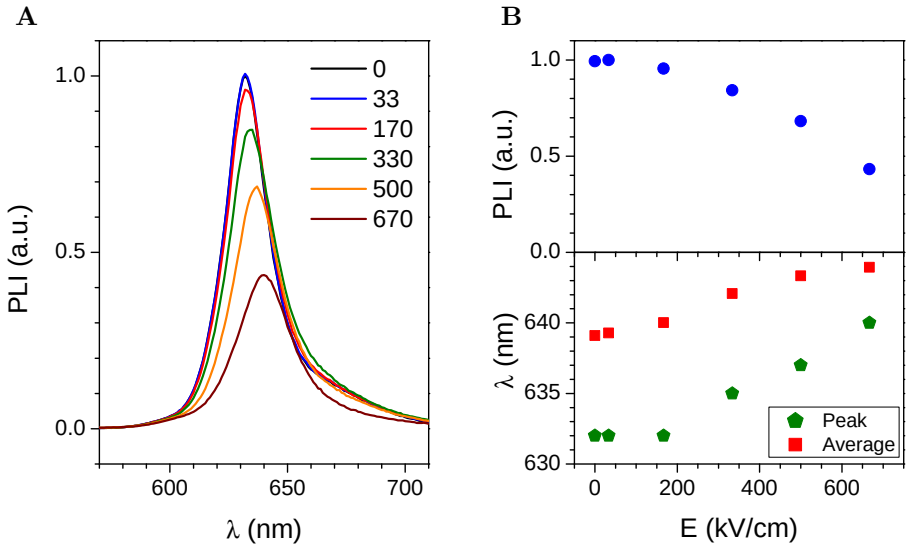

Figure 5.2 – The quantum-confined Stark effect illustrated for a QD ensemble. **(A)** PL spectra of Ocean Nanotech QSP-630 QDs at electric field strengths ranging from 0 to 670 kV/cm. **(B)** Integrated PL intensity (PLI) and PL wavelength (average and peak wavelength) versus the electric field (E).

with k_e the Coulomb constant (9×10^9 N·m^2/C^2), e the elementary charge ($1.6 \cdot 10^{-19}$ C), ϵ_r the static relative permittivity of CdSe (~9.5 [135]), and R the nanoparticle radius.

Several groups have studied the QCSE on single QDs [134, 136, 64, 137, 138]. These studies have revealed valuable insight into the interaction of the excited state with electric fields. A pioneering study by Empedocles and Bawendi showed that QDs have both a polar and polarizable character in the lowest excited state [134]. It was suggested that the polar character stems from charge carriers on or near the QD surface that create local electric fields, thereby inducing an excited state dipole moment. The fluctuation of the local fields over time causes the spectral diffusion (spontaneous spectral shifts typically on the millisecond time scale) observed for single QDs. Later studies confirmed that spectral diffusion is caused by diffusing charges at the QD surface or in the ligand layer [139]. The study of Yacoobi-Gross and co-workers underlined the importance of the organic capping ligands in the QCSE [140]. They showed that a mixed amine-thiol capping layer shifts the emission wavelength depending on the thiol-to-amine ratio. They suggested that a selective arrangement of amine and thiol ligands on the nanocrystal facets creates an internal electric field that Stark-shifts the PL.

In contrast to these works, we tested the QCSE on an *ensemble* of QDs. We deposited QDs on a substrate patterned with interdigitated electrodes. The spacing between the electrodes was 3 µm. The potential applied to the interdigitated electrodes was varied between 0 and 200 V, which resulted in electric fields ranging between 0 and ~670 kV/cm. The QDs were drop-casted from a chloroform dispersion of QDs and then covered with a film of polyvinyl alcohol to protect the QDs from air. This prevented the photo-oxidation of QDs that causes an additional spectral blueshift [139]. Figure 5.2A shows the effect of the applied electric field on the QD PL. A redshift of the PL spectrum is obvious for electric fields of 170 kV/cm and larger. Next to the spectral shift, the PL intensity is quenched. At an electric field strength of 670 kV/cm, the PL intensity has decreased by 57% (figure 5.2B). In conclusion, electric fields (externally applied or originating from local charges) can cause significant changes in the PL intensity and PL average wavelength.

5.3 The ionic strength

The ionic strength of a solution is a measure of the concentration of ions in that solution. For a solution containing n different species of ions, the ionic strength I is given by

$$I = \frac{1}{2}\sum_{i=1}^{n} c_i z_i^2, \tag{5.3}$$

with c_i the molar concentration and z_i is the charge number of ionic species i. The practical relevance for testing the influence of the ionic strength is that QDs used for biological applications (such as cell staining) can be exposed to high salt concentrations. Therefore we need to know if the QD dispersion remains stable at high ionic strengths, and also if the ionic strength influences the PL properties.

Figure 5.3A shows the PL spectra of DHLA-capped QDs at different NaCl concentrations. For ionic strengths up to 10 mM, the PL spectrum is nearly unaffected. For 0.1 M and 1 M NaCl, the PL intensity is decreased and the PL spectrum is redshifted compared to the spectra at low ionic strength. Figure 5.3B shows that the PL average wavelength is shifted by approximately 1 nm. Concurrent with the shift there is a jump in the particle size, which can be attributed to aggregate formation ("salt-induced aggregation"). We believe that the principle mechanism by which the formation of aggregates leads to a spectral shift is electronic energy transfer. The close-packing of QDs within the aggregates could enable the transfer of energy from smaller to larger QDs through dipole-dipole interaction [111].

We have to mention that the effect of the ionic strength on the PL was not univocal. Some measurements showed no clear dependence of the PL on the

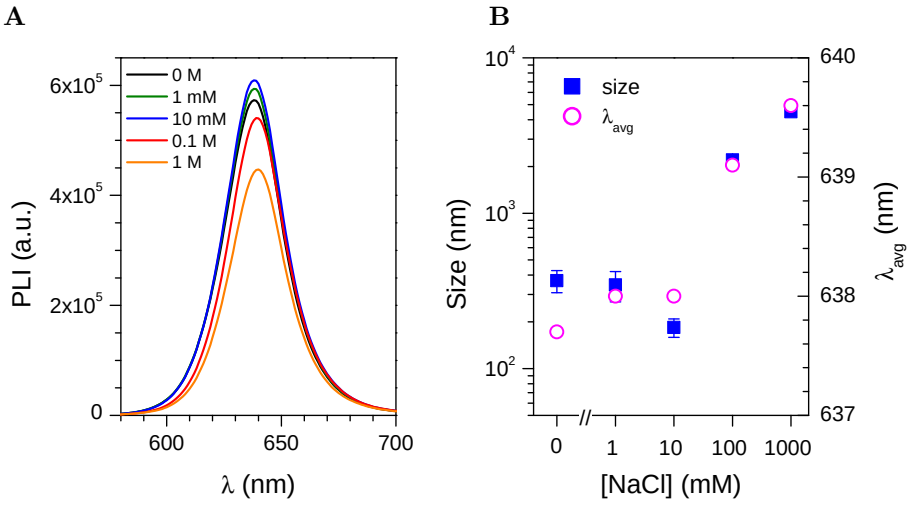

Figure 5.3 – Effect of ionic strength on the PL. **(A)** PL spectra of DHLA-capped QDs recorded at 0, 1, 0.1, 0.01, 0.001 M NaCl. **(B)** Hydrodynamic size (Z-average) measured by DLS and PL average emission wavelength (λ_{avg}) of DHLA-capped Lumidots at different NaCl concentrations.

ionic strength, whereas other measurements revealed a small spectral shift. We believe this is due to the time-dependence of the aggregation process, causing the results to be dependent on the elapsed time between the sample preparation and the measurement. Mattoussi *et al.* investigated the PL intensity of DHLA-capped QDs as a function of NaCl concentration [24]. They found a relatively insignificant drop in PL intensity with increasing salt concentration. Unfortunately, they did not report the PL average wavelength. The extent of aggregate formation at high ionic strength (if any), depends on the QD organic ligands, as shown by the next study. Whereas a dispersion of mercapto-propionic acid capped QDs showed aggregation and a decrease in PL intensity, polymer-coated QDs remained stable up to 5 M NaCl, *i.e.* the UV-visible absorption spectrum did not indicate the presence of aggregates and also the PL intensity remained stable [141].

5.4 Conclusion

In this chapter we presented three factors that affect the PL spectrum of QDs. The first factor was the QD concentration. Our measurements showed a spectral redshift of the PL at high QD concentrations. We attributed this spectral redshift to the reabsorption of PL emission at high QD concentrations. The second factor was the presence of electric fields. For QDs deposited on an

interdigitated electrode chip, the application of strong electric fields caused a reduction in the PL intensity as well as a spectral redshift. At an electric field strength of 500 kV/cm, the PL peak wavelength was shifted by approximately 5 nm and the PL intensity was reduced by ~32 %. These changes in the PL are attributable to the quantum-confined Stark effect (QCSE). The third factor was the ionic strength. Our measurements showed a small spectral redshift of the PL (~1 nm) at large values of the ionic strength ($I \geq 0.1$ M). The spectral shift was accompanied by a substantial increase in the hydrodynamic diameter of the particles, indicating the formation of aggregates. We proposed that this spectral shift is a consequence of electronic energy transfer between aggregated QDs at high ionic strength.

In chapter 6 we discuss the effect of the pH, which was studied in more depth than the three factors presented in this chapter. Studying the influence of environmental factors is important for the correct design and interpretation of the enzymatic sensing experiments. It allows us to consider which parameters should be tightly controlled such that they have no effect on the PL. Additionally, these studies can help to understand the effect of the GOX reaction on the QD PL. For instance, GOX can lower the pH locally by the (indirect) production of gluconic acid.

Chapter 6

pH-sensitivity of quantum dot photoluminescence

In this chapter we illustrate the influence of the pH on the PL of QDs and QRs. Several research groups have reported on the pH-dependency of QD PL. However, few groups have investigated thoroughly the mechanism that underlies the pH-dependency [142, 143]. So while it is known that the PL properties of QDs are pH-dependent, a deep understanding of the phenomenon is lacking. Key questions that remain to be answered pertain to the role of the organic coating in the pH-dependency, to the (ir)reversibility of the PL quenching, and to how the pH-dependency translates to QDs of another material composition.

This chapter is structured as follows. Section 6.1 gives an overview of the current literature concerning this topic. In section 6.2, we give the experimental observations obtained for Lumidot™ QDs. First, an overview of the pH-dependent PL properties (intensity, average wavelength, and lifetime) is given. Then the influence of the organic coating on the pH-dependency of the PL is discussed. Finally, we discuss the reversibility of the pH quenching and study the effect of ageing. In section 6.3 we discuss the possible mechanisms that are causing the pH-dependent PL changes. We show the involvement of three mechanisms, namely acid etching, pH-dependent surface passivation, and the quantum-confined Stark effect. In section 6.4, we compare the pH-dependency of Lumidots™ to that of other (higher quality) QDs and also QRs. Finally, the conclusions of our work are presented in section 6.5.

Parts of this chapter were published as a journal article:

Debruyne, D., Deschaume, O., Coutiño González, l., Locquet, J., Hofkens, J., Van Bael, M., Bartic, C. (2015). The pH-dependent photoluminescence of colloidal CdSe/ZnS quantum dots with different organic coatings. Nanotechnology, 26 (25), 255703.

6.1 Introduction

It is well known that the PL intensity of most water-soluble QDs depends on the pH. Most often it is found that the PL intensity is quenched as the pH decreases. The 1987-work of Spanhel *et al.* is one of the first studies reporting on the pH-dependency of QD PL [144]. They found that decreasing the pH of a solution of CdS QDs was associated with a decrease in the PL intensity and with a shortening of the PL lifetime. Mattoussi *et al.* found that the PL intensity of protein-conjugated DHLA-capped CdSe/ZnS QDs was enhanced at higher pH in the pH range 7-10 [24]. Unconjugated DHLA-capped QDs on the other hand were relatively insensitive in the pH range 7-10. Liu *et al.* investigated mercaptoacetic acid-capped CdSe/ZnSe/ZnS QDs and found that the PL intensity increases monotonically with increasing pH [85]. They also observed a small redshift of the PL with increasing pH. Gao *et al.* studied mercaptoacetic acid capped CdSe/ZnS QDs and found these QDs to be highly sensitive to the pH [107]. Increasing pH values were associated with a higher PL intensity and PL redshift. Yu *et al.* investigated mercaptopropionic-capped CdTe/ZnS QDs, showing that the PL intensity decreased with decreasing pH [145]. The PL intensity could not be restored by adding a base, suggesting that the PL intensity quenching is irreversible. They also observed a redshift of the PL spectrum with decreasing pH. Durisic and co-workers investigated the effect of pH on poly(acrylic acid)-coated CdSe/ZnS QDs functionalized with streptavidin [142, 143]. They measured decreasing PL intensity with decreasing pH in the pH range $6 - 9$.

In contrast to the previously mentioned studies, some studies have reported an increase in the PL intensity with decreasing pH value. Kharlampieva *et al.* studied mercaptoacetic acid-capped CdTe QDs confined in a polyelectrolyte matrix covered with a pH-responsive hydrogel of poly(methyl methacrylate) [146]. They found an increase in the PL intensity at pH 3 compared to pH 8. The PL changes were reversible. Gao *et al.* studied mercaptoacetic acid-capped CdTe QDs and reported an increase in the PL intensity with decreasing pH as well as a PL redshift [147]. The PL intensity changes were again reversible. Zhang *et al.* compared the PL of CdTe QDs capped with mercaptoacetic acid and mercaptopropionic acid [108]. They found that the PL intensity was enhanced in the acidic pH range for both QDs. They also observed a spectral redshift of the PL taking place in the acidic pH range. Finally, CdSe/ZnS QDs capped with poly(ethylene glycol)-appended dihydrolipoic acid (DHLA) were reported to be pH-insensitive over the pH range $4 - 10$ [11].

This literature overview, summarized in table 6.1, shows that the pH-dependency of QD PL is highly variable. The two principle factors that appear to determine the pH-dependency are (quite naturally) the semiconductor material and the organic coating. CdSe/ZnS QDs mostly show a decreasing PL intensity with decreasing pH. Capping these QDs with DHLA is able to render them pH-insensitive. The effect on the emission wavelength (if any) is a spec-

Composition	**Organic coating**	**pH range**	**Effect of pH decrease**		**Ref.**
			PLI	λ_{em}	
CdS		$6-11$	↓, partially reversible		[144]
CdSe/ZnS	DHLA	$7-10$	insensitive		[24]
CdSe/ZnS	DHLA + protein	$7-10$	↓		[24]
CdSe/ZnS	MAA	$2-10$	↓	blueshift	[107]
CdSe/ZnS	PAA + streptavidin	$6-9$	↓, irreversible	none	[142, 143]
CdSe/ZnS	DHLA-PEG	$4-10$	insensitive		[11]
CdSe/ZnSe/ZnS	MAA	$4-10$	↓	blueshift	[85]
CdTe/ZnS	MPA	$4.5-8$	↓, irreversible	redshift	[145]
CdTe	MAA, MPA, PAA	$3-9$	↑	redshift	[108]
CdTe	MAA	$4-11$	↑, reversible	redshift	[147]
CdTe	MAA, in hydrogel matrix	3, 8	↑, reversible		[146]

Table 6.1 – Literature overview of pH-dependency in the PL of QDs. Abbreviations: DHLA = dihydrolipoic acid; MAA = mercaptoacetic acid; MPA = mercaptopropionic acid, PAA = poly(acrylic acid).

tral blueshift. CdTe QDs on the other hand have the reverse pH-dependency, at least for the investigated thiol organic coatings. The PL intensity increases with decreasing pH and the emission wavelength is redshifted.

Despite the varying observations, only a few studies have investigated the pH-dependency in depth to elucidate the mechanisms responsible for the pH-induced PL changes. Durisic *et al.* investigated the effect of pH on immobilized poly(acrylic acid)-coated CdSe/ZnS QDs functionalized with streptavidin by studying the blinking statistics [142]. They measured decreasing PL intensity with decreasing pH in the pH range $6 - 9$. They found that the decrease in PL intensity could be attributed to an increase in the "dark" fraction of QDs (blinking QDs whose PL is below a certain intensity threshold) as well as to a decrease in the PL intensity of the individual QDs. They proposed that H^+ ions play a double role. Firstly, the presence of H^+ ions close to the QD can affect the overlap between electron and hole wave functions, thereby reducing the PL intensity of the "on" state (a demonstration of the QCSE). Secondly, the presence of H^+ ions affects the transition probability to a dark state either by increasing the rate of diffusion to the dark state or by increasing the number of available trap states, or both.

In a sequel work, Durisic and co-workers compared the pH-dependency of the PL of single QDs to that of an ensemble [143]. They made several observations. Firstly, the decrease in PL intensity with decreasing pH is irreversible. Secondly, they found that oxygen plays a pivotal role in the quenching process. Thirdly, only the longest PL lifetime component was found to be pH-dependent, becoming longer with decreasing pH. Fourthly, the PL quenching is accelerated by illumination. Lastly, by comparing the ensemble and single particle PL, they observed that the dark fraction of QDs, which is not observed in the single particle measurements (the PL of dark QDs is below the intensity threshold) contributes to the ensemble PL, and it does so with low PL quantum yield and long lifetime. Based on these observations, they proposed a mechanism in which the ZnS shell is prone to slow decomposition in the presence of acid and oxygen, leading to a sulphur-rich layer at the surface of the QD. As a consequence, the PL quantum yield is reduced because of the presence of trap states on the impaired surface. The trapping of charge carriers at the QD surface also reduces the radiative rate, thus increasing the PL lifetime of those QDs that are part of the dark fraction.

Zhang *et al.* investigated the pH-dependency of thiol-capped CdTe QDs. They observed a peculiar difference between QDs capped with mercaptoacetic acid (MAA) and QDs capped with mercaptopropionic acid (MPA) [108]. For both cappings, the PL intensity increases and then decreases with decreasing pH. However, MPA-capped QDs reach their maximum PL intensity at pH ~6, while MAA-capped QDs reach their maximum at pH ~4.5. The main difference between MAA and MPA is the pK_a value of the carboxylic acid group (3.5 for MAA versus 4.3 for MPA). It was therefore suggested that carboxylic acid groups can interact with the surface, providing surface passivation and

hence increase the PL intensity. This was further investigated by changing the pH in the presence of poly(acrylic acid) (PAA). PAA indeed enhanced the PL intensity in the acidic pH regime. Besides the PL intensity changes, the authors also noticed a PL redshift with decreasing pH value. The redshift was suppressed in the presence of high concentrations of PAA. This further supports the interaction of carboxylic acids with the QD surface. As a final remark, note that the PL redshift in this work was attributed to a sulphuration reaction [147], in line with the mechanism proposed by Durisic *et al.* [143]. However, we would like to point out that the interaction of carboxylic acids with the QD surface would lead to a mixed capping layer (of thiols and carboxyl groups), which is known to cause internal electric fields that can redshift the PL through the QCSE [140]. To determine which of the two mechanisms, the QCSE or a sulphuration reaction, is responsible requires further research. For instance, testing the reversibility of the pH-dependent PL changes could provide further information on the underlying mechanism.

While the studies by Durisic *et al.* and Zhang *et al.* have provided valuable insight, a lot of work remains to be done. Firstly, it is clear from table 6.1 that the hypotheses made in these two works are only valid for specific combinations of QD composition and organic coating. How will the pH-dependency change if one changes the organic coating of the QDs? Secondly, why are the pH changes reversible for some QD systems and irreversible for others? What mechanism can explain reversible pH-dependent changes? Thirdly, little attention has been paid to the pH-dependent spectral shifts that are observed in some studies. Why do some QDs display a blueshift or redshift with changing pH whereas other QDs experience no shift at all?

To address these questions, we have investigated the pH-dependent PL of three types of QDs and for three types of organic coatings, a comparative study which to our knowledge has not been done before. We will discuss the influence of the organic coating and particle type by studying the pH-dependent PL properties, the reversibility of the pH quenching, *etc.* of our systems.

6.2 pH-dependent PL properties of Lumidots™

6.2.1 General observations for micelle-encapsulated Lumidots™

We will start our discussion with the pH-dependent PL properties of Lumidot™ QDs encapsulated with phospholipid micelles. Figure 6.1A shows the PL spectra as a function of the pH. The PL spectrum is quenched at low pH, in accordance with typical observations for CdSe/ZnS QDs (table 6.1). It can also be observed that the PL spectrum is slightly blueshifted at low pH. Figure 6.1B shows the integrated PL intensity versus pH. The largest changes in the

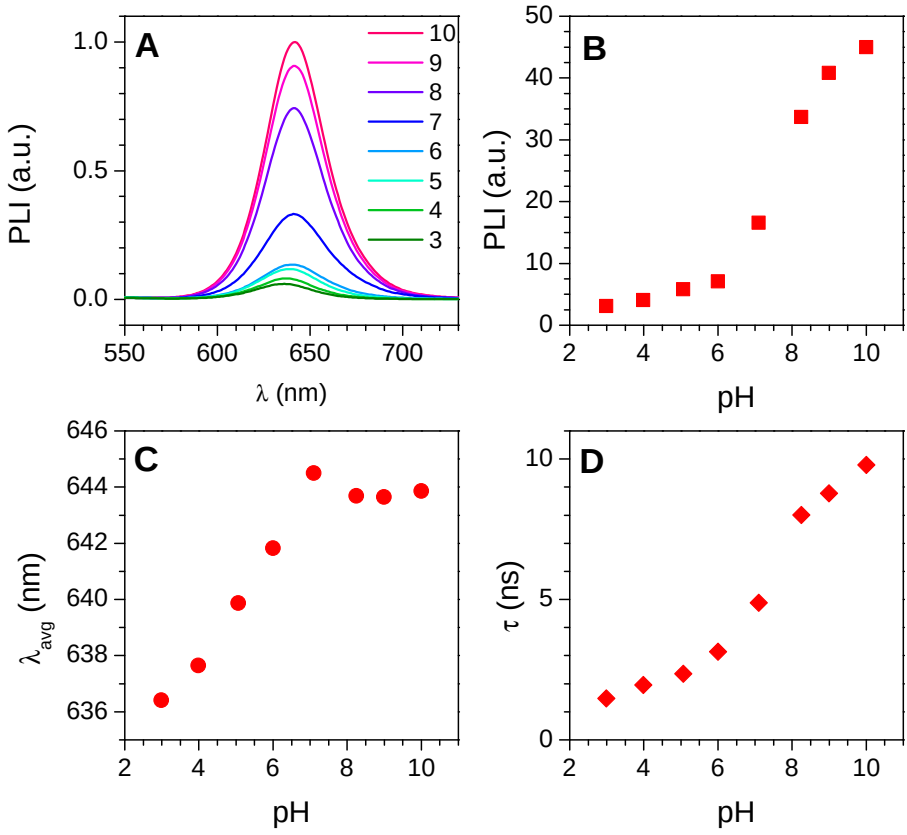

Figure 6.1 – PL properties of micelle-encapsulated Lumidots™ at varying pH. **(A)** pH-dependent PL spectra. **(B)** Integrated PL intensity (PLI) as a function of the pH. **(C)** Average PL wavelength (λ_{avg}) as a function of the pH. **(D)** PL lifetime as a function of the pH. Experimental details: QDs were dispersed in 8 individually-prepared buffered solutions (0.04 M citrate, 0.04 M borate, pH adjusted with NaOH).

PL intensity occur between pH 6 and pH 8. Figure 6.1C shows that the average PL wavelength is blueshifted with decreasing pH. The total spectral shift over the entire pH range amounts to more than 8 nm. Figure 6.1D finally, shows that the PL quenching coincides with a decrease in the PL lifetime (τ). This result is in accordance with the observations of Spanhel *et al.*, who also found a decrease in PL lifetime with decreasing pH value [144], but in contrast to the observations of Durisic *et al.*, who found an increase in PL lifetime with decreasing pH [143].

The PL lifetime τ is given by the inverse of the total recombination rate Γ, which is the sum of the radiative recombination rate Γ_r and the non-radiative recombination rate Γ_{nr}:

$$\tau = \frac{1}{\Gamma} = \frac{1}{\Gamma_r + \Gamma_{nr}}. \tag{6.1}$$

The non-radiative rate itself is the sum of different rates of non-radiative channels such as internal conversion, vibrational relaxation, *etc.* The decrease of the PL lifetime implies an increase in the non-radiative recombination rate. The PL quantum yield Φ can be expressed in terms of the radiative and non-radiative recombination rates:

$$\Phi = \frac{\Gamma_r}{\Gamma_r + \Sigma\Gamma_{nr}}. \tag{6.2}$$

The increase in the non-radiative rate therefore implies a decrease of the PL quantum yield. In other words, the PL quenching can be attributed to a decrease of the PL quantum yield. At this point it is too early to speculate much about the mechanisms behind these pH-dependent changes. We obtained more information on the mechanism(s) by studying the time evolution of the pH-dependency, the influence of the organic coating, and the reversibility of the pH quenching.

6.2.2 Time evolution of the pH-dependency

In this section we show results obtained for DHLA-capped QDs. As the reader will notice, the pH-dependency for DHLA-capped QDs is different from that of micelle-encapsulated QDs. We will discuss these differences in more detail in the next section. Figure 6.2 shows the time evolution of the pH-dependent PL intensity and average wavelength. The PL is quite stable at neutral and basic pH values. The largest changes with time occur in the acidic pH regime between pH values 3 and 6. The PL intensity is progressively quenched in this regime, revealing the instability of the semiconductor surface below pH 6. Changes in the average PL wavelength support the idea that a significant change occurs below pH 6. The monotonous spectral blueshift with decreasing pH switches direction at pH 6, becoming a redshift and then again a blueshift with decreasing pH. Additionally, on day 3 a strong blueshift appears as the pH drops below ~4.5. On day 4, the blueshift is even stronger and starts already

when the pH drops below ~5.2. Another remarkable feature is the crossing of the wavelength profiles at pH 9. Above pH 9, the PL is redshifting with time, while below pH 9, the PL is blueshifting with elapsed time. The reason for this behavior is not clear. The results presented in figure 6.2 show that observations may differ depending on the time of measurement. Some features such as the strong blueshift between pH 4 and 5 are revealed only after several days. This time-dependence, if not paid attention to, may lead to different conclusions concerning the pH-stability.

6.2.3 Influence of the organic coating

It is expected that the organic coating will greatly affect the pH-dependency of the PL properties, because it determines the chemical stability of the semiconductor surface, directly through the surface passivation and in the case of thick organic coatings also indirectly by raising a diffusion barrier against H^+. In chapter 3, we have already seen that the organic coating exerts a large influence on the PL quantum yield. Thiol-capped QDs suffer from a low PL quantum yield, whereas micelle-encapsulated and PSMA-covered QDs retain rather high PL quantum yields.

Figure 6.3 shows the pH-dependent PL intensity and average wavelength for Lumidot™ QDs with three different organic coatings: DHLA, PEG-phospholipid micelles, and PSMA. When comparing the coatings, it is important to keep in mind that the PL intensities in figure 6.3 are normalized for convenience and that the actual PL quantum yields differ greatly. The overall trend of the PL intensity as a function of the pH is similar for the three coatings, namely the PL intensity is decreasing with decreasing pH value. For DHLA-capped QDs, the PL intensity decreases rapidly below pH 6. This is in contrast to the findings of Ji *et al.* who reported pH-insensitivity for DHLA-PEG-capped QDs over the pH range 4-10 [11]. This contradistinction may be due to differences in the quality of the QDs, their history, the slight difference in ligands (DHLA-PEG versus DHLA), or the water-transfer protocol. Above pH 6, the pH-dependency of the PL intensity is quite irregular. Mattoussi *et al.* reported that the PL intensity of their DHLA-capped QDs is pH-insensitive in the range 7-10 [24]. The average PL wavelength is blueshifting with decreasing pH until pH 6. Below pH 6 and with decreasing pH, there is first a redshift of 2 nm followed by a blueshift, with the turning point at pH 5. This pattern is reminiscent of the redshift observed for MAA-capped and MPA-capped CdTe QDs [108].

The pH-dependency of micelle-encapsulated and PSMA-coated QDs is similar. In both cases, the QDs have partially retained their native surface passivation (a substantial part of the weakly-bound native ligands can be lost during the purification step that removes excess free ligands). In both cases, the QDs are encapsulated in the hydrophobic interior of an organic shell. Interestingly, both coatings present a shoulder around pH 6, but it is much more

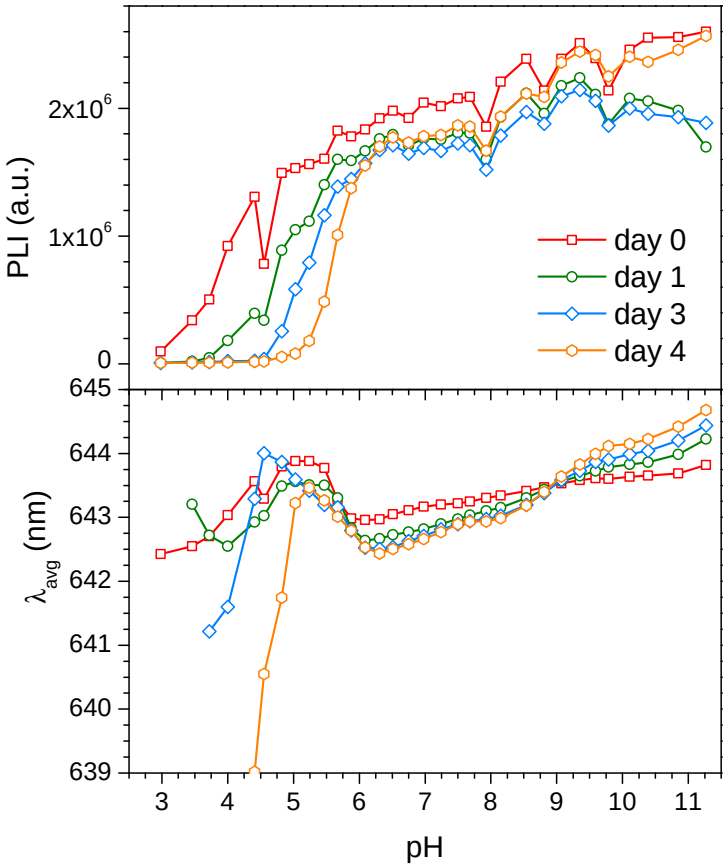

Figure 6.2 – Time evolution of the pH-dependent PL intensity and average PL wavelength for DHLA-capped Lumidots™. Each data point represents an individual sample consisting of QDs dispersed in Britton-Robinson buffer (0.04 M) adjusted to a specific pH value. PL spectra were measured right after preparation (day 0) and after 1, 3, and 4 days.

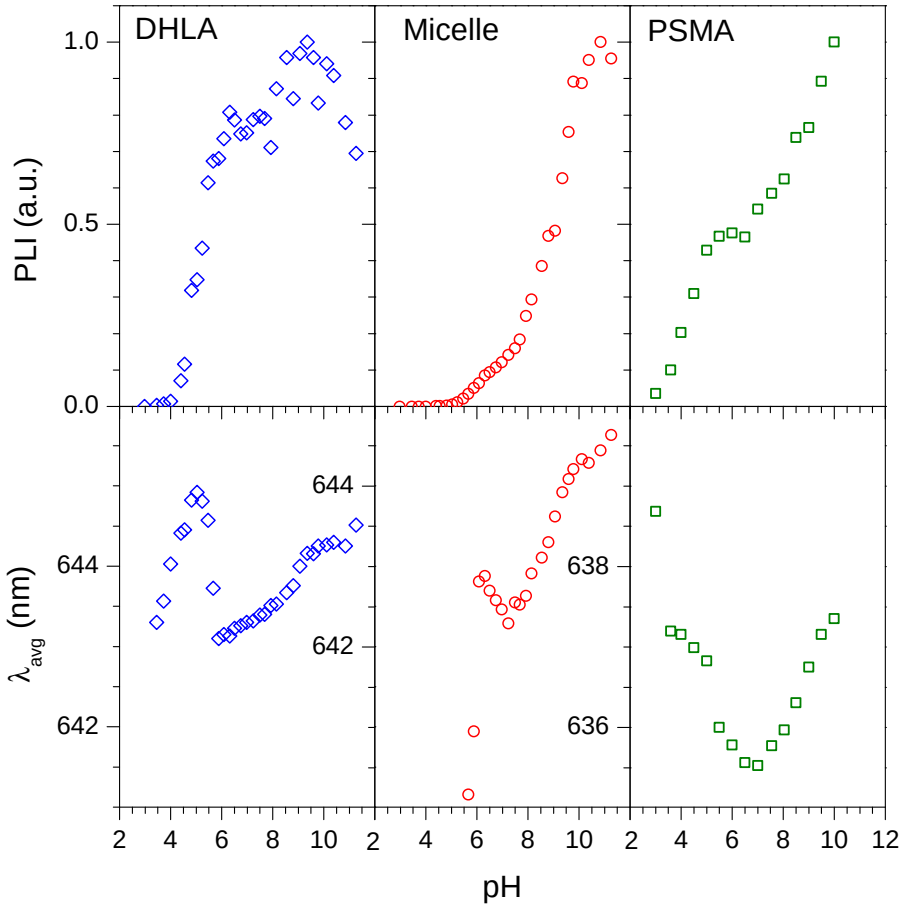

Figure 6.3 – Influence of the organic coating on the pH-dependent PL of Lumidots™. The pH dependency of the normalized PL intensity (PLI) and average PL wavelength (λ_{avg}) is plotted for DHLA-capped, micelle-encapsulated, and PSMA-encapsulated Lumidots™. Each data point represents an individual sample consisting of QDs dispersed in a Britton-Robinson buffer (0.4 M) adjusted to a specific pH value. PSMA-coated QDs were prepared from another batch of Lumidots™ having a slightly shorter emission wavelength.

pronounced for PSMA. The average PL wavelength is blueshifting with decreasing pH between pH 7 and 11. Around pH 7 there is a turning point after which the PL is redshifting with decreasing pH. Notice that the turning point coincides with the start of the shoulder in the PL intensity profile. For micelle-encapsulated QDs, the PL redshift stops at pH 6, below which there is again a strong blueshift. For PSMA-coated QDs, the redshift continues down to pH 3. The coincidence of features in the PL intensity profile and the PL wavelength profile suggests a common underlying mechanism.

6.2.4 Reversibility of the pH-dependent PL

Additional information on the mechanism behind the pH-dependency can be obtained by investigating the reversibility of the quenching process. This was done by exposing the QDs alternately to acidic and basic pH conditions while monitoring the PL spectrum. Figure 6.4A shows the PL properties of micelle-encapsulated QDs and DHLA-capped QDs before, during, and after exposure to pH 5. Upon exposure to pH 5, the PL intensity of both QD types is strongly quenched as expected. When the pH is restored to 9, the PL intensity of micelle-encapsulated QDs recovers almost completely, whereas the PL intensity of DHLA-capped QDs remains quenched. Notice that the change in PL intensity at the transition from pH 9 to pH 5 is more gradual for micelle-encapsulated QDs than for DHLA-capped QDs. Figure 6.4B shows a similar experiment on a shorter time scale and with more pH cycles. For both QD types, each increase/decrease of the pH is associated with an increase/decrease of the PL intensity. Interestingly, the PL intensity of DHLA-capped QDs shows some recovery on this shorter timescale. Overall though, the PL intensity decreases with each pH cycle.

As we have observed earlier, the pH changes also affect the PL emission wavelength. Figure 6.4B shows that the PL intensity quenching upon exposure to pH 5 is accompanied by a spectral blueshift of ~1 nm for DHLA-capped QDs and ~3 nm for micelle-encapsulated QDs. When the pH is restored to 9, the average PL wavelength is redshifted for micelle-encapsulated QDs, but not for DHLA-capped QDs. Interestingly, after the pH has been restored to 9, the average PL wavelength starts to blueshift over time. In figure 6.4B, with shorter exposures to pH 5, the spectral shift is almost fully reversible for micelle-encapsulated QDs and also the DHLA-capped QDs show a reversible component (albeit small and against a rising background). These experiments show that there is both a reversible and irreversible component to the PL changes, and that the irreversible component is larger for DHLA-capped QDs than for micelle-encapsulated QDs.

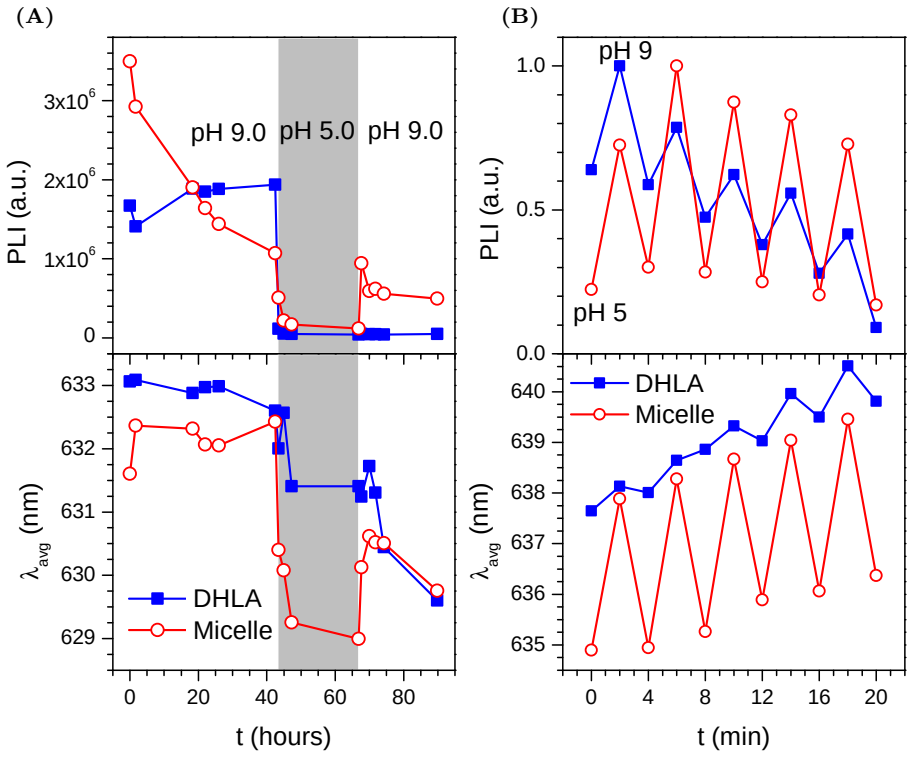

Figure 6.4 – Testing the reversibility of the PL quenching for micelle-encapsulated and DHLA-capped Lumidots™. **(A)** Test on long time scale (hours). The PL intensity (PLI) and the average emission wavelength (λ_{avg}) of the samples was monitored while changing the solution pH from 9 to 5 and then back to 9. The PLI was first allowed to stabilize at pH 9 (for the micelle-encapsulated QDs however, the stabilization was still ongoing after 40 h). **(B)** Test on short time scale with the pH being cycled between 5 and 9 every 2 minutes. Experimental details: QDs were dispersed in citrate-borate buffer (0.05 M). The pH was adjusted by adding small volumes of 1 M HCl/NaOH. PL intensities were corrected for dilution.

6.3 Mechanisms behind the pH-dependency

The results presented in the previous section suggest the involvement of several mechanisms in the pH-dependency of the PL, including irreversible (acid etching) and potentially reversible (pH-dependent surface passivation and the QCSE) mechanisms.

6.3.1 Acid etching

Several authors have described the break down of semiconductor QDs under acidic conditions. Smith *et al.* showed that QDs are dissolved by strong acids [148]. The dissolution of the QDs is evident from the continuous decrease in the optical density of the QDs. They showed that the dissolution rate is dependent on the organic coating and that polyethylenimine-coated QDs are the most acid-resistant. Durisic *et al.* suggested a mechanism of slow decomposition of the ZnS shell in the presence of acid and oxygen in the pH range $6 - 9$ [143]. They proposed that the decomposition is associated with the formation of a sulphur-rich layer, making it a self-inhibiting process. In this case, acid etching can be understood as a process that changes the chemical composition of the QD near its surface.

In our experiments, the occurrence of acid etching is evident at low pH values (≤ 5). In this pH regime, we were unable to measure the absorption spectrum of the QDs after some time (~days), indicating the complete dissolution of QDs. At pH values above 5, the absorption spectrum appeared normal and we did not observe a spectral blueshift, meaning that there were no changes in the size of the CdSe core above pH 5. In any case, a blueshift of the absorption spectrum due to progressive reduction of the QD size by acid etching can probably be observed only within a limited time frame before the QDs are complete dissolved.

Which PL changes are attributable to acid etching? In figure 6.3, it can be seen that the PL intensity is nearly completely quenched below pH 4 for DHLA-capped QDs and below pH 5 for micelle-encapsulated QDs. A strong blueshift can be observed for micelle-encapsulated QDs below pH 6. We believe that this blueshift is a signature of acid etching. For DHLA-capped QDs, figure 6.2 shows a progressive blueshift with time in the acidic pH regime, coincident with nearly complete quenching of the PL intensity. This plot shows that the average PL wavelength is comparable on day 0 and day 1, but on day 3 a strong blueshift appears. This indicates that DHLA-capped QDs may resist the acidic conditions for a limited time period.

Figure 6.4A shows that the PL intensity quenching for DHLA-capped QDs is irreversible. The PL spectrum is also permanently blueshifted upon exposure to acidic pH. Acid etching may be one of the causes for the irreversible component of these changes. Figure 6.4A also shows that the PL quenching for micelle-encapsulated QDs has a large reversible component. This suggests that

micelle-encapsulated QDs are less prone to acid etching than DHLA-capped QDs. This can be explained by differences in the organic coating. DHLA ligands form a thin (and possibly incomplete) monolayer around the QDs. Consequently, the QD surface is easily accessible to reactive species in the solution and irreversible damage by photo-oxidation or acid etching can quickly proceed at low pH. Micelle-encapsulated QDs, on the other hand, are better protected by a hydrophobic bilayer that surrounds the particles. The bilayer may serve as a barrier to the diffusion of oxygen and other hazardous species that would damage the QD surface [148].

6.3.2 pH-dependent surface passivation

As shown in figure 6.1, the PL intensity quenching is associated with a decrease of the PL lifetime, implying an increase in the non-radiative recombination rate. Non-radiative recombination events are associated with crystalline defects and charge carrier traps on the crystal surfaces [56]. Crystal surface traps are normally passivated by the binding of organic ligands. For instance, amines ($R\text{-}NH_2$) can passivate hole traps on CdSe crystal surfaces by sharing their free electron pair in a dative bond [56]. The surface passivation by organic ligands is however not static. It has been shown that part of the surface ligands is weakly/reversibly bound [101]. In apolar organic solvents, QDs are dispersed amidst a large excess of surface ligands, such that when surface ligands dissociate from the surface, they are quickly replaced by free ligands in the solution, thus maintaining a high PL quantum yield.

The situation is different in aqueous solvents and we have to discriminate between the different water-solubilization methods. Let us start with DHLA-capped QDs, which have lost their native ligands in favor of dithiols. We first review what is known about the pH-dependent stability of thiol-cappings. Aldana *et al.* showed that the pH-dependent precipitation of QDs capped with thiols (3-mercapto-1-propanol and 3-mercaptopropionic acid) is caused by the dissociation of the thiolate ligands in the pH range $3 - 7$ [105]. The thiolate ligands are removed from the surface by protonation in the acidic pH range. Interestingly, the dissociation pH was found to be dependent on the size and composition of the QDs. Moreover, the dissociation of ligands was found to be reversible and the QDs could be redispersed by increasing the pH to values larger than or comparable to the pK_a of the thiol group. Thiols typically have pK_a values around 11 (*e.g.* 3-mercaptopropionic acid and 2-mercaptoethanol have pK_a values of respectively 10.6 [149] and 9.5 [150]). Raising the pH above ~9.5 resulted in redispersion of the QDs for both 3-mercapto-1-propanol and 3-mercaptopropionic acid.

The above study shows that thiol-cappings lose their stability in the acidic pH range. Compared to monothiols, DHLA should coordinate more strongly to the surface by virtue of its two thiol groups. It is not clear if the coordination by two thiol groups will increase the pH-stability of the ligand (*i.e.* decrease

the dissociation pH). In our case, the thiols are bound to ZnS, while Aldana *et al.* investigated thiol-capped CdX (X = S, Se, Te) QDs. Based on their results, we estimate that the thiol-ZnS bond will remain stable down to pH values as low as 5 (the dissociation pH was found to decrease with increasing bandgap; the bandgap of ZnS is larger than the bandgap of CdS, which has a dissociation pH between 4 and 5 depending on the QD size). The pK_a value for both the thiol groups of DHLA is 10.7 [151], which is similar to the pK_a values for the monothiols studied by Aldana *et al.* This implies that the dissociation of DHLA ligands could be reversed at pH values similar to those for monothiols (pH > 9.5).

Another study examined how the PL of QDs is affected by the addition of thiols. Jeong *et al.* performed measurements on CdSe/ZnS QDs coated with octylamine-modified poly(acrylic acid) and studied the effect of adding 2-mercaptoethanol in different concentrations and under different pH conditions [92]. They showed that the deprotonated thiol (the thiolate anion, $R\text{-}S^-$) is detrimental to the PL quantum yield. Thiolates presumably passivate electron traps at low concentrations by their electron-donating ability, but they introduce new hole traps at high concentrations. While the study by Jeong *et al.* contains excellent complementary measurements, we feel that a separate study concerning the pH-dependency of the polymer-coated QDs in the absence of thiols is missing. The lack of such a study introduces some uncertainty about the origin of the PL changes (are they attributable to the binding of thiols, or to the binding of the amine and carboxylic acid groups of the polymer, or to both?).

Finally, we remind the reader of the study performed by Zhang *et al.* [108] (discussed in the introduction), in which they showed that carboxylic acid groups (and not carboxylates) interact with the semiconductor surface at low pH, thereby providing surface passivation and hence increase the PL intensity. Taken together, these studies suggest the following picture. Thiolates (and not thiols) coordinate to the QD surface and by doing so they affect the PL negatively (except at low concentrations). At low pH, the thiolate ligands can become protonated upon which they dissociate from the surface. Also, if carboxylic acids are present in the solution, they may interact with the QD surface and provide better surface passivation compared to thiols. Figure 6.2 shows that the PL intensity is quite stable above pH 6. We see no evidence of reversible binding of thiol groups at pH values close to the pK_a (10.7). If such binding events are indeed occurring, they have little effect on the PL intensity. Below pH 6, the PL intensity is quenched progressively with time (figure 6.2). As discussed in the previous section, acid etching is probably involved in this quenching. However, the pH-dependent dissociation of thiolate ligands may also play a role. The dissociation of DHLA ligands is supported by the redshift in the PL wavelength observed between pH 4 and 6, because the partial dissociation of thiol ligands could cause a redshift through the QCSE (see next section). Finally, note that there is no increase in PL intensity at low

pH that would suggest the interaction of carboxylic acids with the QD surface.

Micelle-encapsulated and PSMA-coated QDs present a very different situation. These water-soluble QDs are obtained by ligand addition. Ligand addition methods do not interfere with the native organic capping of the QDs, instead they build further on it. Unfortunately, this does not ensure an intact surface passivation after water-solubilization. The pre-phase transfer purification (see section 3.3) causes a substantial loss of predominantly weakly-bound (L-type) ligands (*e.g.* HDA, TOP, and TOPO). The degree of loss depends on the number of purification steps. We typically employed two purification steps. According to literature, QDs may still possess a small number of L-type ligands after only two purification steps [102, 103]. After the aqueous phase transfer, the number of remaining surface ligands in contact with the QD surface remains constant, because the ligands cannot escape the hydrophobic interior of the polymer shell or micelle (the native ligands are water-insoluble).

Based on the study of Aldana *et al.* concerning the pH-dependent and reversible dissociation of thiol ligands, it is reasonable to assume a similar picture for the native L-type ligands (in so far they are still present). Let us consider hexadecylamine (HDA). HDA can passivate the crystal surface in its deprotonated state (R-NH_2) through a dative bond. The amine group of HDA has a pK_a value of 10.6 [125], similar to the previously considered thiols. Below pH 10.6, the protonated state of HDA (R-NH_3^+) is favored. At pH values below 10.6, the dissociation of HDA is expected to cause a decrease in the PL intensity. Figure 6.3 shows a sharp decrease in the PL intensity of PSMA-coated and micelle-encapsulated QDs below pH 10. We hypothesize that this decrease may be due to pH-dependent depassivation of the crystal surface, possibly involving the dissociation of native (L-type) ligands.

Figure 6.4 shows that the pH-dependent PL changes for micelle-encapsulated QDs have both a reversible and an irreversible component. The previous mechanism, acid etching, clearly contributes only to the irreversible component. Based on the above discussion, we propose that the pH-dependent surface passivation contributes to the reversible component of the PL intensity changes.

6.3.3 The quantum-confined Stark effect

As discussed in chapter 5, the presence of an electric field will cause polarization of the excited electron-hole pair, thereby decreasing the wave function overlap as well as the exciton energy. As a consequence, the QCSE decreases the PL quantum yield and causes a spectral redshift of several nm. In the absence of external electric fields, local charges in the immediate vicinity of the QD can create electric fields sufficiently strong to induce the QCSE. There are several possible origins for local (pH-dependent) charges:

- Wang and co-workers measured the zeta potential of ZnS surfaces [152]. Their measurements showed that the ZnS surface charge is negative

and becomes smaller (more negative) as the pH increases. The surface charge depends also slightly on the stoichiometry of the ZnS surface, with sulphur-rich ZnS being more negative and zinc-rich ZnS being less negative than stoichiometric ZnS [152]. Consequently, the sulphuration reaction at acidic pH suggested by Durisic and co-workers could also change the surface charge in a permanent way [143].

- Local charges may be created when the passivation of the crystal surface by organic ligands is compromised. Firstly, the unpassivated surface atoms themselves may carry a slight positive or negative charge [153]. Secondly, dissociated organic ligands may be charged depending on the pH. For instance, ligands with an amine functional group will carry a positive charge at acidic pH values whereas ligands with a carboxylic acid group will carry a negative charge at basic pH values. In the case of micelle-encapsulated or polymer-coated QDs, dissociated native ligands remain in the hydrophobic interior of the organic coating, thus contributing to the local charge.
- Recently it was shown that QDs experience the QCSE when they possess an inhomogeneous, mixed organic capping layer [140]. While undergoing ligand exchange, QDs temporarily possess both amine and thiol ligands. The ligands can have different affinities for the different crystal facets [154]. Therefore it can be assumed that the competing ligand types are spatially separated on the QD surface, which would result in a pronounced internal electric field [140]. In our case, the pH-dependent dissociation of DHLA and native ligands could be more favorable at some crystal facets, leading to a partial thus inhomogeneous surface passivation. A mixed organic capping layer can also arise from the interaction of carboxylic acids with the QD surface. For instance, carboxylic acids react with the surface of thiol-capped CdTe QDs at low pH, thereby causing a spectral redshift [108]. Carboxylic acid groups can be present on ligands (*e.g.* DHLA, DSPE-PEG COOH), but also in the solution in the form of weak buffer acids such as acetate, citrate, *etc.* The interaction of COOH with the surface will depend on the pH and the pK_a value of the specific carboxylic acid. Lipoic acid for instance has a pK_a of 4.85 [151].

This list shows that there are several possible sources of pH-dependent local charges. The redshift observed for DHLA-capped QDs between pH 3 and 6 in figure 6.3 could be attributable to the QCSE. In this pH range, there is a steep decrease in PL intensity with decreasing pH. It seems reasonable to assume that this PL quenching is associated with deterioration of the semiconductor surface and its passivation, leading to an inhomogeneous charge distribution at the QD surface. For instance, the detachment of DHLA thiol groups and their potential replacement by carboxylic acid groups could lead to an inhomogeneous organic capping. Additionally, acid etching with preference for some crystal facets could occur.

PSMA-coated QDs also show a redshift with decreasing pH (figure 6.3). PSMA is a polymer with carboxylic acid groups, from which it is known that they can interact with the QD surface at low pH (in their protonated form) [108]. In the work of Zhang *et al.*, the surface interaction of carboxylic acids instead of thiols caused an increase in the PL intensity, which was ascribed to the better surface passivation by carboxylic acids [108]. The PSMA-coated QDs in figure 6.3 show a shoulder in the pH range where the redshift occurs. A possible explanation is that COOH-groups of PSMA bind to the QD surface in this pH range, thereby enhancing the PL intensity. At the same time, the binding of COOH-groups would create an inhomogeneous organic capping. The associated internal electric field could then cause a PL redshift through the QCSE.

For the micelle-encapsulated QDs in figure 6.3, a shoulder in the PL intensity can be observed between pH 5 and 7, but it is smaller than the shoulder for PSMA-coated QDs. It is also associated with a PL redshift. While some of the phospholipids that make up the micelles possess carboxylic acid groups, it is unlikely that these groups can interact with the surface, because they are attached to long hydrophilic PEG chains. The origin of the shoulder and the associated redshift requires further investigation. Possibly some buffering acids such as acetate enter the micelle and passivate the QD surface.

We attributed the reversible component of the PL intensity changes (figure 6.4) to the pH-dependent surface passivation. We propose that the reversible component of the spectral shifting is due to the QCSE. We suggest that these two mechanisms are interconnected: the pH-dependent depassivation of the surface causes electric fields that induce the QCSE. Notice that the QCSE should also affect the PL intensity (and not only the PL spectral position). In figure 6.4B, an increase in the pH is associated with an increase in the PL intensity on the one hand and a redshift (of about 3 nm) of the PL on the other hand. If the QCSE causes the spectral redshift, it should cause a simultaneous decrease in the PL intensity. From figure 5.2, we observe that for a 3-nm redshift, the PL intensity decrease due to the QCSE is only 16%. In the reversibility experiment, the small decrease in PL intensity due to the QCSE is probably bested by the increase in PL intensity due to repassivation of the QD surface, which results in a net increase in PL intensity.

6.4 Influence of the QD structure and composition

The literature overview (table 6.1) shows that the QD composition (*i.e.* the semiconductor material) influences the pH-dependency of the PL properties. We will compare the pH-dependent PL properties of three commercial nanocrystals: CdSe/ZnS QDs (Lumidot™ 640), CdSe/ZnS QDs from another supplier (Ocean Nanotech QSP-630), and CdSe/CdS QRs (CANdots® Series A+).

The main difference between these three semiconductor nanocrystals is the shell composition (and thickness). Therefore, the comparison between these nanocrystals will demonstrate the influence of the shell in the pH-dependency. We compare below the differences between the pH-dependency of the nanocrystals for each organic coating separately.

6.4.1 Micelle-encapsulated semiconductor nanocrystals

Figure 6.5 shows that the PL intensity is quenched at low pH for all three micelle-encapsulated nanocrystals. The quenching is strongest for Lumidot™ QDs. It starts at higher pH values and is almost complete below pH 5. In contrast, the PL intensity of QSP-630 QDs and CANdot® QRs is quite stable above pH 5.5. While the PL intensity profiles of the QSP-630 QDs and the QRs resemble each other, their average PL wavelength profiles are quite different. For QSP-630 QDs, there is a blueshift with decreasing pH between pH 10 and 3. For QRs, the average PL wavelength is nearly constant over the pH range $3 - 10$. In both cases, the spectral shifts are smaller than those for Lumidot™ QDs.

The QSP-630 QDs show much better resistance to low pH than Lumidots™, although the nanocrystal composition is identical. The PL intensity quenching is less profound and starts at lower pH values. Also, the spectral blueshift attributed to acid etching as is observed for Lumidots™ is missing for QSP-630 QDs. This indicates that the latter QDs maintain better their integrity, possibly because of a thicker ZnS shell. Indeed, QSP-630 QDs have a substantially larger diameter than Lumidot™ QDs, despite the fact that both QDs emit PL at nearly the same wavelength. TEM measurements found a diameter of 5.7 ± 0.2 nm for Lumidot™ QDs versus 7.6 ± 0.2 nm for QSP-630 QDs (section 4.3). The size difference is likely due to differences in the thickness of the ZnS shell, being thicker for QSP-630 QDs. The QSP-630 QDs also retain their PL brightness better than Lumidots™ during the purification step to remove excess ligands QDs (section 3.3), although both QDs have similar ligands (hexadecylamine for Lumidots™ versus octadecylamine for QSP-630 QDs). So while for both QDs the surface passivation is impaired at low pH due to dissociation of ligands, we believe that the thicker ZnS shell of QSP-630 QDs provides better isolation for the exciton from surface traps.

The almost constant average PL wavelength in the case of CANdot® QRs implies the absence of the QCSE, or in other words, the QRs experience no strong local electric fields. The different composition (CdSe/CdS) or the different organic ligands (phosphonic acids) might be responsible for this.

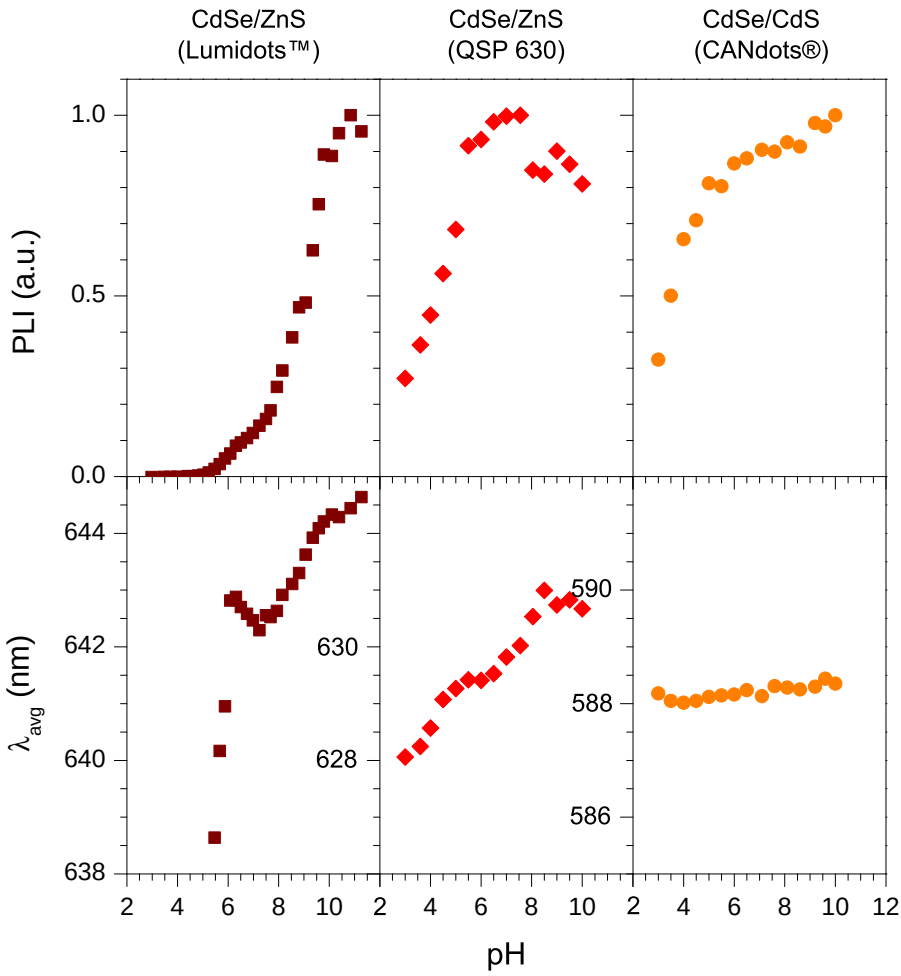

Figure 6.5 – The pH-dependency of micelle-encapsulated Lumidots™, Ocean Nanotech QSP 630, and CANdots® Series A+ 590. The PL intensity (PLI) and average PL wavelength (λ_{avg}) are plotted as a function of the pH. Experimental details: semiconductor nanocrystals were dispersed in Britton-Robinson buffer (0.04 M for QDs, 0.01 M for QRs).

6.4.2 PSMA-coated semiconductor nanocrystals

A remarkable difference exists between Lumidot™ QDs and QSP-630 QDs coated with PSMA (figure 6.6). Lumidots™ show a decreasing PL intensity with decreasing pH. QSP-630 QDs on the other hand show the opposite trend. Their PL intensity increases rapidly with decreasing pH between pH 6 and 9. The PL intensity then obtains a maximum at pH 5.5, after which it declines with decreasing pH. The inverse trend is surprising because micelle-encapsulated QSP-630 QDs, which have the same surface passivation, show the usual trend (figure 6.5). Figure 6.6 also shows a strong blueshift for QSP-630 QDs as the pH decreases from 9 to 6, a feature that is absent in the case of micelle-encapsulated QSP-630 QDs.

The explanation for this unusual pH-dependency should be found in the organic coating. We have proposed before that carboxylic acid groups may interact with the QD surface and provide surface passivation, thereby increasing the PL intensity. In PSMA-coated QDs, the maleic anhydride units of the polymer provide carboxylic acid groups. The maleic anhydride groups are reacted with ethanolamine during the aqueous phase transfer (see section 3.6). This ring opening process results in the formation of an amide bond and a terminal carboxylate [155]. The amide bond is only stable at neutral pH and above. At acidic pH, the amide bond is hydrolysed and the amine is released (deacylation of the amine), leaving behind two carboxylic acid groups. Alkyl-derivatives of maleic acid (*e.g.* citraconic anhydride) are even more reversible towards deacylation. Consequently, it can be expected that PSMA loses the ethanolamine at acidic pH. The pH will also determine the protonation of the carboxyl groups. A recent study reported pK_a values for poly(styrene-co-maleic acid) of 5.27 and 10.49 for the first and second acid dissociation step respectively [156], while an older work found pK_a values of 4.4 and 10.3 [157]. Notice that these pKa values are substantially higher than the pK_a values for maleic acid (1.92 and 6.23) [125]. Thus, in the acidic pH regime, both carboxylic acid groups are protonated. However, in the neutral and alkaline pH regime, PSMA is functionalized with ethanolamine and contains only one carboxylate group of which we don't know the pK_a value. This makes it hard to predict the possible interactions in the neutral and alkaline pH range.

In any case, the interaction of carboxylic acid groups could explain the increase in the PL intensity upon decreasing the pH towards the pK_a value of the carboxylic acid groups. However, why is the interaction with COOH increasing the PL intensity only in the case of QSP-630 QDs and not for Lumidots™? We believe that the differences between the Lumidots™ and QSP-630 QDs are caused by the differences in the ZnS shell thickness. In the case of Lumidots™, the thin (possibly incomplete) ZnS shell offers insufficient protection from surface traps that are created when the pH is decreased and the PL is quenched. The surface passivation by carboxylic acids, possibly detected as the pronounced spectral shift between pH 4 and 6, slightly retards the pH quench-

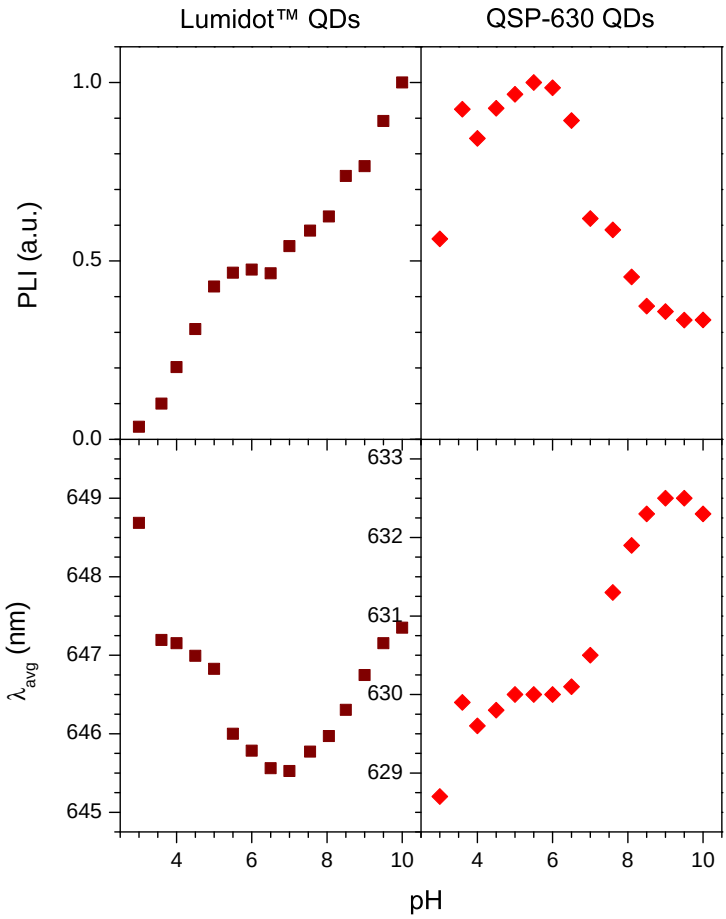

Figure 6.6 – The pH-dependency of the PL for PSMA-coated Lumidots™ and Ocean Nanotech QSP-630 QDs . The PL intensity (PLI) and average PL wavelength (λ_{avg}) are plotted as a function of the pH. Experimental details: QDs were dispersed in Britton-Robinson buffer (0.04 M).

ing, which is visible as a shoulder in an otherwise monotonous decrease. For QSP-630 QDs, the thick ZnS shell is not breached when the pH is decreased and the exciton remains mostly isolated from interaction with surface traps. Instead, the pH decrease reinforces the surface passivation by allowing carboxylic acids groups to bind to the QD surface, and the PL intensity increases.

6.4.3 DHLA-capped semiconductor nanocrystals

Finally, we compare DHLA-capped Lumidots™ and CANdot® QRs (figure 6.7). We discussed the pH-dependency of DHLA-capped Lumidots earlier in this chapter. We attributed the PL quenching at low pH to an acid etching mechanism, potentially in combination with dissociation of the thiolate ligands. The PL redshift between pH 4 and 6 is likely a manifestation of the QCSE, caused by dissociation of thiols ligands and/or binding of carboxylic acids. CANdot® QRs show the opposite pH-dependency: the PL intensity increases with decreasing pH. The PL is also blueshifted, but in contrast to Lumidots™ there is no redshift between pH 4 and 6. However, the measurement point at pH 3 is redshifted by ~1.6 nm compared to pH 3.5. Is this the start of a similar redshift feature as seen for Lumidots™, but shifted to lower pH values?

There are several reasons that may explain the different pH-dependency of CdSe/CdS QRs compared to CdSe/ZnS (Lumidot™) QDs . Firstly, the shell is composed of another semiconductor material. Thiol cappings are more stable (lower dissociation pH) on CdS surfaces than on CdSe surfaces [105]. The redshift at pH 3 might be an indication that the DHLA capping becomes unstable at this pH. A new measurement with an extended pH range would be necessary to draw this conclusion. Secondly, CdSe/CdS QDs are so-called type-II QDs, with the hole confined to the CdSe core while the electron can be either localized at the core or at the shell [158]. This implies that the electron has a larger chance to interact with surface traps on the CdS surface. However, because thiolates passivate electron traps [92] this likely does not affect the PL quantum yield negatively. Thirdly, the different pH behavior may be caused by differences in the thickness or quality of the inorganic shell. Finally, there is obviously the shape difference, dots versus rods, yet we do not believe that the shape can cause an inversion of the pH-dependency.

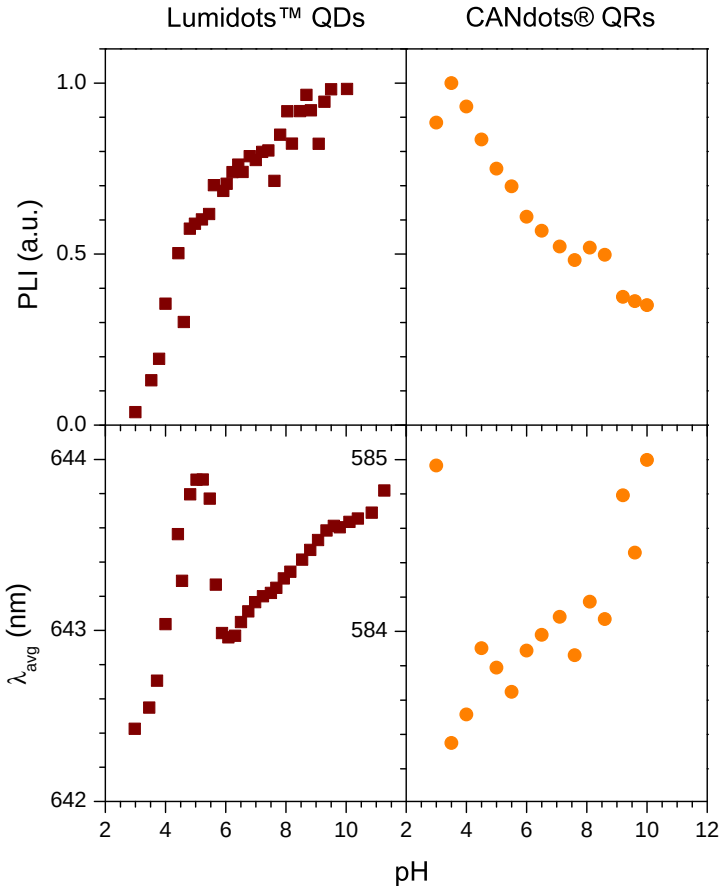

Figure 6.7 – The pH-dependency of the PL for DHLA-capped Lumidot™ QDs and CANdot® QRs. The PL intensity (PLI) and average PL wavelength (λ_{avg}) are plotted as a function of the pH. Experimental details: semiconductor nanocrystals were dispersed in Britton-Robinson buffer (0.04 M for QDs, 0.01 M for QRs).

6.5 Conclusions

A review of the available literature shows that the pH-dependency is different for QDs composed of different materials. For instance, the PL intensity of CdSe/ZnS QDs is generally quenched at low pH, whereas the PL intensity of CdTe QDs is increased at low pH. However, different observations have been made even for the same type of QD, for instance in terms of spectral shifts and reversibility of the quenching. To clarify these different observations, we investigated the pH-dependent PL for three QD types and for three types of organic coating.

We first studied the pH-dependency for micelle-encapsulated CdSe/ZnS QDs and made the following observations. Firstly, lowering of the pH value causes a decrease in both the PL intensity and the PL lifetime, which suggests a reduction of the PL quantum yield. Secondly, we found that the pH-induced changes of the PL are time-dependent and that they may take several hours to days. Thirdly, there are small differences between the pH-dependencies of DHLA-capped, PSMA-coated, and micelle-encapsulated CdSe/ZnS QDs. We found that the PL intensity changes coincide with spectral shifts of the PL, suggesting a common underlying mechanism. Finally, we observed that the pH-dependent PL changes have a reversible and an irreversible component. The organic coating determines which component is dominant. For instance, DHLA-capped QDs have a small reversible component that is observable only on short time scales, while micelle-encapsulated QDs show strong reversibility even on long time scales.

Based on our observations regarding the pH quenching, reversibility, and spectral shifting, we proposed that three mechanisms are involved in the pH-induced PL changes, namely acid etching, pH-dependent surface passivation, and the quantum-confined Stark effect (QCSE). Acid etching causes irreversible quenching at low pH values. The etching process is progressive with time and may ultimately cause complete quenching of the PL. A thick organic capping may protect QDs better against acid etching. pH-dependent surface passivation involves the reversible binding of organic ligands such as thiols and amines. The dissociation of ligands with decreasing pH leads to the creation of surface traps and therefore to quenching of the PL intensity. This process may explain the reversible component in the pH-dependent changes. The QCSE can originate from the electric fields caused by local charges and/or inhomogeneous organic cappings, both of which can be pH-dependent. The QCSE causes changes in the PL intensity as well as spectral shifting. Together, these three mechanisms can explain the reversible and irreversible PL intensity and spectral changes.

In the last part of this chapter, we investigated the influence of the QD material composition on the pH-dependency of the PL. For micelle-encapsulated QDs, we found that QSP-630 CdSe/ZnS QDs are more resistant to PL quenching at low pH than Lumidot™ QDs. Because these two QDs are composed of the same material and have similar organic cappings, this indicates the in-

volvement of other factors such as the shell (epitaxial) quality and thickness. The PL wavelength of CdSe/CdS QRs was nearly constant over the measured pH range, whereas the CdSe/ZnS QDs showed notable pH-dependent spectral shifting. This may be due to the different shell material or due to the differences in the native organic capping. A remarkable difference was found for QDs coated with PSMA. With decreasing pH, Lumidot™ QDs showed a decreasing PL intensity, whereas QSP-630 QDs showed an increasing PL intensity. The differences in shell quality/thickness may be responsible for the opposite behavior. An opposite behavior was also found for DHLA-capped Lumidot™ CdSe/ZnS QDs and CdSe/CdS QRs. The reason for this difference in behavior requires further investigation.

Chapter 7

Bioconjugation of quantum dots with glucose oxidase

In this chapter we discuss the bioconjugation of colloidal micelle-encapsulated QDs with *glucose oxidase* (GOX). The resulting hybrid particles are interesting because the small separation between GOX and QDs is expected to enhance the interaction between the two. This will be the topic of chapter 8. This chapter is structured as follows. Section 7.1 gives a literature overview of bioconjugation strategies that have used to couple QDs and proteins. In the next sections, we present our results obtained with three different bioconjugation strategies. In section 7.2, we discuss the bioconjugation of COOH-functionalized QDs using covalent crosslinking with EDC-NHS. In section 7.3, we discuss the bioconjugation of amine-functionalized QDs using electrostatic binding. In section 7.4 finally, we show how electrostatic binding and covalent crosslinking can be combined for the bioconjugation of amine-functionalized QDs with GOX.

7.1 Introduction

Several strategies have been employed to bioconjugate nanoparticles with proteins. The two most common approaches are based on covalent cross-linking [159, 22, 23, 160] and electrostatic binding [24, 25, 161]. Other techniques include biotin-avidin affinity binding [161], metal-histidine coordination [162, 17], and the denaturation of proteins to liberate the thiol groups which have strong affinity for the semiconductor surface [107, 163]. Below, we discuss some notable studies for each approach.

Electrostatic binding. Gerhards *et al.* employed electrostatic interactions to conjugate positively charged *cytochrome c* to negatively charged QDs [25]. Mattoussi *et al.* reported on the biofunctionalization of DHLA-capped CdSe/ZnS QDs with proteins [24]. Their initial attempts to covalently at-

tach proteins (immunoglobulin G or ovalbumin) to such QDs using EDC were relatively unsuccessful and resulted in the aggregation of the QD-protein conjugates. Therefore, they developed an alternative technique based on self-assembly, using the electrostatic interactions between (negatively charged) QDs and engineered recombinant proteins consisting of positively charged attachment domains genetically fused with desired biologically relevant domains.

Covalent crosslinking. Covalent crosslinking is mostly achieved by using carbodiimide crosslinker chemistry based on the compounds EDC and (sulfo-)NHS. Song *et al.* investigated in detail the bioconjugation of polymer-coated QDs with different proteins using carbodiimide chemistry [22]. They found that the concentration of EDC plays a critical role: too low concentrations result in a large percentage of unconjugated QDs, while too high concentrations lead to significant aggregation. In the concentration range between those two extremes, changing the concentration could be used to tune the number of proteins (from one to several) per QD. Their results also showed that the conjugation protocol has to be optimized separately for each protein. Finally, they showed that the number of bound proteins per QD can influence the PL quantum yield as well as the binding avidity (in case of immunoglobulin G). Wang *et al.* also investigated the bioconjugation of QDs using EDC/NHS chemistry [23]. They studied the effects on the bioconjugation of certain factors such as the isoelectric point (pI) of the biomacromolecules and the buffer pH. They observed that the conjugation efficiency of proteins increased with increasing pI. Secondly, the conjugation efficiency was generally improved when the buffer pH was lowered (in the pH range $6 - 8$). They also studied the kinetics of the conjugation process for one protein by fluorescence correlation spectroscopy and found that the characteristic diffusion time remained quasi-constant after 10 minutes, implying that the conjugation reaction is rapid and occurs on a timescale of minutes.

Other approaches. Goldman *et al.* exploited the affinity of avidin for biotin to bioconjugate CdSe/ZnS QDs [161]. Avidin, a highly positively charged protein, absorbed tightly to negatively charged DHLA-capped QDs (electrostatic self-assembly). Through the avidin bridge, the conjugation to biotinylated antibodies subsequently was readily achieved. Medintz *et al.* conjugated DHLA-capped CdSe/ZnS QDs with a variant of maltose binding protein expressed with a pentahistidine segment at its C-terminus [17]. The modified maltose binding protein spontaneously assembled onto the QDs through metal-histidine coordination. The authors surmised that the oligohistidine-metal coordination occurred at discontinuities or defects in the DHLA-capping. Interestingly, the coordination led to an enhancement of the PL. Gao *et al.* coated CdSe/ZnS QDs with denatured bovine serum albumin (BSA) [107]. Denatured BSA (dBSA) contains 37 thiol groups and was prepared by chemically reducing BSA, converting the disulfide bonds of the protein into thiol groups. The QDs, originally coated with MAA, were incubated in dBSA solution for several days, resulting in the exchange of MAA with BSA.

Wang *et al.* coated MAA-capped CdTe QDs with dBSA [163]. They showed that only dBSA monomers and dimers, and not oligomers, conjugated to their QDs. The PL properties of the dBSA-coated QDs were highly dependent on the dBSA-QD ratio, with too high are too low ratios resulting in a decrease of the PL quantum yield. The PL was also spectrally blueshifted (except for the lowest dBSA-QD ratio, which showed a small redshift). The blueshift became stronger with increasing storage time, and was attributed to the formation of a complex CdTeS shell around the core, reducing the core size.

7.2 Covalent binding using EDC-NHS

The carbodiimide 1-Ethyl-3-(3-dimethyl-aminopropyl)carbodiimide (EDC) is a zero-length crosslinker that is used to mediate the formation of amide linkages between carboxylates and amines. Zero-length crosslinkers achieve crosslinking without the introduction of additional spacer arm atoms between the two conjugated molecules. The application of EDC in particle and surface conjugation procedures along with NHS (N -hydroxysulfosuccinimide) or sulfo-NHS is nearly universal, making it the most common bioconjugation reagent in use today [164]. Typically, the reaction proceeds as follows. The carboxylic acid is first activated by EDC to form an O-acylisourea active intermediate. This intermediate is then displaced by a primary amine that forms an amide bond with the original carboxylic acid. The O-acylisourea intermediate is however highly unstable in aqueous solutions in which it quickly hydrolyses. In the presence of sulfo-NHS, the O-acylisourea intermediate reacts with the hydroxyl group of sulfo-NHS to form a more stable sulfo-NHS ester intermediate. The primary amine then reacts with this sulfo-NHS ester to form an amide bond. Using this two-step reaction, the efficiency of amide bond formation is greatly enhanced, while the final product of the two-step reaction is identical to the one obtained using EDC alone [164]. Finally, the hydrolysis rate of the sulfo-NHS esters is dramatically slower at slightly acidic pH. Therefore it is worthwhile to use to two different buffer solutions. The first buffer solution at slightly acidic pH (pH 6.0) for the activation step and the second buffer solution (pH 7-8) for the conjugation step. Below we describe the protocol that was used to bind GOX onto COOH-functionalized QDs.

Micelle-encapsulated QDs can be equipped with carboxyl groups by using COOH-functionalized phospholipids during encapsulation. In this work, we used a mixture of 10% DSPE-PEG COOH phospholipids and 90% DSPE-mPEG phospholipids. The idea is to crosslink the carboxylate groups of the QDs with primary amines on the surface of GOX by means of EDC-NHS. The experimental procedure is described in protocol 7.1. In summary, we activated the carboxyl groups of the QDs at slightly acidic pH by the addition of EDC and sulfo-NHS. We then used a desalting column to remove unreacted reagents and by-products and to exchange the buffer solution. After the column step,

Required chemicals: water-soluble QDs with COOH functional groups (1 nmol), GOX (16 mg), EDC, sulfo-NHS, PBS buffer (0.1 M phosphate, 0.15 M NaCl, pH $7.2-7.5$), MES buffer (0.1 M MES, 0.5 M NaCl, pH 6.5).

Step-by-step description:

- The amount of GOX is based on the molar concentration of QDs. In this protocol, we take a GOX concentration equal to 100 times the QD concentration. This gives a target 100 nmol (16 mg) of GOX .
- Dissolve the GOX in 1 ml PBS buffer and the QDs in 0.5 ml MES buffer.
- Determine approximately the number of COOH groups to be activated. During the water-solubilization procedure, we used 5 mg phospholipids of which 10% was functionalized with COOH groups. This gives an upper limit of 0.5 mg/2850 g/mol $\approx$ 0.18 µmol COOH groups. Use 10 times this amount of EDC (1.8 µmol EDC) and 25 times this amount of NHS (4.5 µmol or 1 mg).
- Prepare the desalting column: equilibrate the column with PBS buffer.
- Mix the QDs with the EDC and NHS and react for 15 minutes at room temperature.
- Send the sample through the desalting column to remove EDC by-products and/or unreacted EDC. Collect the elute as separate fractions.
- Determine the fraction containing the QDs. Dilute this fraction to 1 ml (if necessary). Mix this fraction with the GOX solution and react for two hours while shaking.
- Concentrate the sample ultracentrifugation through a semi-permeable membrane device (*e.g.* Nanosep® 10K Omega™) or by reverse dialysis. Use gel filtration chromatography to remove the excess (unbound) GOX.

Protocol 7.1 – Bioconjugation using the EDC-NHS crosslinking reaction.

the GOX solution is added and the conjugation reaction is allowed to take place. In this procedure, we use a large excess of GOX compared to QDs for two reasons. Firstly, we want to saturate the QD surfaces with enzymes. secondly, we want to prevent the binding of multiple QDs to one enzyme. For this reason, we also add the QD solution dropwise to the GOX solution, instead of the other way around. Using such a large excess of GOX means that the sample will contain an excess of free enzymes after the crosslinking reaction. To separate the GOX-functionalized QDs from the excess free GOX, we performed gel filtration chromatography (GFC) on our samples.

Figure 7.1 shows the UV-visible absorption versus time of the gel filtration eluent for three samples: the sample containing the (supposedly) bioconjugated QDs (QDs + GOX) and two controls (only GOX and only QDs). Five wavelengths characteristic of either the GOX enzyme or the QDs were monitored: 374 nm and 450 nm correspond to the local maxima in the absorption spectrum of GOX, 325 nm corresponds to a local minimum in the absorption of GOX, and 615 nm corresponds to the first absorption maximum of the QD spectrum. The measurement at 700 nm finally serves as a reference baseline, because neither GOX nor QDs absorb light at this wavelength. The top panel of figure 7.1 shows the GFC profile of a sample containing only GOX. The maximum absorption is reached at 23 min after injection of the sample. The bottom panel shows GFC on a sample containing only QDs. The maximum absorption is detected at 13 min. As expected, this is well before the elution of GOX. The middle panel shows GFC on the sample containing the bioconjugated QDs. Two peaks can be discriminated: the first peak at 13 min corresponds to (bioconjugated) QDs; the second peak at 22 min corresponds to unbound GOX. Bioconjugated QDs should be larger in size than unconjugated QDs. Therefore, it is expected that the bioconjugated QDs reach their maximum absorption before 23 min. However there is no significant difference in the elution time between the unconjugated and bioconjugated QDs.

The elution profiles (figure 7.1) do not indicate an increase in particle size after applying protocol 7.1, suggesting that the bioconjugation may not have been successful. Further characterization of the GFC fractions by other techniques is necessary to confirm if the bioconjugation was unsuccessful. Figure 7.2 shows measurements of the UV-visible absorption, photoluminescence intensity, and hydrodynamic size for the fractions of the sample "QDs + GOX". Because GOX is not fluorescent, the PL measurements confirm that the first peak is attributable to QDs (figure 7.2A). The PL measurements show that the tail of the QD peak protrudes into the GOX peak, indicating that the separation by GFC is incomplete. Note that, while both the PL and the absorption at 615 nm are solely due to the presence of QDs, the PL signal is much more sensitive than the absorption at this wavelength.

Figure 7.2B shows the UV-visible absorption spectra of some representative fractions. Fractions 3, 5, and 7 fall within the first peak (corresponding to QDs), whereas fractions 12 and 16 fall within the second peak (corresponding

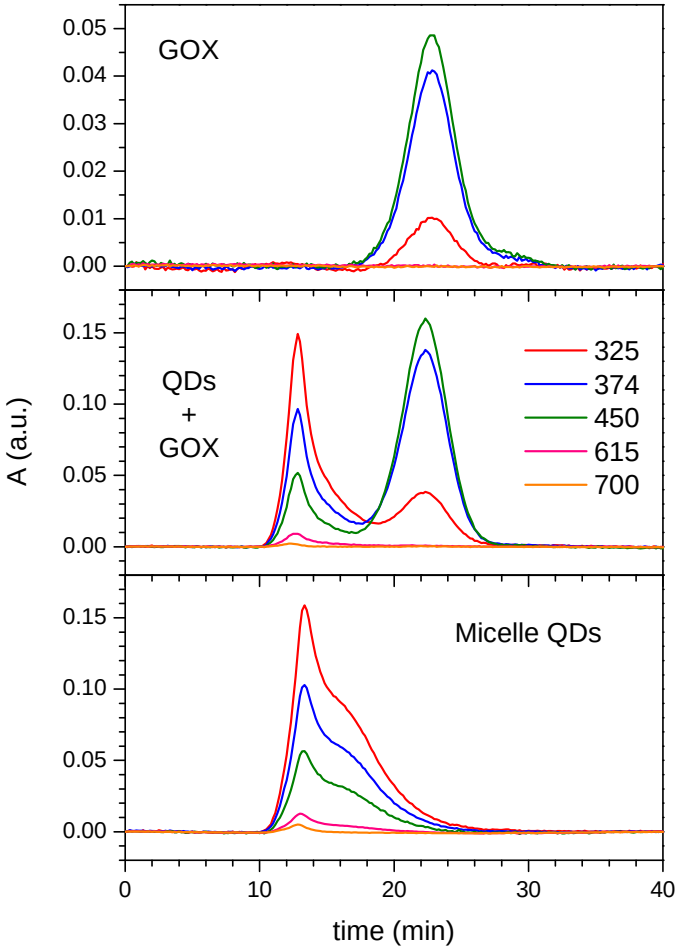

Figure 7.1 – Gel filtration chromatography of three different samples: *glucose oxidase* only (GOX), bioconjugated micelle-encapsulated QDs (QDs+GOX), and micelle-encapsulated QDs only (QDs). The UV/visible absorption of the elute versus time is shown at five different wavelengths (325, 374, 450, 615, and 700 nm). The sample was injected at 0 min.

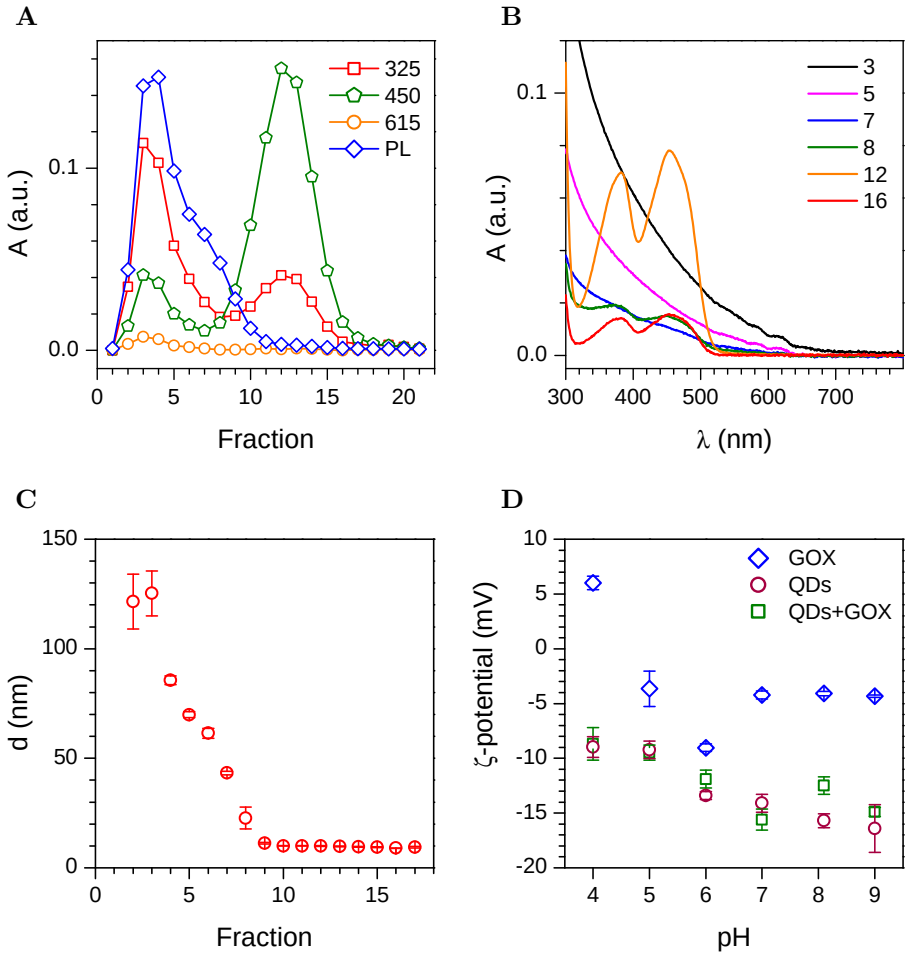

Figure 7.2 – Study of the separate GFC fractions. **(A)** The UV/visible absorption (at 325, 450, and 615 nm) and PL intensity (sum over the range 540-730 nm) for the fractions of the sample QDs+GOX. **(B)** UV/visible absorption spectra for some selected fractions of the sample QDs+GOX. **(C)** Average hydrodynamic particle diameter for fractions $2-17$ of the sample QDs+GOX. **(D)** pH-dependence of the ς-potential for the samples GOX, QDs, and QDs+GOX. Measurements were done on representative fractions for each sample. Experimental details: QDs in the separate fractions are dissolved in borate buffer (0.02 M boric acid, 0.1 M NaCl, pH 8.5) (panels A-C). For the ζ-potential measurement (panel D), some representative fractions were selected and the pH of these samples was adjusted by means of dialysis against a series of Britton-Robinson buffers of constant ionic strength over the pH range $4-9$ (see appendix A for preparation of this buffer series).

to GOX). Fraction number 8 is situated in between the two peaks. The spectra of fractions 3, 5 and 7 show the characteristic shape of the QD spectrum, but there is no trace of the GOX spectrum. Fractions 12 and 16 show the typical absorption spectrum of GOX, with local maxima at 380 nm and 455 nm. Fraction 8 finally, contains features of both the QD and the GOX spectrum.

Figure 7.2C shows the hydrodynamic diameter of the particles obtained by DLS for the first 17 fractions. As expected, the average particle size decreases with increasing fraction number. For fractions 2 to 7, particle sizes larger than 40 nm are found, indicating the presence of aggregates. From fraction 9 onwards, the diameter amounts to approximately 10 nm, which corresponds to the hydrodynamic size of GOX. One can expect that a successful biofunctionalization of QDs with GOX would increase the hydrodynamic size. In principle, this size increase could be deduced by comparing the hydrodynamic size before (figure 3.8) and after biofunctionalization (figure 7.2C). The problem is that our samples are too polydisperse: there is no unique particle size before or after the biofunctionalization. Therefore, it is difficult to draw any conclusions on the success of the biofunctionalization based on these DLS size measurements.

We remind the reader that DLS size measurements are heavily biased towards the larger particles. Even a small amount of aggregates ($\sim 0.001\%$) may lead to a pronounced second peak at higher sizes [162]. The presence of a larger percentage of aggregates likely obscures the peak at low sizes and increases the measured hydrodynamic diameter. The origin of the size polydispersity observed in figure 7.2C is likely two-fold. Firstly, we performed the bioconjugation on a batch of QDs that was not size-selected by GFC. Figure 3.8 shows that already the unconjugated micelle-encapsulated QDs are polydisperse. Secondly, the bioconjugation procedure may further increase the polydispersity by creating QD-GOX assemblies of different sizes. The reason why we did not size-select our QDs before bioconjugation is that during the size-separation by GFC, a substantial amount of QDs is retained within the column matrix. Furthermore, by selecting only one fraction (or a few subsequent fractions), the amount of QDs to work with is further reduced. Consequently, the amount of bioconjugated QDs would have been too small to perform a second GFC step (to remove the excess GOX).

Before their biofunctionalization, the micelle-encapsulated QDs are expected to be negatively charged, due to the phosphate and carboxyl groups on the PEG phospholipids. GOX should be negatively charged at pH values larger than the isoelectric point (pI) of 4.2. Figure 7.2D shows the ς-potential of GOX, QDs, and QDs+GOX. For unconjugated QDs, the ς-potential is negative in the pH range $4 - 9$. For GOX, the ς-potential is positive at pH 4, but negative from pH 5 onwards, in accordance with the pI of 4.2. The pH-dependence of the ς-potential is thus different for GOX and QDs. The ς-potential for QDs+GOX coincides with that of the bare QDs, showing no resemblance to the profile of GOX. This suggests again that GOX is not bound to the QDs. In summary, our experimental results give no indication that the

Required chemicals: positively charged micelle-encapsulated QDs (1 nmol), GOX (16 mg), PBS buffer (0.01 M phosphate, pH 7.0).

Step-by-step description:

- Dissolve the QDs in 1 ml PBS buffer.
- Taking a 100-times excess of GOX compared to QDs requires 16 mg GOX. Dissolve the GOX in 1 ml PBS buffer.
- Slowly add the QD solution to the GOX solution while vortexing.
- Concentrate the sample by ultrafiltration over a semipermeable membrane (*e.g.* Vivaspin™ sample concentrator with MWCO 10,000: spin at 2000 g for 30 min) or by reverse dialysis.
- Perform gel filtration chromatography to remove the excess GOX.

Protocol 7.2 – Bioconjugation using electrostatic attraction.

biofunctionalization of QDs with GOX was successful. We believe the main obstacle preventing successful bioconjugation with this protocol is the electrostatic repulsion between QDs and GOX, which are both negatively charged. Gerhards *et al.* found that *cytochrome c*, which is positively charged at neutral pH (pI = 10.6 [165]), could be conjugated to negatively, but not to positively charged QDs [25]. Therefore, we changed our strategy as described in the next section and used positively charged QDs to facilitate the binding.

7.3 Electrostatic adsorption

GOX is negatively charged at pH values larger than its pI of 4.2. It is therefore expected that GOX can bind electrostatically to positively charged QDs at those pH values. Positively charged QDs can be obtained by using organic ligands with positively charged functional groups, such as amines. For instance, to obtain positively charged micelle-encapsulated QDs, phospholipids with amine groups instead of carboxylic acid groups can be used. Initially, we used a mixture of 10% DSPE-PEG amine phospholipids and 90% DSPE-mPEG phospholipids. However these QDs still had a negative ς-potential, namely -3.6 ± 0.1 at pH 5.0, probably because of the negatively charged phosphate groups (figure 3.5). Micelle-encapsulated QDs having micelles exclusively composed of DSPE-PEG amine have a positive ς-potential, namely $+7.5 \pm 0.4$ at pH 5.0.

The biofunctionalization of these QDs with GOX is described in detail in protocol 7.2. Briefly, QDs were first diluted and then mixed with a large excess of GOX. The large excess of GOX and low concentration of QDs serves to prevent the formation of aggregates or the binding of multiple QDs to one GOX

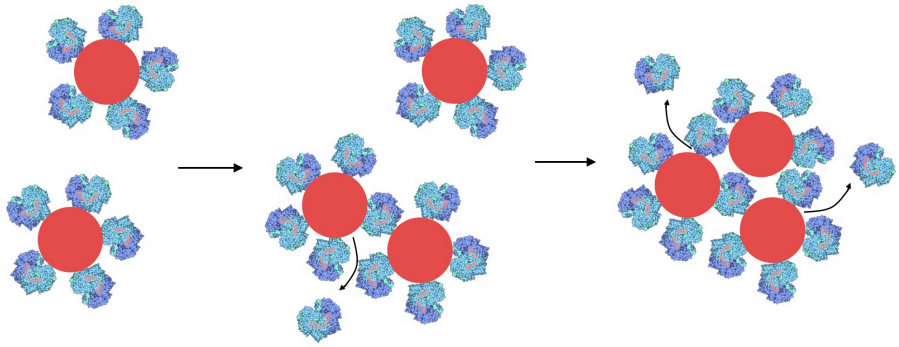

Figure 7.3 – Electrostatic assemblies of QDs and GOX are unstable and form larger aggregates.

enzyme. While the dispersion consisting of mixed QDs and GOX appeared stable and transparent at first sight, we noticed red precipitate after some hours, indicating aggregation of the GOX-functionalized QDs. The aggregates could not be resuspended by shaking or even ultrasonication. This implies that the electrostatic QD-GOX assemblies have limited stability as single particles. GOX-functionalized QDs possibly merge together by displacing one or more GOX molecules, resulting in QDs being bridged by one or more GOX enzymes (figure 7.3). In summary, we were able to interact GOX and positively charged QDs, but they we unstable over time.

7.4 Electrostatic *and* covalent binding

The formation of covalent bonds between the GOX molecules and the QDs to which they have absorbed may increase the stability of the electrostatic assemblies as single particles. The protocol of the last section can be modified to include covalent binding between the QDs and GOX. Because the QDs possess only amine functional groups, it are the carboxylate groups of GOX that have to be activated with EDC-NHS. However, GOX also contain primary amines, therefore care must be taken to prevent crosslinking between GOX enzymes during the activation step. One way to do this is by diluting the solution, which causes the intermolecular distance to increase. The experimental procedure is described in protocol 7.3. With this modified protocol, precipitate could still be observed over time, but it was easily resuspended upon shaking. This indicates that the individual QD-GOX assemblies are more stable.

GFC was used to separate GOX-functionalized QDs from unbound GOX. The monitoring of the elute by UV/visible spectroscopy is shown in figure 7.4. Two peaks corresponding to QDs and GOX can be discerned, but the absorbance values are low and the peaks are not well resolved as in figure 7.1. The

Required chemicals: positively charged micelle-encapsulated QDs (1 nmol), GOX (4 mg), EDC, sulfo-NHS, PBS buffer (0.01 M phosphate, pH 7.0).

Step-by-step description:

- Dissolve 4 mg GOX (25 nmol) in 20 ml PBS buffer. This gives a molar concentration of 1.25 µM. Add the following quantities of EDC ($20 \times 25 = 250$ nmol) and NHS ($50 \times 25 = 1.25$ µmol) to the GOX solution. Shake gently for 15 min.
- Dissolve the QDs (1 nmol) in 1 ml PBS buffer. Add dropwise to the GOX solution and shake overnight.
- Concentrate the sample by ultrafiltration over a semipermeable membrane (*e.g.* Vivaspin™ sample concentrator (MWCO 10,000), spin at 2000 g for 30 min) or by reverse dialysis. Redisperse any precipitated QDs.
- Remove the excess GOX by gel filtration chromatography.

Protocol 7.3 – Bioconjugation based on electrostatic and covalent binding.

absorbance at 325 nm is largest in the first peak, indicating that these are QDs. In the second peak, the absorbances at 374 nm and 450 nm are largest, corresponding to the presence of GOX. We also performed GFC on the unconjugated QDs as a control. However, we found that the unconjugated QDs were completely retained in the column matrix. Possibly, the positively charged QDs interact more strongly with the gel matrix or the gel matrix was contaminated with (negatively charged) QDs or enzymes from previous passages. As a consequence, we do not know the elution time for the unconjugated QDs.

We again investigate the separate fractions by other characterization techniques. Figure 7.5A shows the presence of QDs in the first peak and the presence of GOX in the second peak. The UV/visible absorption spectrum of some representative fractions is shown in figure 7.5B. An increasing absorption towards the UV is seen for fractions 5 to 9, in accordance with the presence of QDs. Fraction 13 shows the characteristic absorption maxima of GOX. Although the overall absorbance is quite low, some interesting observations can be made. For instance, the fractions containing QDs show an absorption feature at 400 nm that becomes larger as the fraction number increases. This feature at 400 nm is not present in the absorption spectrum of pure QDs nor in that of pure GOX. It is also absent in the spectra shown in figure 7.2B. This feature possibly indicates the binding of GOX on QDs, whereby the electrostatic adsorption or the covalent bonding has altered the spectrum of GOX.

We measured the ζ-potential of two fractions falling within the QD peak.

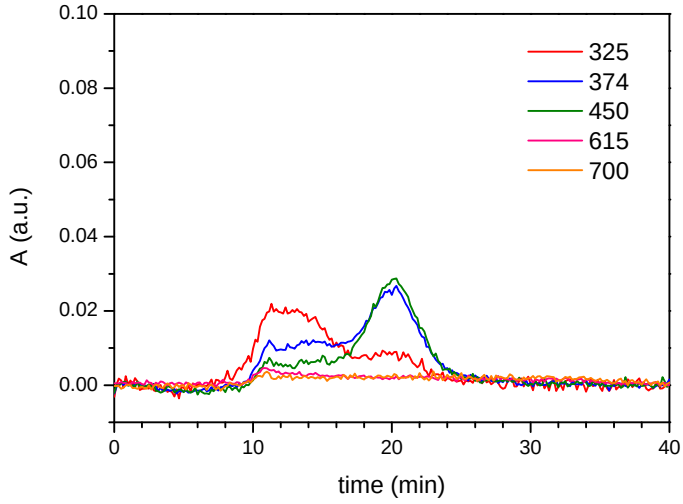

Figure 7.4 – GFC on GOX-functionalized micelle-encapsulated QDs (electrostatic + covalent binding). The UV/visible absorption versus time is shown at five different wavelengths (325, 374, 450, 615, and 700 nm). Experimental details: see figure 7.1.

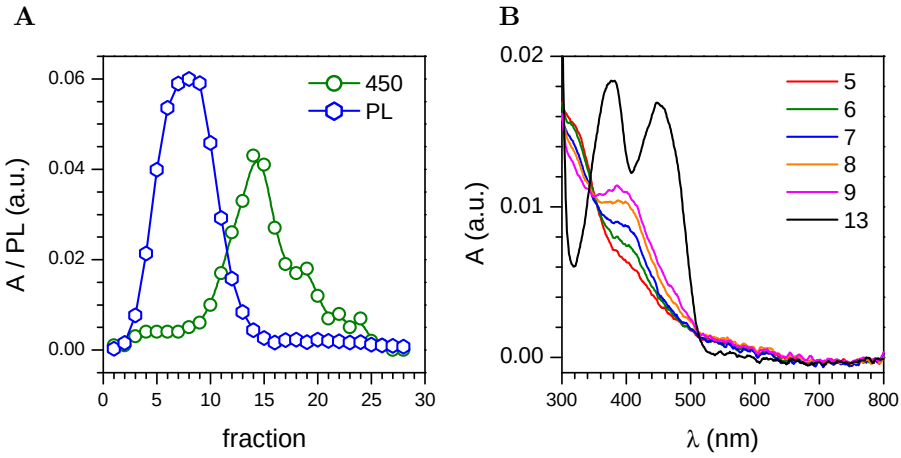

Figure 7.5 – Study of the separate GFC fractions of GOX-functionalized QDs (electrostatic + covalent binding). **(A)** Absorbance (at 450 nm) and PL intensity of the GFC fractions for GOX-functionalized QDs. **(B)** UV/visible absorption spectra of some selected fractions.

Sample	pH	ζ-potential (mV)
QDs	8.1	+7.7 ± 0.2
QDs+GOX: fraction 3	8.5	-10 ± 4
QDs+GOX: fraction 8	8.5	-6±1

Table 7.1 – ζ-potential values for non-functionalized QDs and for two fractions of GOX-functionalized QDs (electrostatic and covalent binding). QDs are micelle-encapsulated with micelles consisting of 100% DSPE-PEG amine.

Table 7.1 shows the ζ-potential of the QDs before and after functionalization with GOX. Initially, the ζ-potential of the non-functionalized amine QDs is positive. However, after biofunctionalization with GOX, the ζ-potential becomes negative. Because bioconjugated QDs would have a shell of negatively charged GOX, this result suggests that the bioconjugation of QDs with GOX was successful. We remark that fractions 3 and 8, of which the ζ-potential was measured, are almost certainly contaminated with free GOX. Figures 7.4 and 7.5A show that the peaks corresponding to QDs and GOX overlap. Moreover, the AFM measurements discussed below confirm the presence of GOX in fractions 6 and 9. However, the influence of small amounts of GOX (as in fraction 3) on the measured ζ-potential is expected to be negligible, because QDs are the stronger scatterers compared to GOX.

Finally, we performed AFM measurements on two fractions of bioconjugated QDs to investigate the particle sizes and distributions. Aliquots of the two fractions were deposited on silicon substrates. The silicon substrates were treated with poly(allylamine) hydrochloride to obtain a positively charged surface that can attract the negatively charged GOX and GOX-functionalized QDs. Figure 7.6 shows the surfaces after the deposition of fractions 6 and 9. From these images, it is clear that two types of particles with different sizes are present on the surface, supposedly GOX and GOX-functionalized QDs. The height profile for fraction 6 shows one particle with a height of approximately 11 nm. The height profile for fraction 9 shows one larger particle measuring ~9 nm and several smaller particles measuring ~2 nm, most likely corresponding to a QD and GOX enzymes respectively.

The peak height distributions shown in figure 7.6 are based on 3×3 μm^2 scans (supplementary figure 7.7). Note again that these are not conventional height distributions (see section 2.7). The peak height distributions reveal a bimodal distribution for fraction 6 and a trimodal distribution for fraction 9. From the AFM data, it is clear that fraction 9 contains a large amount of GOX enzymes next to the QDs, while fraction 6 contains GOX and QDs in more or less similar amounts. For fraction 9, an additional peak (shoulder) can be observed between 4 and 6 nm. This peak may be due to the stacking of two GOX molecules or due to a different orientation of GOX on the surface. The average QD height calculated from the height distributions is 10.0 nm ($n = 45$,

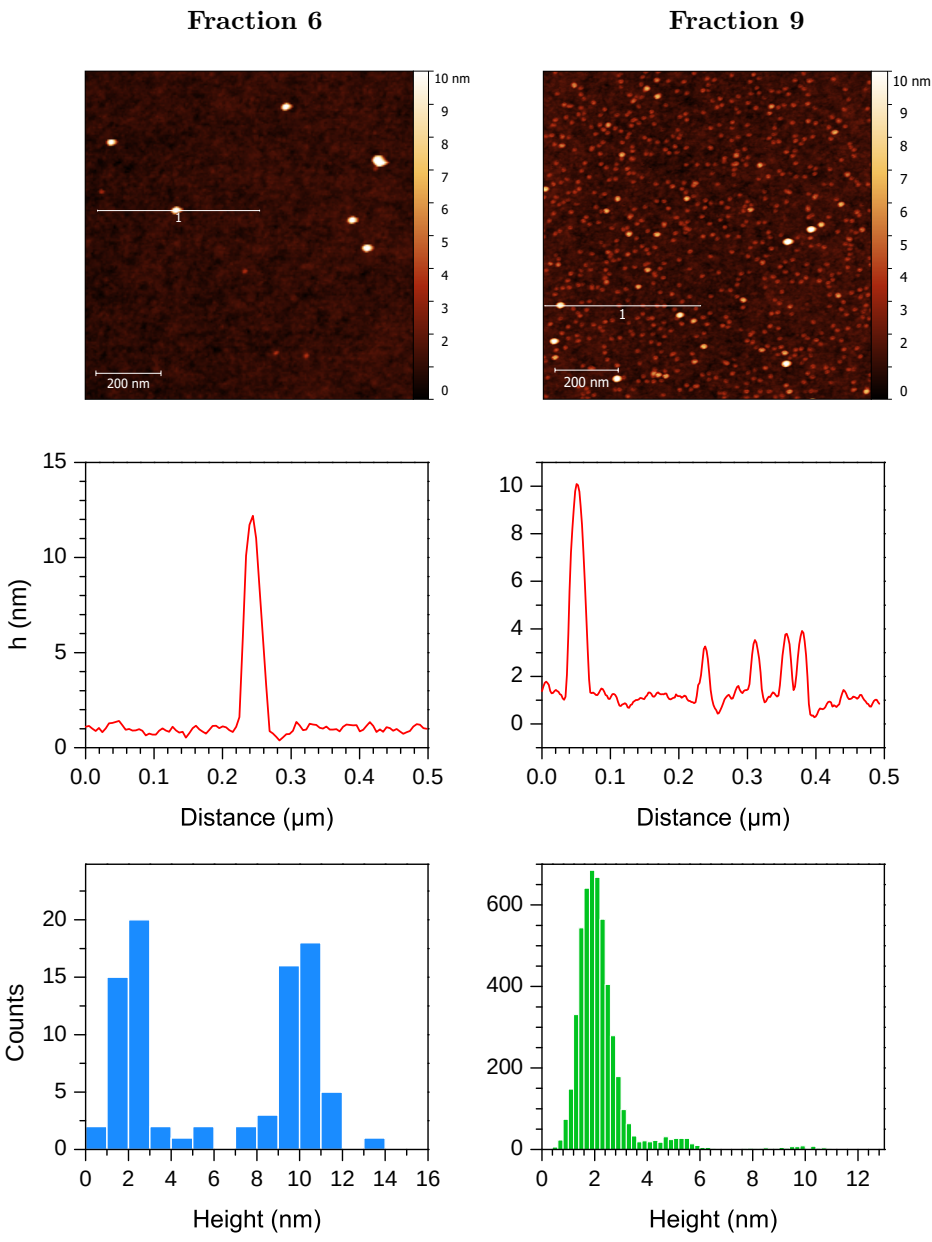

Figure 7.6 – AFM topography images and extracted data for fractions 6 (left) and 9 (right). **Top:** AFM topography images (1×1 µm^2). **Middle:** Line profiles corresponding to the white marker lines in the top images. **Bottom:** Peak height distributions based on the 3×3 µm^2 AFM topography images (figure 7.7).

σ = 1.1 nm) for fraction 6 and 9.6 nm (n = 71, σ = 1.0 nm) for fraction 9. For unconjugated QDs (QSP-630), the average particle height is 9.0 nm (section 4.3). The average particle height of the bioconjugated QDs is thus slightly larger than that of the unconjugated QDs. This can be expected because a shell of GOX around the QDs will increase the average particle size. However, the difference of ~1 nm is smaller than expected. Moreover, the unconjugated QDs and the bioconjugated QDs were deposited on different surfaces (respectively bare silicon dioxide and silicon dioxide covered with poly(allylamine) hydrochloride), which produces additional uncertainty when comparing these two samples. Moreover, a close-up AFM image (supplementary figure 7.8) shows no sign of an internal structure for the single QD-GOX assemblies: they appear as uniform, nearly spherical particles.

Overall, our experiments suggest that the bioconjugation was successful. Visual observations (aggregate formation), ζ-potential measurements and UV-visible spectroscopy indicate the interaction between GOX and QDs. The AFM data reveal a small size increase for the bioconjugated QDs compared to the unconjugated QDs, but the data is not conclusive. Gel electrophoresis could provide more conclusive information on the success of the bioconjugation [22]. The migration of the QDs in response to an electric field gives information on their surface charge. A successful bioconjugation is expected to cause a reversal of the QD surface charge. Therefore, the migration pattern of QDs should be different before and after successful bioconjugation (with unconjugated QDs being attracted to the anode and bioconjugated QDs being attracted to the cathode). Another technique that could probe the charge of the deposited particles is Kelvin probe force microscopy (KPFM). This is an AFM-based technique to simultaneously map the topography and electrostatic surface potential of a sample. Measuring the surface potential of nanoparticles such as QDs challenges the resolution of this technique. However, the lateral resolution of KPFM can be improved by using the so-called frequency-modulation method [166]. KPFM has been used to image surface charges of individual biomolecules such as avidin and DNA [167].

7.5 Conclusion

The bioconjugation of micelle-encapsulated QDs with GOX was attempted by three different approaches. The first approach was covalent crosslinking between carboxylic acid groups on the micelle-encapsulated QDs and amine groups on the enzymes using the well-established EDC-NHS crosslinking scheme. Gel filtration chromatography was used to separate excess GOX from biofunctionalized QDs. Inspection of the gel filtration profiles as well as examination of the collected size fractions indicated that the bioconjugation by this method was not successful. Most likely, the electrostatic repulsion between GOX and QDs, which are both negatively charged, prevented the crosslinking reaction. The second approach was based on the electrostatic attraction between positively charged micelle-encapsulated QDs and negatively charged GOX. However, the electrostatic attraction resulted in the formation of large aggregates that precipitated out of the solution. The third approach was based on a combination of covalent crosslinking and electrostatic adsorption. The COOH-groups of GOX were first activated by EDC-NHS. Then positively charged amine-functionalized QDs were added. Zeta potential measurements showed that the charge of the QDs, which was initially positive, became negative after performing this bioconjugation protocol. The UV-visible absorption spectra of the size fractions containing QDs showed an additional peak at 400 nm that may be due to the binding of GOX. AFM measurements showed that the QD fractions contained a considerable amount of free GOX, illustrating the need for improving the purification protocol. The AFM height distributions did not reveal an increase in particle size for the QDs, as would be expected after successful bioconjugation with GOX. Additional measurements using other techniques such as gel electrophoresis are required to be conclusive about the success of the bioconjugation.

7.6 Supplementary figures

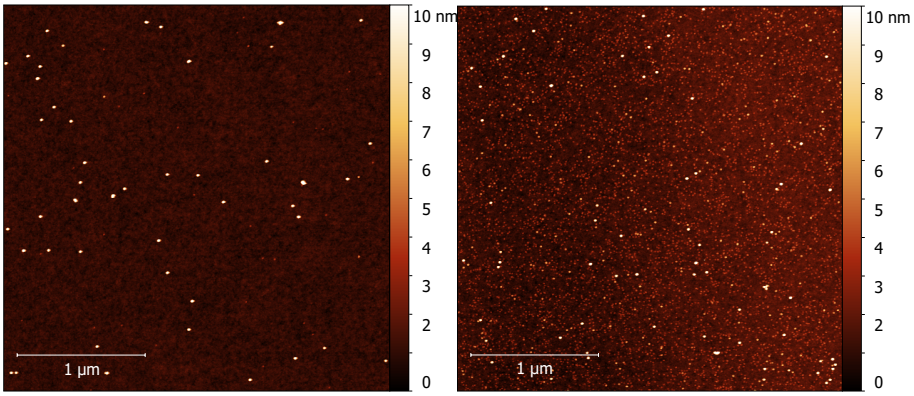

Figure 7.7 – AFM topography images (3×3 µm^2) of fractions 6 (left) and 9 (right). Experimental details: Silicon wafer pieces were cleaned with piranha solution (3:1 mixture of sulfuric acid and hydrogen peroxide resp.) and subsequently incubated in poly(allylamine) hydrochloride solution (1 mg/ml, filtered through 0.2 micron filter) for 5 min. The substrate was rinsed with MES buffer (0.1 M, pH 6.5) and UPW. The substrate was dried under a nitrogen stream and QDs were drop cast followed by a final rinsing step with UPW.

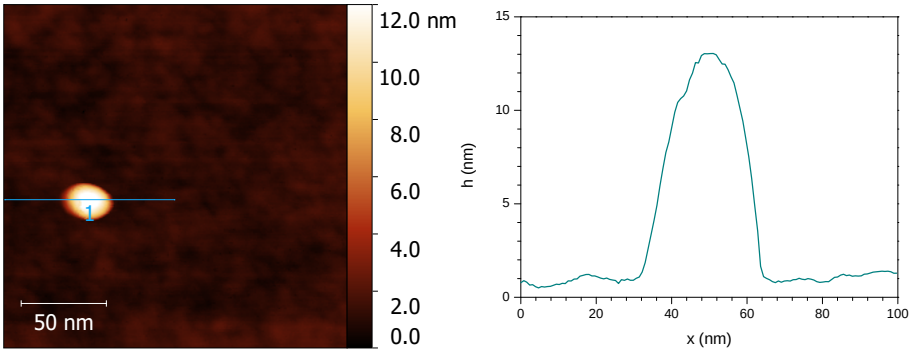

Figure 7.8 – Close-up AFM image with height profile for fraction 6. The image spans an area of 0.2 x 0.2 µm².

Chapter 8

Interaction of quantum dots with glucose oxidase

In this chapter we describe the interaction between colloidal QDs and GOX. More specifically, we discuss the influence of the GOX enzymatic reaction on the QD PL. Section 8.1 introduces some previous works concerning the biosensing with GOX and QDs. In section 8.2 we discuss the interaction between the activity of *free* GOX and QDs. In section 8.3 we do the same for GOX-functionalized QDs. Finally, the conclusion of this chapter is given in section 8.4

8.1 Introduction

The unique optoelectronic properties of QDs may enable a new generation of robust biosensors [168]. One of the routes being explored is the combination of QDs with enzymes [12, 13, 18, 122, 169, 19, 170, 171, 172, 173, 174]. In most cases, the biosensing is based on the interaction between the enzymatic reaction and the photoluminescent or photoconductive properties of the QDs. The successful development of this new class of biosensors requires an understanding of the mechanism behind the enzyme-QD interaction. The mechanism will be different for different types of enzymes.

We have chosen *glucose oxidase* (GOX) as our model enzyme. GOX is the most widely used enzyme as an analytical reagent for the determination of glucose, because of its relatively low cost and good stability [175]. Many commercial blood glucose meters are based on GOX. GOX is an oxido-reductase that catalyzes the oxidation of glucose to D-glucono-1,5-lactone and hydrogen peroxide (H_2O_2). The reaction is given by:

$$\beta\text{-D-glucose} + O_2 \rightarrow \text{D-glucono-1,5-lactone} + H_2O_2.$$

This reaction is often coupled to the action of a peroxidase to visualize the formed hydrogen peroxide.

Several groups have reported on the influence of the GOX reaction on the PL of QDs, which is mediated through H_2O_2. Gill *et al.* demonstrated that the sensitivity of CdSe/ZnS QDs towards H_2O_2 can be used for the detection of glucose [19]. QDs were functionalized with fluorescein isothiocyanate-modified avidin and subsequently coupled to biotin-modified GOX. Two fluorescence signals, one originating from the fluorescein and one from the QDs, were used for ratiometric PL measurements. In the presence of glucose, the PL signal of the fluorescein remained constant, whereas the PL of the QDs became quenched. The quenching of the QD PL was attributed to the H_2O_2 produced by GOX. The detection limit for H_2O_2 was 0.1 mM. The detection limit for glucose is not explicitly stated in the article, but appears to be slightly higher (~1 mM). Also the sensitivity for glucose in the range $1 - 10$ mM is less than the sensitivity for H_2O_2 in the same range.

Wu *et al.* found that H_2O_2 also effectively quenches the room temperature phosphorescence of Mn-Doped ZnS QDs [170]. The authors bioconjugated these QDs with GOX by using EDC/NHS and found that the addition of glucose quenched the phosphorescence. They noted that the interaction of H_2O_2 with the QDs requires a relatively long time (~15 min). They also investigated the effect of temperature and pH on the quenching process. They found that the optimal pH range for free GOX and QDs ($6.2 - 7.8$) is shifted towards slightly more basic values for the GOX-conjugated QDs ($7.4 - 8.6$).

8.2 Interactions with free glucose oxidase

Figure 8.1 shows the effect of added glucose on the PL of QDs in the presence of GOX. The PL is quenched for concentrations of 10 µM and higher. The PL quenching by the activity of GOX is not surprising, because the reaction product H_2O_2 is a known quencher of QD PL [176]. Figure 8.2 shows the effect of adding H_2O_2 on the PL intensity. H_2O_2 concentrations above 10 µM cause quenching of the PL intensity. However, H_2O_2 may not be solely responsible for the PL quenching by active GOX. Hydrolysis of the second enzymatic product, D-glucono-1,5-lactone, yields gluconic acid [177]. Chapter 6 has clearly illustrated the effect of low pH on the PL of QDs. However, the spectra shown in the left panel of figure 8.1 were measured in MES buffer, and the pH of this buffered solution should remain nearly constant upon the addition of small amounts of acid. The right panel of figure 8.1 shows the PL intensity quenching in both UPW and MES buffer. The PL intensity quenching is similar in both cases, suggesting that the generation of gluconic acid plays no significant role in the PL quenching. The quenching is also accompanied by a spectral blueshift. The reason for this shift requires further examination, but may be caused by similar mechanisms as those discussed in chapter 6.

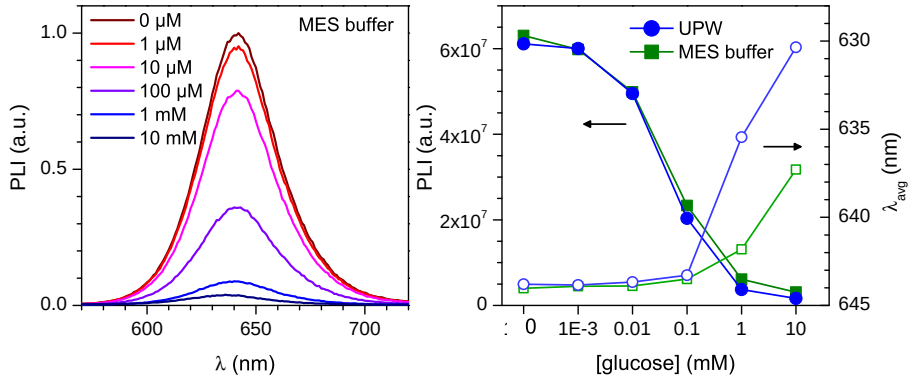

Figure 8.1 – Glucose titration of micelle-encapsulated QDs mixed with GOX. **Left:** PL spectra of QDs in MES buffer (0.05 M MES, pH 6.0) for different concentrations of glucose. **Right:** Integrated PL intensity (■ ●) and average PL wavelength (□ ○) versus glucose concentration for QDs in UPW and MES buffer. Experimental details: aliquots of the QD stock solution (Lumidot™ 640 QDs encapsulated with 100% DSPE-PEG COOH) were dissolved in MES buffer solutions and UPW solutions that contained different glucose concentrations.

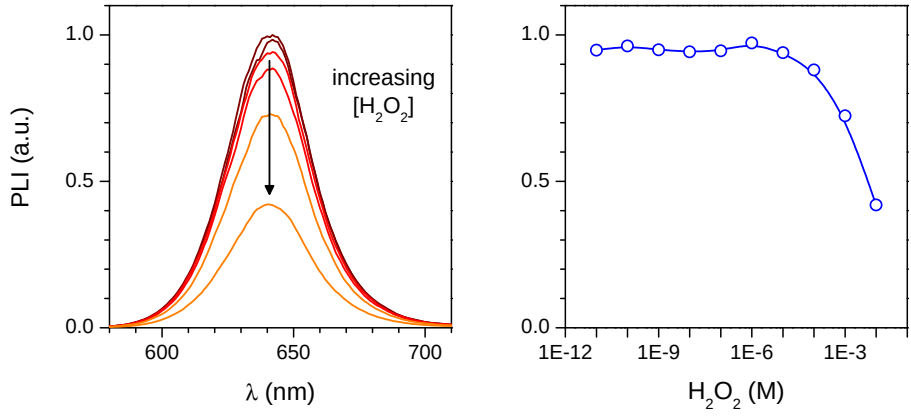

Figure 8.2 – Titration of micelle-encapsulated QDs in phosphate buffer with H_2O_2 in the concentration range 10 mM - 10 fM. **Left:** PL spectra of QDs in the presence of different H_2O_2 concentrations. **Right:** Integrated (normalized) PL intensity versus H_2O_2 concentration. Experimental details: aliquots of the QD stock solution (Lumidot™ 640 QDs encapsulated with 100% DSPE-PEG COOH) were dissolved in UPW solutions that contained different concentrations of H_2O_2.

Earlier reports have shown that the PL quenching is time-dependent [19, 170]. This is not surprising, because the generation and concentration of the enzymatic reaction products is time-dependent. The spectra shown in figure 8.1 are therefore snapshots taken at a certain time after the glucose addition. Figure 8.3 shows time traces of the PL intensity before and after the addition of glucose. The top panel shows the response of the PL in the absence of GOX. The additions of UPW and glucose solution are noticeable as (small) perturbations in the PL intensity trace. For instance, the second addition of glucose causes a drop in the PL intensity of more than 6%. After this drop, the PL intensity slowly rises. The reason for the PL intensity drop and its slow recovery is not clear. The bottom panel shows time traces in the presence of GOX. The first addition of 1 mM glucose causes a drop in the PL intensity of approximately 10%, after which the PL intensity recovers slowly. The second addition causes more spectacular changes. The PL intensity drops by more than 20%. It then shows a short moment of increase, but subsequently decreases further down to 60% of the original intensity.

8.3 Interactions with bioconjugated glucose oxidase

There are two interesting questions concerning the biofunctionalization of QDs with GOX. Firstly, do the bound enzymes remain active and secondly, is the interaction between QDs and GOX enhanced by the close proximity that results from the binding of GOX directly on the QDs. To answer these questions, three of the GOX-functionalized QD fractions shown in figure 7.5A were measured, namely fractions 2, 4, and 7. In chapter 7 we have shown, through AFM analysis, that fractions 6 and 9 still contain considerable amounts of free GOX, even after GFC. Fraction 7 will therefore also contain large amounts of free GOX, while fractions 2 and 4 should contain less free GOX. In any case, the presence of free GOX enzymes makes it hard to investigate the activity of the bound GOX separately.

It is also important to consider the pH of the solution in which the QDs are dispersed, because the activity of GOX is pH-dependent, having a maximum activity between pH 5.0 and 6.0 [178]. The QDs on the other hand are dispersed in borate buffer (pH 8.5) after size-separation by GFC. To ensure a better activity of GOX, we replaced the borate buffer solution for fraction 7 by a MES buffer (pH 6.5) using a dialysis membrane. We choose to work at a pH of 6.5 and not lower, to avoid extensive pH quenching of the QD PL. The QDs in fractions 2 and 4 were left in borate buffer.

Figure 8.4 shows the effect of adding glucose to GOX-functionalized QDs. For fraction 2, the PLI is increasing during the first 20 minutes. This is most likely due to photobrightening. Indeed, our samples were stored in the dark prior to the PL measurements. The addition of UPW causes a drop in the PLI,

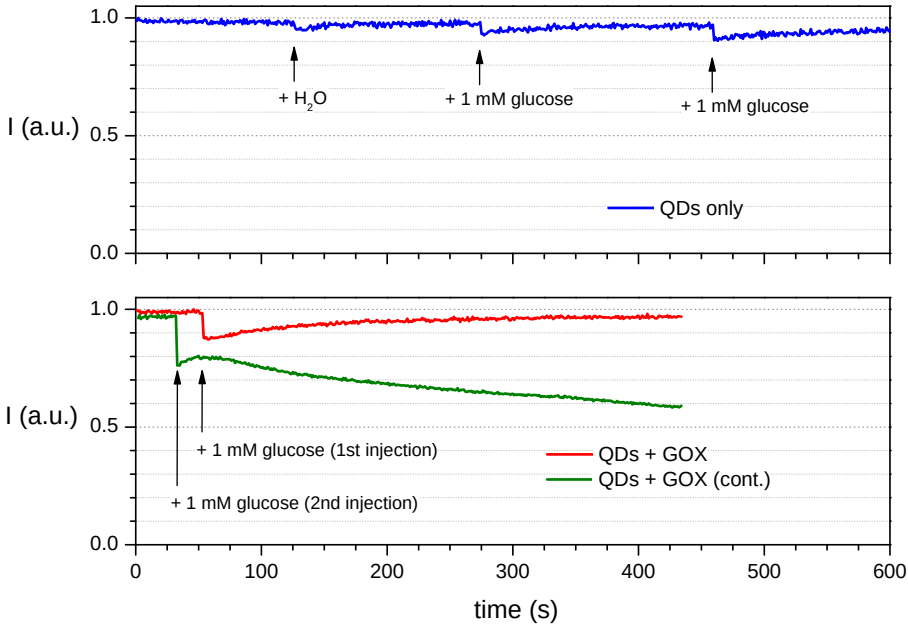

Figure 8.3 – Time traces of the PL intensity of QDs in the presence and absence of GOX activity. **Top:** control experiment to test the effect on the PL intensity of added solutions. The sample consists of QDs (no GOX) dispersed in UPW. The arrows indicate the addition of small volumes of UPW and glucose (1 mM final concentration). **Bottom:** testing the influence of the enzymatic reaction on the QD PL intensity. The sample consists of QDs and GOX (0.1 mg/ml) dispersed in UPW. The arrows indicate the addition of glucose (1 mM final concentration). The green curve is a continuation of the red curve.

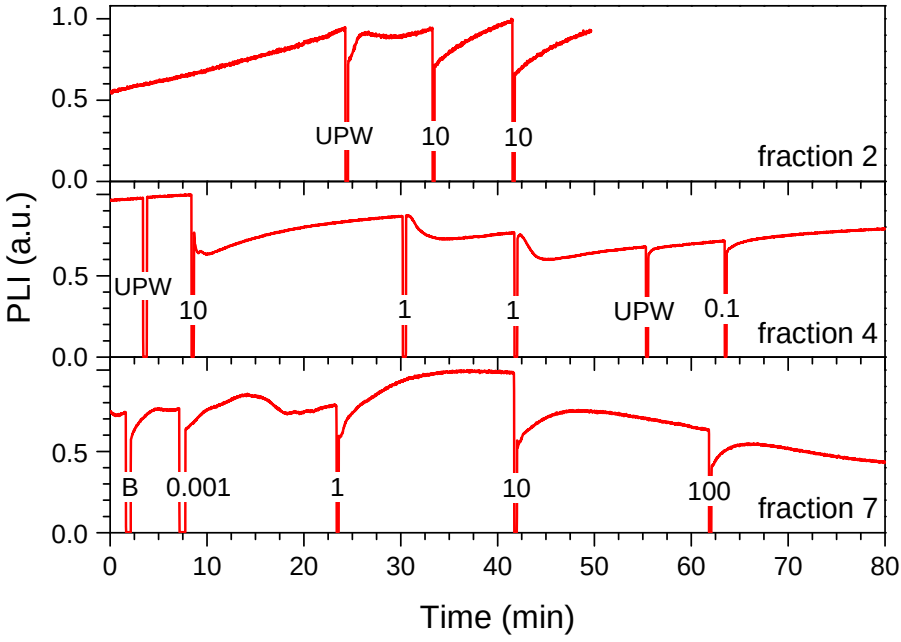

Figure 8.4 – PLI time traces for different fractions of GOX-functionalized QDs (fractions 2, 4, and 7 in figure 7.5A). For fractions 2 and 4, QDs are dispersed in borate buffer (pH 8.5, 20 mM borate, 0.10 M NaCl). For fraction 7, the borate buffer was replaced by MES buffer (pH 6.5, 50 mM MES, 10 mM NaCl) by means of dialysis. The labels UPW and B indicate the addition of 10 µl UPW and 10 µl buffer respectively. The label M means that the cuvette was moved in its holder. The numbers indicate the addition of 10 µl glucose solution, with the number itself giving the amount of glucose in µmol. The GOX-functionalized QDs were prepared according to protocol 7.3 and purified by GFC. The volume of the fractions was approximately 1 ml.

but it recovers within two minutes. The reason for the drop in PLI is not clear. Care was taken not to disturb the cuvette position during the addition. The addition of 10 µmol glucose also leads to a drop of the PLI. The recovery is slower than in the case of UPW addition. For fraction 4, the addition of UPW does not change the PLI, in contrast to the observation made for fraction 2. Upon the addition of 10 µmol of glucose, the PLI shows a strong drop, followed by a slow increase afterwards. The addition of 1 µmol glucose also decreases the PLI. For fraction 7, the addition of buffer causes a short-lived decrease. After the addition of 1 nmol glucose, the PLI is fluctuating in an unpredictable manner. After the addition of 1 µmol glucose, the PLI increases to a new high. The addition of 10 µmol glucose causes a large drop of the PLI. After the drop, the PLI increases temporarily, but then declines further. The addition of 100 µmol has a similar effect.

The above results show that the PLI quenching by the activity of GOX is a non-trivial matter. The effect of glucose addition is confounded by the fact that the addition of a control, such as UPW or buffer solution, may or may not change the PLI. In figure 8.4 for instance, it is not certain if the PLI drop following the addition of 1 mM glucose to fraction 7 is due to the activity of GOX or due to the addition itself. The PLI quenching by the action of GOX is also different for the three fractions. For fraction 2 there is an initial drop in PLI followed by an increase. For fraction 4, the initial drop is followed by a short period of further decrease and then a slow recovery. For fraction 7, the initial drop is followed by an increase, and then decrease of the PL intensity. These differences may be due to variations in the enzyme and QD concentrations or to the different buffer pH of fraction 7. The QD concentration decreases with decreasing fraction number (see figure 7.5A), fraction 7 having the highest and fraction 2 the lowest QD concentration. The concentration of *free* GOX on the other hand increases with fraction number. Fraction 7 thus contains the highest amount of GOX at a pH closer to the optimal pH range for the enzyme. Therefore it seems plausible to assume that the differences in PLI changes between the fractions originate mostly from differences in the activity of GOX.

We have several recommendations for future experiments to improve the data quality and facilitate the interpretation of the data. Firstly, we recommend to store the samples in daylight such that the photobrightening process has been completed by the time of measurement, thereby giving a more stable baseline for the PLI. Secondly, the fact that the injection of a control solution (UPW or buffer) may or may not elicit a PL response is problematic. The reason for the PL response is unclear and should be further investigated. In this experiment, glucose was added by addition of a small drop (~10 µl) to the QD solutions (~1 ml). Possibly, another approach of injecting the glucose solution may give more reproducible results (*e.g.* casting the drop on the walls of the cuvette such that it makes smoother contact with the QD solution). Thirdly, the PL measurement was interrupted during each glucose addition,

because opening the lid of the fluorimeter sample stage admits external light that can potentially overload the detector. However, by interrupting the measurement, we miss crucial information on the initial PL response right after the glucose addition. By use of filters or by placing the fluorimeter in a yellow room, the need for interrupting the measurement could be avoided. Fourthly, while we performed multiple glucose additions on the same sample (because of limited sample amount), this is clearly not optimal. For reproducible measurements, future experiments should use a fresh sample for each glucose addition. Finally, the presence of *free* (unbound) GOX should be avoided, because it obscures the activity of the bound GOX. Thus, the separation of GOX and GOX-functionalized QDs should be improved, for instance by introducing an additional purification step, a different purification method, or by optimizing the GFC column (*e.g.* by using a different gel matrix or longer column).

8.4 Conclusion

The enzymatic activity of GOX has a pronounced effect on the QD PL. We first performed measurements on solutions containing free GOX and QDs (*i.e.* GOX was not conjugated to the QDs). The PL intensity of the QDs was quenched upon the addition of glucose at concentrations as low as 10 µM. The PL quenching is attributable to the production of H_2O_2 by GOX. The indirect release of gluconic acid likely plays no significant role in the PL quenching. The PL intensity changes caused by the activity of GOX are time-dependent: the initial drop in PL intensity after glucose addition was followed by either a recovery or a further decrease of the PL intensity, depending on the sample history and on the added glucose concentration. Initial experiments on GOX-functionalized QDs showed a similar behaviour of the PL intensity upon the addition of glucose. The presence of free GOX in the samples obscured the activity of the conjugated GOX. Further experiments and improvements in the experimental approach are necessary to verify the activity of the conjugated GOX.

Conclusion

General conclusions

The goal of this thesis was to study enzymatic sensing with QDs. We performed this study on CdSe/ZnS QDs and *glucose oxidase* (GOX). The investigation was done on both colloidal QDs and surface-deposited QDs. For colloidal QDs, we investigated the optical photoluminescence (PL) properties of the QDs. For the surface-deposited QDs, we measured the photoconductive properties of the QDs. Our aim was to examine how these optoelectronic properties of QDs are affected by the enzymatic activity of GOX.

The first step in our work was the water-solubilization of QDs dispersed in apolar solvents (chapter 3). This was accomplished by three different methods: ligand exchange with dihydrolipoic acid (DHLA), polymer coating using poly(styrene-co-maleic anhydride) (PSMA), and phospholipid micelle encapsulation. We found that PSMA polymer coating and micelle-encapsulation were superior to DHLA-ligand exchange in terms of retaining the PL quantum yield. The obtained aqueous QD dispersions were in general not monodisperse. For micelle-encapsulated QDs, this is probably due to varying numbers of QDs inside the micelles. To narrow the size distribution of the water-soluble QDs and to remove unwanted organic material (such as empty micelles or excess polymer), we used gel-filtration chromatography. In this aspect, micelle-encapsulated QDs were preferred over PSMA-coated QDs, because the latter interacted with the gel matrix.

Chapter 4 deals with surface-deposited QDs. Hydrophilic QDs were deposited on surfaces to study their size and shape by atomic force microscopy (AFM). Micelle-encapsulated QDs and DHLA-capped QRs were successfully deposited on (functionalized) silicon substrates using electrostatic adsorption. We observed a remarkable size difference between red-emitting CdSe/ZnS QDs obtained from two different suppliers. The size difference could be due to differences in the ZnS shell (thickness). Differences in the build (quality) of the QDs may explain some of the observations regarding the pH-dependency (see below). To study enzymatic sensing with surface-deposited QDs, hydrophobic QDs were immobilized on thiol-modified gold electrodes. We were able

to generate electrochemical photocurrents in the µA range by illuminating the QD-modified gold electrodes. The wavelength-dependency of the photocurrent was similar to the absorption spectrum of the QDs, indicating that the photocurrents were mediated by the QDs. The electrostatic deposition of GOX on top of the QD film was not successful. The deposition protocol should be modified to increase the electrostatic attraction between the substrate and GOX.

In chapter 5, we investigated (environmental) factors that affect the PL of QDs. This investigation is important for the correct design and interpretation of the enzymatic sensing experiments. Firstly, we found that the PL spectrum was slightly red-shifted when increasing the QD concentration. We postulated that the redshift is due to reabsorption of PL emission. Secondly, the effect of electric fields on the QD PL was investigated by depositing hydrophobic QDs on a chip with interdigitated electrodes. The application of strong electric fields (~100 kV/cm) caused a reduction of the PL intensity as well as a spectral redshift. The observed PL changes are attributable to the quantum-confined Stark effect (QCSE). The QCSE can also be induced by local electric fields originating from charges near or at the QD surface. Thirdly, we found that the aggregation of QDs in solutions of high ionic strength ($\geq$ 0.1 M) was accompanied by a redshift of the PL. The PL redshift may be attributable to electronic energy transfer between QDs in the aggregates.

The last environmental factor we looked into was the pH (chapter 6). The influence of the pH is known in literature, but several issues remain to be clarified such as the role of the organic coating. We investigated the pH-dependent PL of CdSe/ZnS QDs for three types of organic coating, namely DHLA, PSMA, and phospholipid micelles. We made the following observations: (1) A decrease of the pH value leads to quenching of the PL intensity for all three coatings; (2) the PL intensity changes are accompanied by spectral shifts; (3) The pH-induced PL changes continue for several days; (4) the pH-dependent PL changes have a reversible and an irreversible component and the organic coating determines which component is dominant. Based on these experimental observations, we proposed the involvement of three mechanisms. The first mechanism, acid etching, is progressive with time and causes irreversible quenching of the PL at acidic pH values. Bulky organic coatings (*e.g.* micelles) may provide better protect against acid etching than thin organic cappings (*e.g.* DHLA). The second mechanism, pH-dependent surface passivation, involves the reversible binding of organic ligands such as thiols, phosphines, and amines. This mechanism may explain the reversible component of the PL intensity changes. The third mechanism is the QCSE, which causes a spectral redshift and a reduction in the PL intensity. The QCSE originates from electric fields caused by local charges and/or inhomogeneous organic cappings. The latter can result from surface depassivation, thus connecting the QCSE to the second mechanism. Together, these three mechanisms can explain the reversible and irreversible PL intensity and spectral changes. Our findings concerning the reversibility of

the pH quenching and the influence of the organic coating are an addition to the current knowledge about this topic. Next to the organic coating, we investigated the role of the QD composition in the pH-dependency of the PL. We observed that two batches of CdSe/ZnS QDs, provided by different suppliers, showed remarkably different pH-dependencies, indicating that factors such as the thickness of the ZnS shell play an important role. CdSe/CdS QRs showed a very different pH-dependency compared to CdSe/ZnS QDs. For instance, while the PSMA-coated QDs showed a decrease in the PL intensity with decreasing pH, PSMA-coated QRs showed the opposite behavior. This marks the importance of the role of the shell material composition.

In chapter 7, we discussed the bioconjugation of micelle-encapsulated QDs with GOX. The bioconjugation was attempted by three different approaches: covalent crosslinking using EDC-NHS, electrostatic binding, and covalent crosslinking combined with electrostatic binding. The first two approaches were not successful. The covalent crosslinking between COOH-functionalized QDs was most likely hindered by the electrostatic repulsion between GOX and QDs. The electrostatic binding between amine-functionalized QDs and GOX resulted in the formation of aggregates. The third approach on the other hand was likely successful. Amine-functionalized QDs were reacted with EDC-NHS-activated GOX. After the bioconjugation protocol, gel filtration chromatography was used to separate excess GOX from the biofunctionalized QDs. Measurements of the zeta potential showed that the charge of the QDs was reversed from positive to negative by the bioconjugation protocol, indicating the successful conjugation of GOX on QDs. AFM measurements however, did not provide solid evidence for the successful bioconjugation. They did show the presence of considerable amounts of free GOX in the QD size fractions, illustrating the need for improving the purification protocol. Additional measurements using other techniques such as gel electrophoresis are required to be conclusive about the success of the bioconjugation.

In chapter 8 finally, we investigated the interaction between GOX and micelle-encapsulated QDs. For a solution containing free GOX and QDs, the PL intensity of the QDs was quenched upon the addition of glucose at concentrations as low as 10 µM. The PL quenching was attributable to the production of H_2O_2 by GOX. The PL intensity changes caused by the activity of GOX were time-dependent. An initial drop in PL intensity was followed by either a recovery or a further decrease of the PL intensity, depending on the sample history and on the added glucose concentration. Initial experiments on GOX-functionalized QDs showed a similar behavior. The presence of free GOX in the solution made it impossible to separately investigate the activity of the bound GOX. Further experiments and improvements in the experimental approach are necessary to verify the activity of the bound GOX.

Outlook

This thesis contains useful guidelines for the water solubilization of QDs, the biofunctionalization of QDs with proteins, and the enzymatic biosensing with QDs. Below we give our recommendations for future research on these topics.

In chapter 4, we presented photoelectrochemical measurements on QD-modified gold electrodes. One of our original goals was to observe the modulation of the photoelectrochemical currents by the activity of GOX. This goal was not reached because the immobilization of GOX turned out to be unsuccessful. We propose that the electrostatic adsorption of GOX may be more successful by using a high ionic strength buffer during the immersion of the sample in the GOX solution. If still not successful, the ligand exchange with cysteamine should be followed by the deposition of a layer of polycations to increase the surface charge.

In chapter 6, we compared the pH-dependency of the PL for different QD types and for different organic coatings. Our experiments provided information on the underlying mechanisms that cause the pH-dependent PL changes. However, many questions still remain. With regard to the spectral shifting, we proposed the involvement of the QCSE, which is induced by local electric fields. In section 6.3.3, we listed several potential sources for the QCSE. Further research is needed to determine which of these sources are actually involved. One of the listed sources is the presence of an inhomogeneous surface capping. We suggested that such a capping may result from the pH-dependent surface depassivation or from the interaction of functional groups such as carboxylic acids with the surface. To prove the interaction of a certain functional group, we suggest comparing QDs with organic cappings that are different only in the presence of this functional group or that have a different pKa value for this functional group (the three organic coatings that were compared in this work are too different to provide such information).

We believe it is worthwhile to further investigate the reversible pH-dependent PL of micelle-encapsulated QDs. The striking correlation between PL intensity changes and spectral shifting suggests a connection between (at least) two mechanisms such as the QCSE and surface depassivation. The relatively robust reversibility of the PL changes is interesting from an application point of view. It also raises the question whether it is possible to create organic coatings that lead to even better reversibility.

With regard to the differences in pH-dependency between QDs of different material composition, several issues should be resolved. Firstly, we proposed that the different pH-dependency of QSP-630 QDs as compared to Lumidot™ 640 QDs could be due to differences in the ZnS shell thickness or quality. Researchers having experience with QD synthesis could test this hypothesis by preparing a series of QDs with different thicknesses of the ZnS shell. If our hypothesis is true, they should find that the pH quenching is less profound for QDs with a thicker shell. Secondly, the comparison between CdSe/ZnS

QDs and CdSe/CdS QRs is not ideal because there are too many differences between these nanocrystals, including the size, the shape, the shell material, and the native organic ligands. Ideally, CdSe/ZnS QDs should be compared to CdSe/CdS QDs of equal size that share the same ligands. This would allow the investigation of the influence of the shell material (ZnS vs CdS).

Concerning the bioconjugation of QDs with GOX, we showed that electrostatic interactions can both prevent and facilitate the bioconjugation. The bioconjugation of QDs by the combination of electrostatic adsorption and covalent crosslinking should be further investigated to confirm its success. Methods that could prove useful are gel electrophoresis and potentially Kelvin probe microscopy. Moreover, it should be confirmed by additional measurements that the feature at 400 nm in the UV-visible absorption spectrum of the bioconjugated QDs is attributable to GOX. If this is indeed the case, then the reason for the shift in the absorption maxima of GOX should be elucidated. There is also room for improvement regarding the purity of the samples. AFM measurements showed that the QD fractions contained considerable amounts of free, unbound GOX. The free GOX screens the activity of the bioconjugated GOX (which we want to measure), and should therefore be removed as much as possible. One of the options could be an additional passage through the gel filtration column.

In the last chapter we investigated the interaction between colloidal QDs and GOX. The measurements on the bioconjugated QDs should be repeated with samples that are free of unbound GOX. It should be avoided that the samples display photobrightening during the glucose titration. The equilibration time of the samples in the light beam should be increased until the photobrightening is complete. The injection of glucose and control solutions should be carefully controlled and if possible even automated. Measurements should also run continuously during the glucose titration and should not be interrupted during the addition of glucose solution. A fresh sample should be used for each glucose concentration.

Appendix A

Buffer preparation using pHTools

Britton-Robinson buffer

The Britton-Robinson buffer is a universal buffer that covers the pH range 2-12 [179]. Universal buffer solutions consist of mixtures of acids of diminishing strength, and the neutralization of these acids by addition of an alkali gives an approximately linear response of the pH with the amount of alkali added. The Britton-Robinson buffer is prepared by mixing equimolar amounts of acetic acid, phosphoric acid, and boric acid. The pH is adjusted to the desired value by adding sodium hydroxide.

The Matlab toolbox pHTools

pHTools is a toolbox for Matlab that can be used for the mathematical modelling of buffer systems, allowing the prediction of buffer capacity, ionic strength, and titration curves [180]. We used this toolbox to obtain the concentrations of the different ion species in the solution. Figure A.1 shows the output of pHTools for a 50 mM Britton-Robinson buffer. When the pH value approaches the pK_a value of one of the buffering acids, this acid changes its protonation state. The output also gives the amount of strong base that is required to reach a certain pH value (based on the assumption that the buffer is prepared with protonated acids).

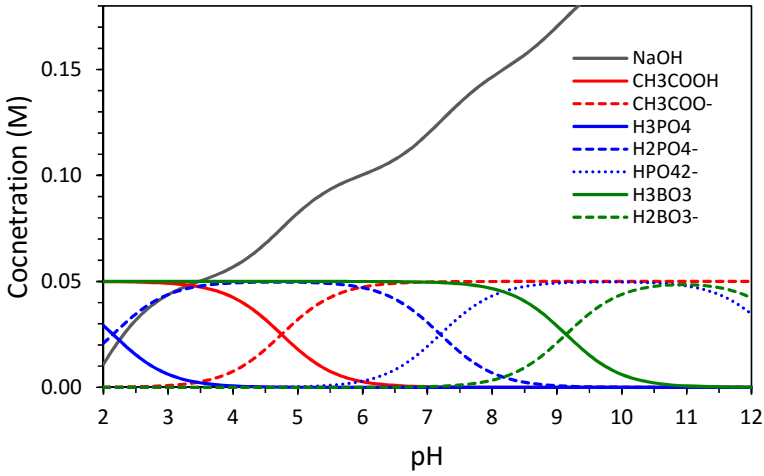

Figure A.1 – Graphical representation of a typical output from the $_{pH}$Tools software. The graph shows the concentrations of the different ionic species for a 50 mM Britton-Robinson buffer.

Constant ionic strength buffers

A buffer series can be prepared by adjusting the pH through the addition of a strong base. However, titration with a base changes the ionic strength (IS) of the solution, by dissociation of the strong base and by changes in the ionization state of the buffering acids (figure A.1). Consequently, the IS is pH-dependent. For some experiments, a constant IS is desirable (*e.g.* ζ-potential measurements). A crude method to obtain a constant IS buffer series is to add a large amount of NaCl to each buffer in the series, such that the ionic strength is almost completely determined by the NaCl concentration. The downside of this method is that it enables only the preparation of constant IS buffer series of high IS.

To prepare buffer series of constant low IS, the amount of NaCl to be added to each buffer in the series must be accurately calculated. This is were a software like $_{pH}$Tools is useful. The IS at each pH can be predicted with $_{pH}$Tools. The concentration of NaCl necessary to obtain a constant IS over a certain pH range can subsequently be calculated (figure A.2). The calculated quantities of NaOH and NaCl necessary to prepare a 50 mM Britton-Robinson buffer with constant IS (0.22 M) over the pH range $4-9$ are given in table A.1.

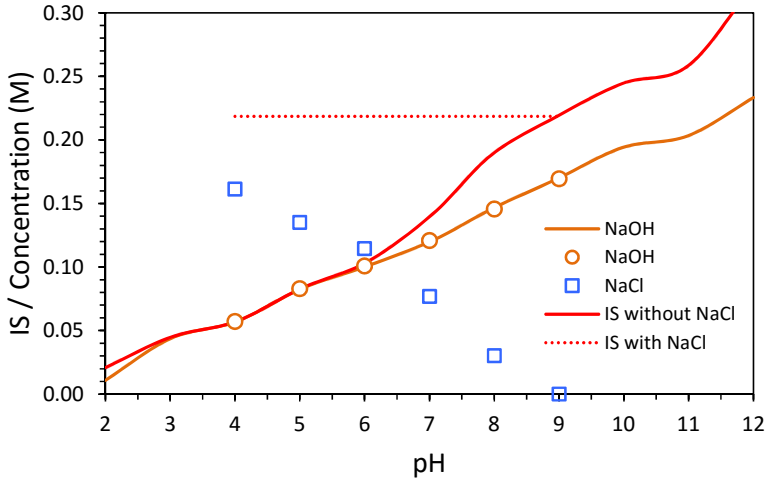

Figure A.2 – The ionic strength increases with increasing pH. The addition of NaCl in appropriate amounts can fix the ionic strength over the pH range $4-9$.

pH	NaOH	IS	NaCl	NaCl	new IS
	g	M	M	g	M
4.0	2.285	0.06	0.16	9.43	0.22
5.0	3.322	0.08	0.14	7.90	0.22
6.0	4.033	0.10	0.11	6.69	0.22
7.0	4.836	0.14	0.08	4.49	0.22
8.0	5.826	0.19	0.03	1.77	0.22
9.0	6.774	0.22	0.00	0.00	0.22

Table A.1 – Calculated amounts of NaOH and NaCl to prepare a 50 mM Britton-Robinson buffer with constant IS over the pH range $4-9$.

Appendix B

Fabrication of interdigitated electrodes

This appendix describes the process steps involved in the microfabrication of interdigitated electrodes. The photomask (soda-lime, inverted, 3-µm minimum feature size) was ordered from Compugraphics. The microfabrication procedure involves the following steps:

1. Cleaning of the silicon substrate;
2. Sputter deposition of titanium and gold. Titanium serves as an adhesion layer for gold on silicon;
3. Cleaning of the photomask and of the gold-coated silicon substrate;
4. Spin coating of the image reversal photoresist (AZ 5214 E);
5. Optical lithography step using a Carl Suss MA6 mask aligner;
6. Ion milling step to remove gold from areas that are not covered by resist;
7. Cleaning step to remove the resist that remains on the patterned gold.

The more detailed process sheet is presented in table B.1. Figure B.1 shows the finished interdigitated electrodes.

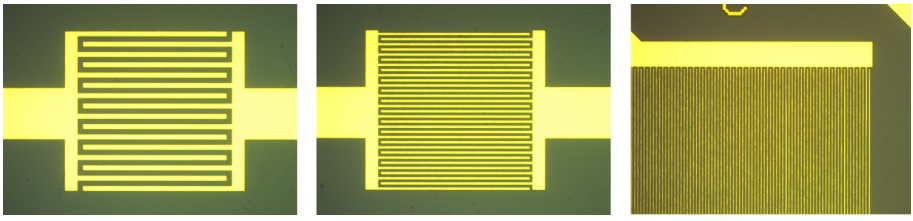

Figure B.1 – Interdigitated gold electrodes with 10 µm spacing (left), 5 µm spacing (middle), and 3 µm spacing (right).

Process	Step	Time
Mask cleaning	hot microstrip (ultrasonic bath)	15 min
	dirty IPA	5 min
	water rinse	
	clean IPA	5 min
	N-propanol	5 min
	N_2 dry gun	
Wafer cleaning	acetone (ultrasonic bath)	10 min
	hot acetone	3 min
	hot IPA	3 min
	N_2 dry gun	
	hot plate @ 90 °C	5 min
	O_2plasma	3 min
Sputter deposition	Ti (10 nm) + Au (100 nm)	
Optical lithography	apply resist AZ 5214 E	
	spin @ 5000 rpm	30 s
	prebake @ 110 °C	60 s
	hard mask exposure, 16 mW/cm^2	3 s
	reversal bake @ 120 °C	120 s
	flood exposure	5 s
	develop in AZ 351:H_2O (1:3.5)	2 x 30 s
	water rinse	
	N_2 dry gun	
	microscope inspection	
Ion milling	xenon ion mill, 16 cycles (30 s mill, 30 s wait)	16 x 30 s
	conductivity check	
Resist removal	warm acetone 50 °C	overnight
	beaker in ultrasonic bath	30 min
	hot acetone	5 min
	hot IPA	5 min
	N_2 dry gun	

Table B.1 – Process sheet for the fabrication of interdigitated electrodes by ion milling.

Appendix C

Flow cell design

We designed a flow cell for use with our gel-filtration chromatography setup. The flow cell allows us to examine the eluent by UV-visible spectroscopy. The flow cell consists of a polystyrene disposable cuvette or a quartz cuvette in which two homemade plastic (PEEK) pieces were glued. The first plastic piece is a rectangular cuboid with dimensions $9.9 \times 9.9 \times 10$ mm^3. It is glued to the bottom of the cuvette. The second piece is also a rectangular cuboid with dimensions $9.9 \times 9.9 \times 6$ mm^3, in which a center channel was carved and two holes were drilled. The second piece is glued on top of first piece. The design of these two pieces is shown in figure C.1. Tygon® tubes were inserted in the holes for the input and output of the eluent solution.

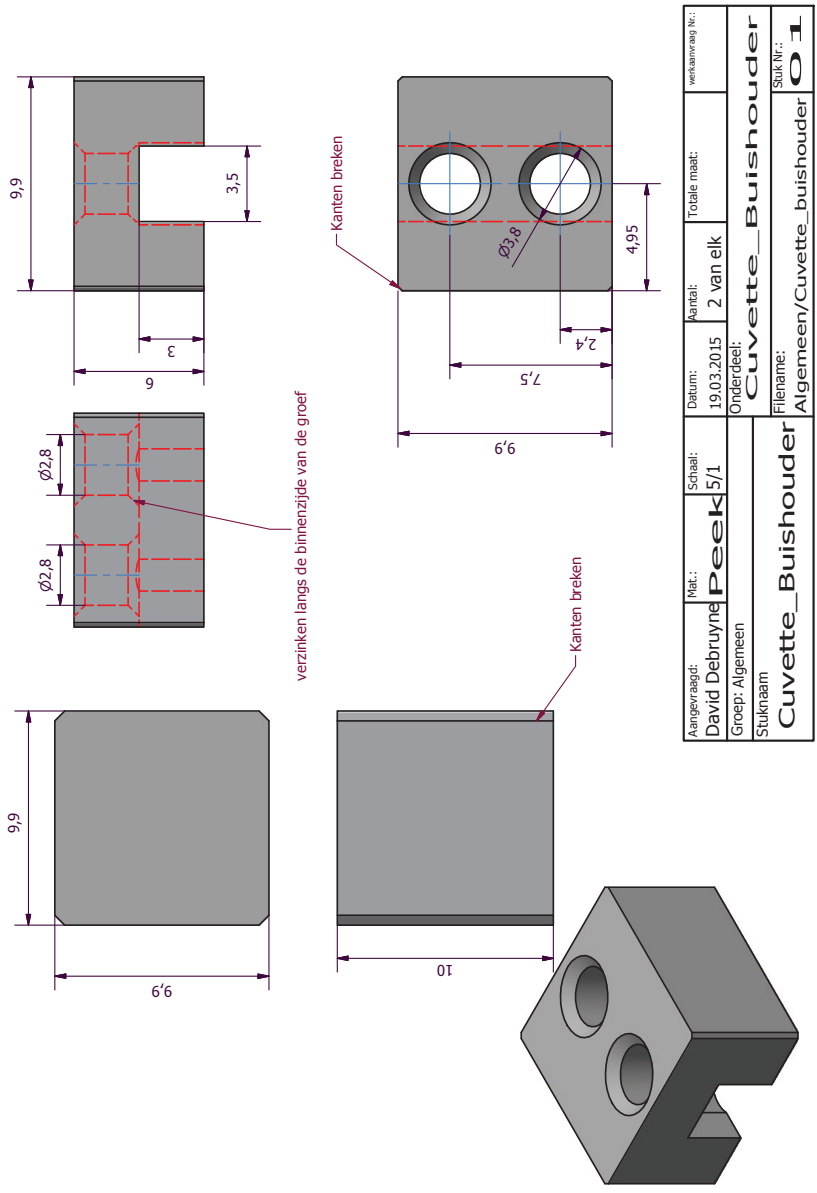

Figure C.1 – Design of the PEEK plastic pieces for the flow cell.

Bibliography

[1] Chan, W. C., Maxwell, D. J., Gao, X., Bailey, R. E., Han, M., and Nie, S. (2002). Luminescent quantum dots for multiplexed biological detection and imaging. *Curr. Opin. Biotechnol.*, *13* (1), 40–46. doi:10.1016/S0958-1669(02)00282-3.

[2] Michalet, X., Pinaud, F. F., Bentolila, L. a., Tsay, J. M., Doose, S., Li, J. J., Sundaresan, G., Wu, a. M., Gambhir, S. S., and Weiss, S. (2005). Quantum dots for live cells, in vivo imaging, and diagnostics. *Science*, *307* (5709), 538–544. doi:10.1126/science.1104274.

[3] Esteve-Turrillas, F. A. and Abad-Fuentes, A. (2013). Applications of quantum dots as probes in immunosensing of small-sized analytes. *Biosens. Bioelectron.*, *41* (1), 12–29. doi:10.1016/j.bios.2012.09.025.

[4] Willner, I., Basnar, B., and Willner, B. (2007). Nanoparticle-enzyme hybrid systems for nanobiotechnology. *FEBS J.*, *274* (2), 302–9. doi:10.1111/j.1742-4658.2006.05602.x.

[5] Frasco, M. F. and Chaniotakis, N. (2009). Semiconductor Quantum Dots in Chemical Sensors and Biosensors. *Sensors*, *9* (9), 7266–7286. doi:10.3390/s90907266.

[6] Coronado, J. M., Fresno, F., Hernández-Alonso, M. D., and Portela, R., eds. (2013). Design of Advanced Photocatalytic Materials for Energy and Environmental Applications, chap. Sensitizers: Dyes and Quantum Dots, pp. 329–343. Green Energy and Technology. Springer London, London. ISBN 978-1-4471-5060-2. doi:10.1007/978-1-4471-5061-9.

[7] Talapin, D. V., Lee, J.-S., Kovalenko, M. V., and Shevchenko, E. V. (2010). Prospects of Colloidal Nanocrystals for Electronic and Optoelectronic Applications. *Chem. Rev.*, *110* (1), 389–458. doi:10.1021/cr900137k.

[8] Klimov, V. I. (2000). Optical Gain and Stimulated Emission in Nanocrystal Quantum Dots. *Science*, *290* (5490), 314–317. doi:10.1126/science.290.5490.314.

[9] Algar, W. R., Tavares, A. J., and Krull, U. J. (2010). Beyond labels: A review of the application of quantum dots as integrated components of assays, bioprobes, and biosensors utilizing optical transduction. *Anal. Chim. Acta*, *673* (1), 1–25. doi:10.1016/j.aca.2010.05.026.

[10] Reiss, P., Protière, M., and Li, L. (2009). Core/Shell semiconductor nanocrystals. *Small*, *5* (2), 154–68. doi:10.1002/smll.200800841.

[11] Ji, X., Palui, G., Avellini, T., Na, H. B., Yi, C., Knappenberger, K. L., and Mattoussi, H. (2012). On the pH-Dependent Quenching of Quantum Dot Photoluminescence by Redox Active Dopamine. *J. Am. Chem. Soc.*, *134* (13), 6006–6017. doi:10.1021/ja300724x.

[12] Yuan, J., Guo, W., and Wang, E. (2008). Utilizing a CdTe quantum dots-enzyme hybrid system for the determination of both phenolic compounds and hydrogen peroxide. *Anal. Chem.*, *80* (4), 1141–5. doi:10.1021/ac0713048.

[13] Ma, W., Qin, L.-X., Liu, F.-T., Gu, Z., Wang, J., Pan, Z. G., James, T. D., and Long, Y.-T. (2013). Ubiquinone-quantum dot bioconjugates for in vitro and intracellular complex I sensing. *Scientific Reports*, *3*, 1537. doi:10.1038/srep01537.

[14] Heller, A. (1990). Electrical wiring of redox enzymes. *Acc. Chem. Res.*, *23* (5), 128–134. doi:10.1021/ar00173a002.

[15] Holland, J. T., Lau, C., Brozik, S., Atanassov, P., and Banta, S. (2011). Engineering of Glucose Oxidase for Direct Electron Transfer via Site-Specific Gold Nanoparticle Conjugation. *J. Am. Chem. Soc.*, *133* (48), 19262–19265. doi:10.1021/ja2071237.

[16] Xiao, Y., Patolsky, F., Katz, E., Hainfeld, J. F., and Willner, I. (2003). "Plugging into Enzymes": nanowiring of redox enzymes by a gold nanoparticle. *Science (New York, N.Y.)*, *299* (5614), 1877–81. doi:10.1126/science.1080664.

[17] Medintz, I. L., Clapp, A. R., Mattoussi, H., Goldman, E. R., Fisher, B., and Mauro, J. M. (2003). Self-assembled nanoscale biosensors based on quantum dot FRET donors. *Nat. Mater.*, *2* (9), 630–8. doi:10.1038/nmat961.

[18] Tanne, J., Schäfer, D., Khalid, W., Parak, W. J., and Lisdat, F. (2011). Light-Controlled Bioelectrochemical Sensor Based on CdSe/ZnS Quantum Dots. *Anal. Chem.*, *83* (20), 7778–7785. doi:10.1021/ac201329u.

[19] Gill, R., Bahshi, L., Freeman, R., and Willner, I. (2008). Optical Detection of Glucose and Acetylcholine Esterase Inhibitors by H2O2-Sensitive CdSe/ZnS Quantum Dots. *Angew. Chem.*, *47* (9), 1676–1679. doi:10.1002/anie.200704794.

[20] Mazumder, S., Dey, R., Mitra, M. K., Mukherjee, S., and Das, G. C. (2009). Review: Biofunctionalized Quantum Dots in Biology and Medicine. *J Nanomater*, *2009*, 1–17. doi:10.1155/2009/815734.

[21] Iyer, A., Chandra, A., and Swaminathan, R. (2014). Hydrolytic enzymes conjugated to quantum dots mostly retain whole catalytic activity. *Biochim. Biophys. Acta*, *1840* (9), 2935–2943. doi:10.1016/j.bbagen.2014.06.003.

[22] Song, F. and Chan, W. C. W. (2011). Principles of conjugating quantum dots to proteins via carbodiimide chemistry. *Nanotechnology*, *22* (49), 494006. doi:10.1088/0957-4484/22/49/494006.

[23] Wang, J., Huang, X., Zan, F., Guo, C.-G., Cao, C., and Ren, J. (2012). Studies on bioconjugation of quantum dots using capillary electrophoresis and fluorescence correlation spectroscopy. *Electrophoresis*, *33* (13), 1987–95. doi:10.1002/elps.201200024.

[24] Mattoussi, H., Matthew Mauro, J., Goldman, E. R., Anderson, G. P., Sundar, V. C., Mikulec, F. V., and Bawendi, M. G. (2000). Self-assembly of CdSe-ZnS quantum dot bioconjugates using an engineered recombinant protein. *J. Am. Chem. Soc.*, *122* (49), 12142–12150. doi:10.1021/ja002535y.

[25] Gerhards, C., Schulz-Drost, C., Sgobba, V., and Guldi, D. M. (2008). Conjugating luminescent CdTe quantum dots with biomolecules. *J. Phys. Chem. B*, *112* (46), 14482–14491. doi:10.1021/jp8030094.

[26] Debruyne, D., Deschaume, O., Coutiño-Gonzalez, E., Locquet, J.-P., Hofkens, J., Van Bael, M. J., and Bartic, C. (2015). The pH-dependent photoluminescence of colloidal CdSe/ZnS quantum dots with different organic coatings. *Nanotechnology*, *26* (25), 255703. doi:10.1088/0957-4484/26/25/255703.

[27] Masumoto, Y. and Takagahara, T., eds. (2002). Semiconductor Quantum Dots: Physics, Spectroscopy and Applications, 1st edition. Springer.

[28] Gaponenko, S. V. (1998). Optical Properties of Semiconductor Nanocrystals (Cambridge Studies in Modern Optics), 1 edition. Cambridge University Press. ISBN 0521582415.

[29] Wise, F. W. (2000). Lead Salt Quantum Dots: the Limit of Strong Quantum Confinement. *Acc. Chem. Res.*, *33* (11), 773–780. doi:10.1021/ar970220q.

[30] Norris, D. and Bawendi, M. (1996). Measurement and assignment of the size-dependent optical spectrum in CdSe quantum dots. *Phys. Rev. B*, *53* (24), 16338–16346. doi:10.1103/PhysRevB.53.16338.

[31] D.J. Norris, L. B., M.G. Bawendi (1997). Molecular Electronics, chap. Optical properties of semiconductor nanocrystals, pp. 281–323. Blackwell.

[32] Brus, L. E. (1984). Electron-electron and electron-hole interactions in small semiconductor crystallites: The size dependence of the lowest excited electronic state. *J. Chem. Phys.*, *80* (9), 4403–4409. doi:http://dx.doi.org/10.1063/1.447218.

[33] Murphy, C. J. and Coffer, J. L. (2002). Quantum Dots: A Primer. *Appl. Spectrosc.*, *56* (1), 16–27. doi:10.1366/0003702021954214.

[34] Bergman, L. and McHale, J. L., eds. (2011). Handbook of Luminescent Semiconductor Materials, chap. Fundamentals of the Quantum Confinement Effect, pp. 279–306. CRC Press. ISBN 9781439834671.

[35] Efros, A. L., Rosen, M., Kuno, M., Nirmal, M., Norris, D. J., and Bawendi, M. (1996). Band-edge exciton in quantum dots of semiconductors with a degenerate valence band: Dark and bright exciton states. *Phys. Rev. B*, *54*, 4843–4856. doi:10.1103/PhysRevB.54.4843.

[36] Chestnoy, N., Harris, T. D., Hull, R., and Brus, L. E. (1986). Luminescence and photophysics of cadmium sulfide semiconductor clusters: the nature of the emitting electronic state. *J. Phys. Chem.*, *90* (15), 3393–3399. doi:10.1021/j100406a018.

[37] Steigerwald, M. L., Alivisatos, A. P., Gibson, J. M., Harris, T. D., Kortan, R., Muller, A. J., Thayer, A. M., Duncan, T. M., Douglass, D. C., and Brus, L. E. (1988). Surface derivatization and isolation of semiconductor cluster molecules. *J. Am. Chem. Soc.*, *110* (10), 3046–3050. doi:10.1021/ja00218a008.

[38] Schmitt-Rink, S., Miller, D. A. B., and Chemla, D. S. (1987). Theory of the linear and nonlinear optical properties of semiconductor microcrystallites. *Phys. Rev. B*, *35*, 8113–8125. doi:10.1103/PhysRevB.35.8113.

[39] Wang, Y. and Herron, N. (1991). Nanometer-sized semiconductor clusters: materials synthesis, quantum size effects, and photophysical properties. *J. Phys. Chem.*, *95* (2), 525–532. doi:10.1021/j100155a009.

[40] Murray, C. B., Norris, D. J., and Bawendi, M. G. (1993). Synthesis and characterization of nearly monodisperse CdE (E = sulfur, selenium, tellurium) semiconductor nanocrystallites. *J. Am. Chem. Soc.*, *115* (19), 8706–8715. doi:10.1021/ja00072a025.

[41] Dabbousi, B. O., Rodriguez-Viejo, J., Mikulec, F. V., Heine, J. R., Mattoussi, H., Ober, R., Jensen, K. F., and Bawendi, M. G. (1997). (CdSe)ZnS Core-Shell Quantum Dots: Synthesis and Characterization of a Size Series of Highly Luminescent Nanocrystallites. *J. Phys. Chem. B*, *101* (46), 9463–9475. doi:10.1021/jp971091y.

[42] Bruchez Jr., M. (1998). Semiconductor Nanocrystals as Fluorescent Biological Labels. *Science*, *281* (5385), 2013–2016. doi:10.1126/science.281.5385.2013.

[43] Wolkin, M., Jorne, J., Fauchet, P., Allan, G., and Delerue, C. (1999). Electronic states and luminescence in porous silicon quantum dots: The role of oxygen. *Phys. Rev. Lett.*, *82* (1), 197–200. doi:10.1103/PhysRevLett.82.197.

[44] Dubertret, B., Skourides, P., Norris, D. J., Noireaux, V., Brivanlou, A. H., and Libchaber, A. (2002). In vivo imaging of quantum dots encapsulated in phospholipid micelles. *Science*, *298* (5599), 1759–62. doi:10.1126/science.1077194.

[45] Choi, H. S., Liu, W., Misra, P., Tanaka, E., Zimmer, J. P., Itty Ipe, B., Bawendi, M. G., and Frangioni, J. V. (2007). Renal clearance of quantum dots. *Nat. Biotechnol.*, *25* (10), 1165–1170. doi:10.1038/nbt1340.

[46] Kamat, P. V. (2008). Quantum Dot Solar Cells. Semiconductor Nanocrystals as Light Harvesters. *J. Phys. Chem. C*, *112* (48), 18737–18753. doi:10.1021/jp806791s.

[47] Walling, M. a., Novak, J. a., and Shepard, J. R. E. (2009). Quantum Dots for Live Cell and In Vivo Imaging. *Int. J. Mol. Sci.*, *10* (2), 441–491. doi:10.3390/ijms10020441.

[48] Resch-Genger, U., Grabolle, M., Cavaliere-Jaricot, S., Nitschke, R., and Nann, T. (2008). Quantum dots versus organic dyes as fluorescent labels. *Nat. Methods*, *5* (9), 763–775. doi:10.1038/nmeth.1248.

[49] Wang, F. and Hu, S. (2009). Electrochemical sensors based on metal and semiconductor nanoparticles. *Microchim. Acta*, *165* (1-2), 1–22. doi:10.1007/s00604-009-0136-4.

[50] Liao, L., Lu, H., Li, J., He, H., Wang, D., Fu, D., Liu, C., and Zhang, W. (2007). Size Dependence of Gas Sensitivity of ZnO Nanorods. *J. Phys. Chem. C*, *111* (5), 1900–1903. doi:10.1021/jp065963k.

[51] Harris, D. K. and Bawendi, M. G. (2012). Improved precursor chemistry for the synthesis of III-V quantum dots. *J. Am. Chem. Soc.*, *134* (50), 20211–20213. doi:10.1021/ja309863n.

[52] Derfus, a. M., Chan, W. C. W., and Bhatia, S. N. (2004). Probing the Cytotoxicity of Semiconductor Quantum Dots. *Nano Lett.*, *4* (1), 11–18. doi:Doi 10.1021/Nl0347334.

[53] Kirchner, C., Liedl, T., Kudera, S., Pellegrino, T., Muñoz Javier, A., Gaub, H. E., Stölzle, S., Fertig, N., and Parak, W. J. (2005). Cytotoxicity of Colloidal CdSe and CdSe/ZnS Nanoparticles. *Nano Lett.*, *5* (2), 331–338. doi:10.1021/nl047996m.

[54] (2011). Directive 2011/65/EU of the European parliament and of the council. Online. URL: `http://eur-lex.europa.eu/legal-content/EN/TXT/?uri=CELEX:02011L0065-20150624`.

[55] Fan, J. and Chu, P. K. (2010). Group IV Nanoparticles: Synthesis, Properties, and Biological Applications. *Small*, *6* (19), 2080–2098. doi:10.1002/smll.201000543.

[56] Smith, A. M. and Nie, S. (2010). Semiconductor nanocrystals: structure, properties, and band gap engineering. *Acc. Chem. Res.*, *43* (2), 190–200. doi:10.1021/ar9001069.

[57] Smith, A. M., Mohs, A. M., and Nie, S. (2009). Tuning the optical and electronic properties of colloidal nanocrystals by lattice strain. *Nat. Nanotechnol.*, *4* (1), 56–63. doi:10.1038/nnano.2008.360.

[58] Kim, S., Fisher, B., Eisler, H.-J., and Bawendi, M. (2003). Type-II Quantum Dots: CdTe/CdSe(Core/Shell) and CdSe/ZnTe(Core/Shell) Heterostructures. *J. Am. Chem. Soc.*, *125* (38), 11466–11467. doi:10.1021/ja0361749.

[59] Zhong, X., Feng, Y., Knoll, W., and Han, M. (2003). Alloyed Zn x Cd 1 - x S Nanocrystals with Highly Narrow Luminescence Spectral Width. *J. Am. Chem. Soc.*, *125* (44), 13559–13563. doi:10.1021/ja036683a.

[60] Bailey, R. E. and Nie, S. (2003). Alloyed semiconductor quantum dots: tuning the optical properties without changing the particle size. *J. Am. Chem. Soc.*, *125* (23), 7100–6. doi:10.1021/ja035000o.

[61] Buhro, W. E. and Colvin, V. L. (2003). Semiconductor nanocrystals: Shape matters. *Nat. Mater.*, *2* (3), 138–139. doi:10.1038/nmat844.

[62] Yu, H., Li, J., Loomis, R. a., Wang, L.-W., and Buhro, W. E. (2003). Two- versus three-dimensional quantum confinement in indium phosphide wires and dots. *Nat. Mater.*, *2* (8), 517–520. doi:10.1038/nmat942.

[63] Ithurria, S. and Dubertret, B. (2008). Quasi 2D Colloidal CdSe Platelets with Thicknesses Controlled at the Atomic Level. *J. Am. Chem. Soc.*, *130* (49), 16504–16505. doi:10.1021/ja807724e.

[64] Park, K., Deutsch, Z., Li, J. J., Oron, D., and Weiss, S. (2012). Single molecule quantum-confined Stark effect measurements of semiconductor nanoparticles at room temperature. *ACS Nano*, *6* (11), 10013–10023. doi:10.1021/nn303719m.

[65] R, J., Jones, A. M., Holmes, D., Reed, R., Weyers, J., and Jones, A. (2002). Practical skills in chemistry, chap. Basic spectroscopy, p. 167. Pearson Education.

[66] Würth, C., Grabolle, M., Pauli, J., Spieles, M., and Resch-Genger, U. (2013). Relative and absolute determination of fluorescence quantum yields of transparent samples. *Nat. Protoc.*, *8* (8), 1535–1550. doi:10.1038/nprot.2013.087.

[67] Dhami, S., Mello, a. J. D., Rumbles, G., Bishop, S. M., Phillips, D., and Beeby, A. (1995). Phthalocyanine fluorescence at high concentration: dimers or reabsorption effect? *Photochem. Photobiol.*, *61* (4), 341–346. doi:10.1111/j.1751-1097.1995.tb08619.x.

[68] Kubin, R. and Fletcher, A. (1983). Fluorescence quantum yields of some rhodamine dyes. *J. Lumin.*, *27* (4), 455 – 462. doi:http://dx.doi.org/10.1016/0022-2313(82)90045-X.

[69] Fery-Forgues, S. and Lavabre, D. (1999). Are Fluorescence Quantum Yields So Tricky to Measure? A Demonstration Using Familiar Stationery Products. *J. Chem. Educ.*, *76* (9), 1260. doi:10.1021/ed076p1260.

[70] Grabolle, M., Spieles, M., Lesnyak, V., Gaponik, N., Eychmüller, A., and Resch-Genger, U. (2009). Determination of the Fluorescence Quantum Yield of Quantum Dots: Suitable Procedures and Achievable Uncertainties. *Anal. Chem.*, *81* (15), 6285–6294. doi:10.1021/ac900308v.

[71] de Mello, J. C., Wittmann, H. F., and Friend, R. H. (1997). An improved experimental determination of external photoluminescence quantum efficiency. *Advanced Materials*, *9* (3), 230–232. doi:10.1002/adma.19970090308.

[72] Faulkner, D., McDowell, J., Price, A., Perovic, D., Kherani, N., and Ozin, G. (2012). Measurement of absolute photoluminescence quantum yields using integrating spheres - Which way to go? *Laser Photon. Rev.*, *6* (6), 802–806. doi:10.1002/lpor.201200077.

[73] Wahl, M. (2014). Time-Correlated Single Photon Counting. Technical Note PicoQuant. URL: http://www.picoquant.com/images/uploads/page/files/7253/technote_tcspc.pdf.

[74] Lakowicz, J. R. (2006). Principles of Fluorescence Spectroscopy, 3rd edition, chap. Time-Domain Lifetime Measurements, pp. 97–155. Springer.

[75] Eaton, D. F. (1990). Recommended methods for fluorescence decay analysis. *Pure Appl. Chem.*, *62* (8), 1631–1648. doi:10.1351/pac199062081631.

[76] Maus, M., Rousseau, E., Cotlet, M., Schweitzer, G., Hofkens, J., Van der Auweraer, M., De Schryver, F. C., and Krueger, A. (2001). New picosecond laser system for easy tunability over the whole ultraviolet/visible/near infrared wavelength range based on flexible harmonic generation and optical parametric oscillation. *Rev. Sci. Instrum.*, *72* (1), 36. doi:10.1063/1.1326930.

[77] Pike, R. and Pierre, S., eds. (2002). Scattering: Scattering and inverse scattering in Pure and Applied Science, chap. Practical aspects of visible and near-visible light scattering, pp. 895–919. Academic Press.

[78] Dynamic Light Scattering: An Introduction in 30 Minutes. URL: http://www.malvern.com/en/support/resource-center/technical-notes/TN101104DynamicLightScatteringIntroduction.aspx.

[79] Delgado, A. V., González-Caballero, F., Hunter, R. J., Koopal, L. K., and Lyklema, J. (2005). Measurement and Interpretation of Electrokinetic Phenomena (IUPAC Technical Report). *Pure Appl. Chem.*, *77* (10). doi:10.1351/pac200577101753.

[80] Ohshima, H. (1994). A Simple Expression for Henry's Function for the Retardation Effect in Electrophoresis of Spherical Colloidal Particles. *J. Colloid Interface Sci.*, *168* (1), 269–271. doi:10.1006/jcis.1994.1419.

[81] (2014). Application note: simplifying the measurement of zeta potential using M3-PALS. Online. URL: http://www.malvern.com/en/support/resource-center/application-notes/AN101104ZetaPotentialM3-PALS.aspx.

[82] Necas, D. and Klapetek, P. (2012). Gwyddion: an open-source software for SPM data analysis. *Central European Journal of Physics*, *10*, 181–188. doi:10.2478/s11534-011-0096-2.

[83] Eisenstein, M. (2006). A look back: adventures in the matrix. *Nat. Methods*, *3* (5), 410–410. doi:10.1038/nmeth0506-410.

[84] Love, J. C., Estroff, L. a., Kriebel, J. K., Nuzzo, R. G., and Whitesides, G. M. (2005). Self-assembled monolayers of thiolates on metals as a form of nanotechnology. *Chem. Rev.*, *105* (4), 1103–69. doi:10.1021/cr0300789.

[85] Liu, Y.-S., Sun, Y., Vernier, P. T., Liang, C.-H., Chong, S. Y. C., and Gundersen, M. a. (2007). pH-Sensitive Photoluminescence of CdSe/ZnSe/ZnS Quantum Dots in Human Ovarian Cancer Cells. *J. Phys. Chem. C*, *111* (7), 2872–2878. doi:10.1021/jp0654718.

[86] Chan, W. and Nie, S. (1998). Quantum Dot Bioconjugates for Ultrasensitive Nonisotopic Detection. *Science*, *281* (5385), 2016–2018. doi:10.1126/science.281.5385.2016.

[87] Uyeda, H. T. H., Medintz, I. I. L., Jaiswal, J. K., Simon, S. M., and Mattoussi, H. (2005). Synthesis of compact multidentate ligands to prepare stable hydrophilic quantum dot fluorophores. *J. Am. Chem. Soc.*, *127* (11), 3870–3878. doi:10.1021/ja044031w.

[88] Susumu, K., Oh, E., Delehanty, J. B., Blanco-Canosa, J. B., Johnson, B. J., Jain, V., Hervey, W. J., Algar, W. R., Boeneman, K., Dawson, P. E., and Medintz, I. L. (2011). Multifunctional compact zwitterionic ligands for preparing robust biocompatible semiconductor quantum dots and gold nanoparticles. *J. Am. Chem. Soc.*, *133* (24), 9480–96. doi:10.1021/ja201919s.

[89] Mitchell, G. P., Mirkin, C. a., and Letsinger, R. L. (1999). Programmed Assembly of DNA Functionalized Quantum Dots. *J. Am. Chem. Soc.*, *121* (35), 8122–8123. doi:10.1021/ja991662v.

[90] Green, M. (2010). The nature of quantum dot capping ligands. *J. Mater. Chem.*, *20* (28), 5797. doi:10.1039/c0jm00007h.

[91] Medintz, I. L., Uyeda, H. T., Goldman, E. R., and Mattoussi, H. (2005). Quantum dot bioconjugates for imaging, labelling and sensing. *Nat. Mater.*, *4* (6), 435–46. doi:10.1038/nmat1390.

[92] Jeong, S., Achermann, M., Nanda, J., Ivanov, S., Klimov, V. I., and Hollingsworth, J. a. (2005). Effect of the thiol-thiolate equilibrium on the photophysical properties of aqueous CdSe/ZnS nanocrystal quantum dots. *J. Am. Chem. Soc.*, *127* (29), 10126–7. doi:10.1021/ja042591p.

[93] Breus, V. V., Heyes, C. D., and Nienhaus, G. U. (2007). Quenching of CdSe-ZnS Core-Shell Quantum Dot Luminescence by Water-Soluble Thiolated Ligands. *J. Phys. Chem. C*, *111* (50), 18589–18594. doi:10.1021/jp075848p.

[94] Carion, O., Mahler, B., Pons, T., and Dubertret, B. (2007). Synthesis, encapsulation, purification and coupling of single quantum dots in phospholipid micelles for their use in cellular and in vivo imaging. *Nat. Protoc.*, *2* (10), 2383–90. doi:10.1038/nprot.2007.351.

[95] Lees, E. E., Nguyen, T.-L., Clayton, A. H. A., and Mulvaney, P. (2009). The Preparation of Colloidally Stable, Water-Soluble, Biocompatible, Semiconductor Nanocrystals with a Small Hydrodynamic Diameter. *ACS Nano*, *3* (5), 1121–1128. doi:10.1021/nn900144n.

[96] Gao, X., Cui, Y., Levenson, R. M., Chung, L. W. K., and Nie, S. (2004). In vivo cancer targeting and imaging with semiconductor quantum dots. *Nat. Biotechnol.*, *22* (8), 969–976. doi:10.1038/nbt994.

[97] Janczewski, D., Tomczak, N., Han, M.-Y., and Vancso, G. J. (2011). Synthesis of functionalized amphiphilic polymers for coating quantum dots. *Nat. Protoc.*, *6* (10), 1546–1553. doi:10.1038/nprot.2011.381.

[98] Gerion, D., Pinaud, F., Williams, S. C., Parak, W. J., Zanchet, D., Weiss, S., and Alivisatos, a. P. (2001). Synthesis and Properties of Biocompatible Water-Soluble Silica-Coated CdSe/ZnS Semiconductor Quantum Dots. *J. Phys. Chem. B*, *105* (37), 8861–8871. doi:10.1021/jp0105488.

[99] Borys, N. J., Walter, M. J., Huang, J., Talapin, D. V., and Lupton, J. M. (2010). The Role of Particle Morphology in Interfacial Energy Transfer in CdSe/CdS Heterostructure Nanocrystals. *Science*, *330* (6009), 1371–1374. doi:10.1126/science.1198070.

[100] Talapin, D. V., Nelson, J. H., Shevchenko, E. V., Aloni, S., Sadtler, B., and Alivisatos, A. P. (2007). Seeded Growth of Highly Luminescent CdSe/CdS Nanoheterostructures with Rod and Tetrapod Morphologies. *Nano Lett.*, *7* (10), 2951–2959. doi:10.1021/nl072003g.

[101] Kalyuzhny, G. and Murray, R. W. (2005). Ligand effects on optical properties of CdSe nanocrystals. *J. Phys. Chem. B*, *109* (15), 7012–21. doi:10.1021/jp045352x.

[102] Morris-Cohen, A. J., Donakowski, M. D., Knowles, K. E., and Weiss, E. a. (2010). The Effect of a Common Purification Procedure on the Chemical Composition of the Surfaces of CdSe Quantum Dots Synthesized with Trioctylphosphine Oxide. *J. Phys. Chem. C*, *114* (2), 897–906. doi:10.1021/jp909492w.

[103] Shakeri, B. and Meulenberg, R. W. (2015). A Closer Look into the Traditional Purification Process of CdSe Semiconductor Quantum Dots. *Langmuir*, *31* (49), 13433–13440. doi:10.1021/acs.langmuir.5b03584.

[104] Shen, Y., Gee, M. Y., Tan, R., Pellechia, P. J., and Greytak, A. B. (2013). Purification of Quantum Dots by Gel Permeation Chromatography and the Effect of Excess Ligands on Shell Growth and Ligand Exchange. *Chem. Mater.*, *25* (14), 2838–2848. doi:10.1021/cm4012734.

[105] Aldana, J., Lavelle, N., Wang, Y., and Peng, X. (2005). Size-dependent dissociation pH of thiolate ligands from cadmium chalcogenide nanocrystals. *J. Am. Chem. Soc.*, *127* (8), 2496–2504. doi:10.1021/ja047000+.

[106] Aldana, J., Wang, Y. a., and Peng, X. (2001). Photochemical instability of CdSe nanocrystals coated by hydrophilic thiols. *J. Am. Chem. Soc.*, *123* (36), 8844–8850. doi:10.1021/ja016424q.

[107] Gao, X., Chan, W. C. W., and Nie, S. (2002). Quantum-dot nanocrystals for ultrasensitive biological labeling and multicolor optical encoding. *J. Biomed. Opt.*, *7* (4), 532. doi:10.1117/1.1506706.

[108] Zhang, H., Zhou, Z., Yang, B., and Gao, M. (2003). The Influence of Carboxyl Groups on the Photoluminescence of Mercaptocarboxylic Acid-Stabilized CdTe Nanoparticles. *J. Phys. Chem. B*, *107* (1), 8–13. doi:10.1021/jp025910c.

[109] Berg, J., Tymoczko, J., and Stryer, L. (2002). Biochemistry. 5th edition, chap. Chapter 12. Lipids and Cell Membranes. W.H.Freeman: New York.

[110] Ashok, B., Arleth, L., Hjelm, R. P., Rubinstein, I., and Onyüksel, H. (2004). In vitro characterization of PEGylated phospholipid micelles for improved drug solubilization: effects of PEG chain length and PC incorporation. *J. Pharm. Sci.*, *93* (10), 2476–87. doi:10.1002/jps.20150.

[111] Kagan, C. R., Murray, C. B., Nirmal, M., and Bawendi, M. G. (1996). Electronic Energy Transfer in CdSe Quantum Dot Solids. *Phys. Rev. Lett.*, *76* (9), 1517–1520. doi:10.1103/PhysRevLett.76.1517.

[112] Di Corato, R., Quarta, A., Piacenza, P., Ragusa, A., Figuerola, A., Buonsanti, R., Cingolani, R., Manna, L., and Pellegrino, T. (2008). Water solubilization of hydrophobic nanocrystals by means of poly(maleic anhydride-alt-1-octadecene). *J. Mater. Chem.*, *18* (17), 1991. doi:10.1039/b717801h.

[113] Murray, C. B., Kagan, C. R., and Bawendi, M. G. (1995). Self-Organization of CdSe Nanocrystallites into Three-Dimensional Quantum Dot Superlattices. *Science*, *270* (5240), 1335–1338. doi:10.1126/science.270.5240.1335.

[114] Hu, K., Brust, M., and Bard, A. J. (1998). Characterization and Surface Charge Measurement of Self-Assembled CdS Nanoparticle Films. *Chem. Mater.*, *10* (4), 1160–1165. doi:10.1021/cm970757y.

[115] Stoll, C., Gehring, C., Schubert, K., Zanella, M., Parak, W. J., and Lisdat, F. (2008). Photoelectrochemical signal chain based on quantum dots on gold-Sensitive to superoxide radicals in solution. *Biosens. Bioelectron.*, *24* (2), 260–265. doi:10.1016/j.bios.2008.03.039.

[116] Schubert, K., Khalid, W., Yue, Z., Parak, W. J., and Lisdat, F. (2010). Quantum-dot-modified electrode in combination with NADH-dependent dehydrogenase reactions for substrate analysis. *Langmuir*, *26* (2), 1395–1400. doi:10.1021/la902499e.

[117] Tang, Z., Wang, Y., and Kotov, N. a. (2002). Semiconductor nanoparticles on solid substrates: Film structure, intermolecular interactions, and polyelectrolyte effects. *Langmuir*, *18* (18), 7035–7040. doi:10.1021/la025601d.

[118] Jaffar, S., Nam, K. T., Khademhosseini, A., Xing, J., Langer, R. S., and Belcher, A. M. (2004). Layer-by-layer surface modification and patterned electrostatic deposition of quantum dots. *Nano Lett.*, *4* (8), 1421–1425. doi:10.1021/nl0493287.

[119] Zucolotto, V., Gattás-Asfura, K. M., Tumolo, T., Perinotto, a. C., Antunes, P. a., Constantino, C. J. L., Baptista, M. S., Leblanc, R. M., and Oliveira, O. N. (2005). Nanoscale manipulation of CdSe quantum dots in layer-by-layer films: Influence of the host polyelectrolyte on the luminescent properties. *Appl. Surf. Sci.*, *246* (4), 397–402. doi:10.1016/j.apsusc.2004.11.044.

[120] Kirby, B. J. and Hasselbrink, E. F. (2004). Zeta potential of microfluidic substrates: 1. Theory, experimental techniques, and effects on separations. *Electrophoresis*, *25* (2), 187–202. doi:10.1002/elps.200305754.

[121] Yue, Z., Lisdat, F., Parak, W. J., Hickey, S. G., Tu, L., Sabir, N., Dorfs, D., and Bigall, N. C. (2013). Quantum-Dot-Based Photoelectrochemical Sensors for Chemical and Biological Detection. *ACS Appl. Mater. Interfaces*, *5* (8), 2800–2814. doi:10.1021/am3028662.

[122] Katz, E., Zayats, M., Willner, I., and Lisdat, F. (2006). Controlling the direction of photocurrents by means of CdS nanoparticles and cytochrome c-mediated biocatalytic cascades. *Chemical Communications*, (13), 1395. doi:10.1039/b517332a.

[123] Lioubashevski, O., Chegel, V. I., Patolsky, F., Katz, E., and Willner, I. (2004). Enzyme-catalyzed bio-pumping of electrons into au-nanoparticles: a surface plasmon resonance and electrochemical study. *J. Am. Chem. Soc.*, *126* (22), 7133–43. doi:10.1021/ja049275v.

[124] Lefrançois, A., Couderc, E., Faure-Vincent, J., Sadki, S., Pron, A., and Reiss, P. (2011). Effect of the treatment with (di-)amines and dithiols on the spectroscopic, electrochemical and electrical properties of CdSe nanocrystals' thin films. *Journal of Materials Chemistry*, *21* (31), 11524. doi:10.1039/c1jm10538h.

[125] Haynes, W. M., ed. (2012). CRC Handbook of Chemistry and Physics. CRC Press, 93rd ed. ISBN 1-4398-8049-2.

[126] Hecht, H., Kalisz, H., Hendle, J., Schmid, R., and Schomburg, D. (1993). Crystal Structure of Glucose Oxidase from Aspergillus niger Refined at $2 \cdot 3$ Å Reslution. *J. Mol. Biol.*, *229* (1), 153–172. doi:10.1006/jmbi.1993.1015.

[127] Trinder, P. (1969). Determination of blood glucose using an oxidase-peroxidase system with a non-carcinogenic chromogen. *J. Clin. Pathol.*, *22* (2), 158–61.

[128] Liu, T.-c., Huang, Z.-l., Wang, H.-Q., Wang, J.-h., Li, X.-q., Zhao, Y.-d., and Luo, Q.-m. (2006). Temperature-dependent photoluminescence of water-soluble quantum dots for a bioprobe. *Anal. Chim. Acta*, *559* (1), 120–123. doi:10.1016/j.aca.2005.11.053.

[129] Joshi, A., Narsingi, K. Y., Manasreh, M. O., Davis, E. A., and Weaver, B. D. (2006). Temperature dependence of the band gap of colloidal CdSe/ZnS core/shell nanocrystals embedded into an ultraviolet curable resin. *Appl. Phys. Lett.*, *89* (13), 131907. doi:10.1063/1.2357856.

[130] Erickson, H. P. (2009). Size and shape of protein molecules at the nanometer level determined by sedimentation, gel filtration, and electron microscopy. *Biol. Proced. Online*, *11* (1), 32–51. doi:10.1007/s12575-009-9008-x.

[131] Typical value for the molar exctinction coefficient as reported on the website of Sigma-Aldrich for Lumidot™ 640. URL: `http://www.sigmaaldrich.com/materials-science/nanomaterials/lumidots.html`.

[132] Miller, D. A. B., Chemla, D. S., Damen, T. C., Gossard, A. C., Wiegmann, W., Wood, T. H., and Burrus, C. A. (1984). Band-Edge Electroabsorption in Quantum Well Structures: The Quantum-Confined Stark Effect. *Phys. Rev. Lett.*, *53* (22), 2173–2176. doi:10.1103/PhysRevLett.53.2173.

[133] Marshall, J. D. and Schnitzer, M. J. (2013). Optical strategies for sensing neuronal voltage using quantum dots and other semiconductor nanocrystals. *ACS Nano*, *7* (5), 4601–9. doi:10.1021/nn401410k.

[134] Empedocles, S. a. and Bawendi, M. G. (1997). Quantum-Confined Stark Effect in Single CdSe Nanocrystallite Quantum Dots. *Science*, *278* (5346), 2114–2117. doi:10.1126/science.278.5346.2114.

[135] Geick, R. (1966). Lattice Vibrational Properties of Hexagonal CdSe. *J. Appl. Phys.*, *37* (5), 1994. doi:10.1063/1.1708656.

[136] Park, S.-J., Link, S., Miller, W. L., Gesquiere, A., and Barbara, P. F. (2007). Effect of electric field on the photoluminescence intensity of single CdSe nanocrystals. *Chem. Phys.*, *341* (1-3), 169–174. doi:10.1016/j.chemphys.2007.06.025.

[137] Türck, V., Rodt, S., Heitz, R., Stier, O., Straßburg, M., Pohl, U., and Bimberg, D. (2002). Interplay of surface charges and excitons localized in CdSe/ZnSe quantum dots. *Physica E*, *13* (2-4), 269–272. doi:10.1016/S1386-9477(01)00535-5.

[138] Müller, J., Lupton, J. M., Lagoudakis, P. G., Schindler, F., Koeppe, R., Rogach, a. L., Feldmann, J., Talapin, D. V., and Weller, H. (2005). Wave Function Engineering in Elongated Semiconductor Nanocrystals with Heterogeneous Carrier Confinement. *Nano Lett.*, *5* (10), 2044–2049. doi:10.1021/nl051596x.

[139] Braam, D., Mölleken, A., Prinz, G. M., Notthoff, C., Geller, M., and Lorke, A. (2013). Role of the ligand layer for photoluminescence spectral diffusion of CdSe/ZnS nanoparticles. *Phys. Rev. B*, *88* (12), 125302. doi:10.1103/PhysRevB.88.125302.

[140] Yaacobi-Gross, N., Soreni-Harari, M., Zimin, M., Kababya, S., Schmidt, A., and Tessler, N. (2011). Molecular control of quantum-dot internal electric field and its application to CdSe-based solar cells. *Nat. Mater.*, *10* (12), 974–979. doi:10.1038/nmat3133.

[141] Liu, L., Guo, X., Li, Y., and Zhong, X. (2010). Bifunctional multidentate ligand modified highly stable water-soluble quantum dots. *Inorg. Chem.*, *49* (8), 3768–75. doi:10.1021/ic902469d.

[142] Durisic, N., Wiseman, P. W., Grütter, P., and Heyes, C. D. (2009). A common mechanism underlies the dark fraction formation and fluorescence blinking of quantum dots. *ACS Nano*, *3* (5), 1167–75. doi:10.1021/nn800684z.

[143] Durisic, N., Godin, A. G., Walters, D., Grütter, P., Wiseman, P. W., and Heyes, C. D. (2011). Probing the Dark Fraction of Core-Shell Quantum Dots by Ensemble and Single Particle pH-Dependent Spectroscopy. *ACS Nano*, *5* (11), 9062–9073. doi:10.1021/nn203272p.

[144] Spanhel, L., Haase, M., Weller, H., and Henglein, A. (1987). Photochemistry of colloidal semiconductors. 20. Surface modification and stability of strong luminescing CdS particles. *J. Am. Chem. Soc.*, *109* (13), 5649–5655. doi:10.1021/ja00253a015.

[145] Yu, D., Wang, Z., Liu, Y., Jin, L., Cheng, Y., Zhou, J., and Cao, S. (2007). Quantum dot-based pH probe for quick study of enzyme reaction kinetics. *Enzyme Microb. Technol.*, *41* (1-2), 127–132. doi:10.1016/j.enzmictec.2006.12.012.

[146] Kharlampieva, E., Kozlovskaya, V., Zavgorodnya, O., Lilly, G. D., Kotov, N. a., and Tsukruk, V. V. (2010). pH-responsive photoluminescent LbL hydrogels with confined quantum dots. *Soft Matter*, *6* (4), 800–807. doi:10.1039/B917845G.

[147] Gao, M., Kirstein, S., Möhwald, H., Rogach, A. L., Kornowski, A., Eychmüller, A., and Weller, H. (1998). Strongly Photoluminescent CdTe Nanocrystals by Proper Surface Modification. *J. Phys. Chem. B*, *102* (43), 8360–8363. doi:10.1021/jp9823603.

[148] Smith, A. M., Duan, H., Rhyner, M. N., Ruan, G., and Nie, S. (2006). A systematic examination of surface coatings on the optical and chemical properties of semiconductor quantum dots. *Phys. Chem. Chem. Phys.*, *8* (33), 3895. doi:10.1039/b606572b.

[149] Szajewski, R. P. and Whitesides, G. M. (1980). Rate constants and equilibrium constants for thiol-disulfide interchange reactions involving oxidized glutathione. *J. Am. Chem. Soc.*, *102* (6), 2011–2026. doi:10.1021/ja00526a042.

[150] Edsall, J. T. and Wyman, J. (1958). Biophysical Chemistry. Academic Press.

[151] Biewenga, G., Guido, R., and Bast, A. (1997). An Overview of Lipoate Chemistry. In J. Fuchs, L. Packer, and G. Zimmer, eds., Lipoic Acid in Health and Disease, p. 18. Marcel, Dekker, New York.

[152] Wang, M., Zhang, Q., Hao, W., and Sun, Z.-X. (2011). Surface stoichiometry of zinc sulfide and its effect on the adsorption behaviors of xanthate. *Chem. Cent. J.*, *5* (1), 73. doi:10.1186/1752-153X-5-73.

[153] Jones, M., Lo, S. S., and Scholes, G. D. (2009). Signatures of exciton dynamics and carrier trapping in the time-resolved photoluminescence of colloidal cdse nanocrystals. *J. Phys. Chem. C*, *113* (43), 18632–18642. doi:10.1021/jp9078772.

[154] Yin, Y. and Alivisatos, A. P. (2005). Colloidal nanocrystal synthesis and the organic-inorganic interface. *Nature*, *437* (7059), 664–670. doi:10.1038/nature04165.

[155] Hermanson, G. T. (2013). Bioconjugate Techniques, 3rd Edition, chap. Functional targets for bioconjugation, pp. 127–228. Academic Press.

[156] Banerjee, S., Sen, K., Pal, T. K., and Guha, S. K. (2012). Poly(styrene-co-maleic acid)-based pH-sensitive liposomes mediate cytosolic delivery of drugs for enhanced cancer chemotherapy. *Int. J. Pharm.*, *436* (1-2), 786–797. doi:10.1016/j.ijpharm.2012.07.059.

[157] Garrett, E. R. and Guile, R. L. (1951). Potentiometric Titrations of a Polydicarboxylic Acid: Maleic Acid-Styrene Copolymer. *J. Am. Chem. Soc.*, *73* (10), 4533–4535. doi:10.1021/ja01154a011.

[158] Eshet, H., Grünwald, M., and Rabani, E. (2013). The Electronic Structure of CdSe/CdS Core/Shell Seeded Nanorods: Type-I or Quasi-Type-II? *Nano Lett.*, *13* (12), 5880–5885. doi:10.1021/nl402722n.

[159] Wang, S., Mamedova, N., Kotov, N. a., Chen, W., and Studer, J. (2002). Antigen/Antibody Immunocomplex from CdTe Nanoparticle Bioconjugates. *Nano Lett.*, *2* (8), 817–822. doi:10.1021/nl0255193.

[160] He, Y., Su, Y., Yang, X., Kang, Z., Xu, T., Zhang, R., Fan, C., and Lee, S. T. (2009). Photo and pH stable, highly-luminescent silicon nanospheres and their bioconjugates for immunofluorescent cell imaging. *J. Am. Chem. Soc.*, *131* (12), 4434–4438. doi:10.1021/ja808827g.

[161] Goldman, E. R., Balighian, E. D., Mattoussi, H., Kuno, M. K., Mauro, J. M., Tran, P. T., and Andersont, G. P. (2002). Avidin: A natural bridge for quantum dot-antibody conjugates. *J. Am. Chem. Soc.*, *124* (22), 6378–6382. doi:10.1021/ja0125570.

[162] Pons, T., Uyeda, H. T., Medintz, I. L., and Mattoussi, H. (2006). Hydrodynamic dimensions, electrophoretic mobility, and stability of hydrophilic quantum dots. *J. Phys. Chem. B*, *110* (41), 20308–20316. doi:10.1021/jp065041h.

[163] Wang, Q., Kuo, Y., Wang, Y., Shin, G., Ruengruglikit, C., and Huang, Q. (2006). Luminescent properties of water-soluble denatured bovine serum albumin-coated CdTe quantum dots. *J. Phys. Chem. B*, *110* (34), 16860–6. doi:10.1021/jp062279x.

[164] Hermanson, G. T. (2008). Bioconjugate Techniques (Second Edition), chap. Chapter 3. Zero-Length Crosslinkers, pp. 215–223. Academic Press.

[165] Mori, S. and Barth, H. G. (1999). Size Exclusion Chromatography, chap. Aqueous Size Exclusion Chromatography, p. 172. Springer-Verlag Berlin Heidelberg.

[166] Zerweck, U., Loppacher, C., Otto, T., Grafström, S., and Eng, L. M. (2005). Accuracy and resolution limits of Kelvin probe force microscopy. *Phys. Rev. B*, *71* (12), 125424. doi:10.1103/PhysRevB.71.125424.

[167] Leung, C., Kinns, H., Hoogenboom, B. W., Howorka, S., and Mesquida, P. (2009). Imaging surface charges of individual biomolecules. *Nano Lett.*, *9* (7), 2769–73. doi:10.1021/nl9012979.

[168] Sapsford, K. E., Pons, T., Medintz, I. L., and Mattoussi, H. (2006). Biosensing with Luminescent Semiconductor Quantum Dots. *Sensors*, *6* (8), 925–953. doi:10.3390/s6080925.

[169] Jiang, H. and Ju, H. (2007). Enzyme-quantum dots architecture for highly sensitive electrochemiluminescence biosensing of oxidase substrates. *Chem. Commun.*, (4), 404–406. doi:10.1039/B616007G.

[170] Wu, P., He, Y., Wang, H. F., and Yan, X. P. (2010). Conjugation of glucose oxidase onto Mn-doped Zns quantum dots for phosphorescent sensing of glucose in biological fluids. *Anal. Chem.*, *82* (4), 1427–1433. doi:10.1021/ac902531g.

[171] Zheng, M., Cui, Y., Li, X., Liu, S., and Tang, Z. (2011). Photoelectrochemical sensing of glucose based on quantum dot and enzyme nanocomposites. *J. Electroanal. Chem.*, *656* (1-2), 167–173. doi:10.1016/j.jelechem.2010.11.036.

[172] Khan, S. a., Smith, G. T., Seo, F., and Ellerbee, A. K. (2015). Label-free and non-contact optical biosensing of glucose with quantum dots. *Biosens. Bioelectron.*, *64*, 30–5. doi:10.1016/j.bios.2014.08.035.

[173] Mansur, A., Mansur, H., and González, J. (2011). Enzyme-polymers conjugated to quantum-dots for sensing applications. *Sensors*, *11* (10), 9951–72. doi:10.3390/s111009951.

[174] Yuan, J., Guo, W., and Wang, E. (2008). Quantum dots-bienzyme hybrid system for the sensitive determination of glucose. *Biosens. Bioelectron.*, *23* (10), 1567–71. doi:10.1016/j.bios.2008.01.008.

[175] Bankar, S. B., Bule, M. V., Singhal, R. S., and Ananthanarayan, L. (2009). Glucose oxidase - An overview. *Biotechnol. Adv.*, *27* (4), 489–501. doi:10.1016/j.biotechadv.2009.04.003.

[176] Mancini, M. C., Kairdolf, B. A., Smith, A. M., and Nie, S. (2008). Oxidative Quenching and Degradation of Polymer-Encapsulated Quantum Dots: New Insights into the Long-Term Fate and Toxicity of Nanocrystals in Vivo. *J. Am. Chem. Soc.*, *130* (33), 10836–10837. doi:10.1021/ja8040477.

[177] Pocker, Y. and Green, E. (1973). Hydrolysis of D-glucono-.delta.-lactone. I. General acid-base catalysis, solvent deuterium isotope effects, and transition state characterization. *J. Am. Chem. Soc.*, *95* (1), 113–119. doi:10.1021/ja00782a019.

[178] BRENDA, the enzyme database. URL: `http://www.brenda-enzymes.org/enzyme.php?ecno=1.1.3.4&Suchword=&organism%5B%5D=Aspergillus+niger&show_tm=0`.

[179] Britton, H. T. S. and Robinson, R. A. (1931). CXCVIII. Universal buffer solutions and the dissociation constant of veronal. *J. Chem. Soc.*, p. 1456. doi:10.1039/jr9310001456.

[180] Dougherty, D. P., Da Conceicao Neta, E. R., McFeeters, R. F., Lubkin, S. R., and Breidt, F. (2006). Semi-mechanistic Partial Buffer Approach to Modeling pH, the Buffer Properties, and the Distribution of Ionic Species in Complex Solutions. *J. Agric. Food Chem.*, *54* (16), 6021–6029. doi:10.1021/jf0531508.

List of publications

- Debruyne, D., Deschaume, O., Coutiño González, l., Locquet, J., Hofkens, J., Van Bael, M., Bartic, C. (2015). The pH-dependent photoluminescence of colloidal CdSe/ZnS quantum dots with different organic coatings. *Nanotechnology, 26* (25), 255703-255703. doi:10.1088/0957-4484/26/25/255703.

- Bloemen, M., Debruyne, D., Demeyer, P., Clays, K., Gils, A., Geukens, N., Bartic, C., Verbiest, T. (2014). Catechols as ligands for CdSe–ZnS quantum dots. *RSC Advances, 4*, 10208-10211. doi:10.1039/c3ra47844k.

- De Haeck, J., Bhattacharyya, S., Debruyne, D., Le, H., Nguyen, M., Janssens, E., Nguyen, M., Lievens, P. (2012). Ionization energies and structures of lithium doped silicon clusters. *Physical Chemistry Chemical Physics, 14* (24), 8542-8550. doi:10.1039/c2cp40465f .

- Debruyne, D., Deschaume, O., Trekker, J., Van Bael, M., Bartic, C. (2012). Enzyme Conjugation and Biosensing with Quantum Dots: a Photoluminescence Study. *2012 12TH IEEE CONFERENCE ON NANOTECHNOLOGY (IEEE-NANO)*. IEEE International Conference on Nanotechnology (IEEE-NANO). Birmingham, UK, 20-23 August 2012 (pp. 1-4). doi:10.1109/NANO.2012.6322170.

Conference contributions

- **IEEE Nano 2012.** Birmingham, United Kingdom. 20-23 Aug 2012. Enzyme conjugation and biosensing with quantum dots: A photoluminescence study.
- **International Symposium on Small Particles and Inorganic Clusters XVI.** Leuven, Belgium. 8–13 Jul 2012. The photoluminescent properties of water soluble and enzyme conjugated quantum dots.
- **General Scientific Meeting of the Belgian Physical Society 2013.** Louvain-la-Neuve, Belgium. 22 May 2013. pH-dependent photoluminescence of CdSe/ZnS quantum dots: time-correlated single photon counting and spectral deconvolution.
- **International Conference on Photochemistry 2013.** Leuven, Belgium. 21-26 Jul 2013. pH-induced exciton energy shift in water-solubilized CdSe/ZnS quantum dots.
- **General Scientific Meeting of the Belgian Physical Society 2014.** Leuven, Belgium. May 28th 2014. pH-sensitive quantum dots and rods.

Acknowledgments

The realization of this thesis would not have been possible without the help and support of many people. Therefore, I would like to take a moment to thank these people.

First and foremost, I would like to thank my promotors, Prof. Carmen Bartic and Prof. Margriet Van Bael, for offering me the possibility to pursue this PhD. Their guidance, support, and advice was much appreciated. They remained supportive when things went more difficult, for which I am grateful.

Secondly, I would like to thank the members of my examination committee for their valuable input: Prof. Christ Glorieux, Prof. Jean-Pierre Locquet, Prof. Maria Seo, Prof. Zeger Hens, and Prof. André Vantomme.

Thirdly, I would like to thank the members of my research group: Dr. Olivier Deschaume, Dr. Tobias Peissker, Andreea Ungureanu, Barbara Gysbrechts, and Yovan de Coene. Thank you for the useful discussions, for all the help, and for the good atmosphere in the office. A special thanks goes to Olivier. He was always ready to help out and he taught me uncountable chemistry tricks. I could not have had a better tutor inside or outside the lab!

I am thankful to Prof. Jean-Pierre Locquet and Prof. Chris Van Haesendonck for allowing me the use of their equipment. I thank Bert De Roo for assisting with measurements.

I would like to thank several people from the Chemistry Department. I am obliged to Prof. Johan Hofkens for allowing me the use of his equipment. I would like to thank Eduardo Coutino for his helpfulness, his advice, and for the tool trainings. I am also grateful to Wouter Baekelant.

I would like to thank several people from Imec. I would like to thank Prof. Liesbet Lagae for allowing me to work at Imec. I am grateful to Hilde Jans for accompanying me during my first steps at Imec and for her help with the IWT proposal. I also thank Jesse Trekker for showing me the micelle encapsulation

protocol.

I am thankful to Claire Petermann for helping me with the microfabrication of electrodes in the cleanroom.

I am grateful to the people of the "werkplaats", who were always ready to assist. A special thanks to Philippe Mispelter, Philippe Muylaert, and Valentijn Tuts for helping with the design and the making of components. I would also like to thank Ludwig Henderix for his assistance in the lab and for his advice on chemical products.

I would like to thank Monique Van Meerbeek and Liliane Goffin. Besides taking care of all the orders and administration, they were always there for a supportive conversation.

I should not forget to thank Bas, Bert, Mattias, Matias, Bart, Ewald, Koen, Katrien, and Kelly for the memorable lunch breaks centered around playing cards and ping pong.

Finally, I would like to thank the master students who worked with me on quantum dots: Andrea Bertolucci, Nuria Fabrí Faja, and Christophe Piron.